# Stony Brook University

# Integration of Nanostructured Semiconducting/Conducting Polymers in Organic Photovoltaic Devices

A Dissertation Presented

by

**Htay M. Hlaing**

to

The Graduate School

in Partial Fulfillment of the

Requirements

for the Degree of

**Doctor of Philosophy**

in

**Physics**

Stony Brook University

**May 2012**

**Stony Brook University**

The Graduate School

**Htay M. Hlaing**

We, the dissertation committee for the above candidate for the

Doctor of Philosophy degree, hereby recommend

acceptance of this dissertation.

**Benjamin M. Ocko – Dissertation Advisor**
**Group Leader, Condensed Matter Physics and Materials Sciences,**
**Brookhaven National Lab**

**Peter W. Stephens - Chairperson of Defense**
**Professor, Department of Physics and Astronomy**

**Philip B. Allen**
**Professor, Department of Physics and Astronomy**

**Clark McGrew**
**Associate Professor, Department of Physics and Astronomy**

**Robert B. Grubbs**
**Associate Professor, Department of Chemistry**

This dissertation is accepted by the Graduate School

Charles Taber
Interim Dean of the Graduate School

Abstract of the Dissertation

**Integration of Nanostructured Semiconducting/Conducting Polymers**

**in Organic Photovoltaic Devices**

by

**Htay M. Hlaing**

**Doctor of Philosophy**

in

**Physics**

Stony Brook University

**2012**

One of the main difficulties in incorporating nanotechnology into organic electronic devices is the complexity of fabricating nanoscale structures with relatively well-defined order over relatively large areas. Nanoimprint technology offers a promising route to address this problem, because it can be used to control morphology and molecular orientation of the polymer nanostructures from which functional devices can be built directly.

In this dissertation, the development of novel architectures for organic electronic devices utilizing the polymer nanostructures fabricated by nanoimprint lithography is presented. First, nanoimprinted structures were fabricated with 100 nm spaced grooves from thin films of poly-(3 hexylthiophene), a conjugated semiconducting polymer. These structures have potential applications in the formation of ordered heterojunction organic photovoltaic (OPV) devices. Grazing-incidence wide-angle X-ray scattering studies of the morphology and orientation of the polymer thin films showed that nanoimprinting introduced significant reorientation while Grazing-incidence small-angle X-ray scattering studies demonstrated the excellent fidelity of the

pattern transfer. Temperature-dependent scattering measurements indicated that the imprinted induced orientation and alignment remain intact even at temperatures where the imprinted topographical features nearly vanish.

In the second part of the thesis, the integration of conducting polymer, poly (3,4-ethylenedioxythiophene) poly (styrene sulfonate) (PEDOT:PSS), nanostructures in OPV devices were investigated. PEDOT:PSS nanostructures, fabricated by water-vapor assisted nanoimprinting, have potential to improve the device performance through both an increased interfacial area and the reorientation of the electron-donor polymer in the subsequently deposited active layer.

## Table of Contents

## List of Figures

## List of Tables

**Acknowledgments**

Firstly, I would like to thank my advisor Dr. Ben Ocko for giving me the opportunity to perform research on this exciting field of organic photovoltaic at Brookhaven National Lab. This thesis work would not have been done without his support, guidance, and encouragement in the past few years. I would also like to thanks my on-campus advisor, Professor Peter Stephens, and the rest of my committee members for their work on this thesis committee.

I truly believe that the interdisciplinary research atmosphere and close collaboration of physicists, chemists and engineers within our group are the most important keys for the success of this thesis work and special thanks go to all of my colleagues at soft matter group and electronic materials group at Center for Functional Materials.

Last but not least I would like to thank my whole family for their endless support, although they were quite far away. Finally, the biggest thanks go to my wife, Sanda, for supporting all my adventures and misadventures along the way.

# CHAPTER 1

## Introduction

### 1.1 Motivation

Organic electronics, which utilize the electrical properties of organic materials in the active layers of the devices, have received much attention because they may allow large-area electronic applications to be manufactured in high volumes on arbitrary substrates by printing or other low-cost fabrication techniques. An organic photovoltaic (OPV) is perhaps the most researched device in this paradigm in addition to organic thin films transistors and organic light emitting diodes.

Current organic electronic devices are mainly fabricated by spin-coating or drop-casting followed by thermal or solvent annealing. The morphologies of these devices are uncontrollable and irreproducible and this affects their electrical performances as well as the prospect for mass production. Nanoimprint lithography (NIL) offers a potential solution for producing well-defined morphologies and it also has the potential to be compatible with roll-to-roll processing. Moreover, NIL process influences both the morphology and molecular structure of the imprinted materials and has a profound impact on the performance and quality of the imprinted device. In order to use nano-imprinted polymer nanostructure as a device, it is important to understand the molecular structure and stability of the imprinted pattern outside of the mold, both over a wide temperature range and during subsequence fabrication processes. This thesis investigates the relationship of processing, properties and structure for the development of organic photovoltaic devices based on the NIL technology.

## 1.2 Overview of the thesis

The thesis is structured in the following way:

In Chapter 2, a general introduction to organic solar cells is presented. First, the basic properties of organic photovoltaic materials are described followed by the progress in device architecture, from single layer device to bulk heterojunction device. The operational principle of a photovoltaic device are reviewed together with the critical factors limiting the OPV device performance and strategies for further device improvement. This chapter is concluded by a discussion of the electrical characterization of an OPV device.

In Chapter 3, the scientific background of X-ray scattering and its application for structural analysis of the types of polymer materials used in this work are introduced. A brief overview of synchrotron sources and the beamlines where the experiments were performed is also described.

In Chapter 4, a detailed X-ray structural study of poly(3-alkylthiophene)s (P3ATs) thin films, an important class of semiconducting polymers, is presented. The molecular packing of the P3ATs at room temperature is investigated in detail. Moreover, the structural changes during thermal annealing and during solvent-vapor annealing are also presented.

In Chapter 5, nanoimprinting as a way to control the morphology and molecular orientation of poly(3-hexylthiophene) (P3HT) thin films is investigated. In this chapter, the principles of nanoimprint technology and fabrication of silicon master templates are discussed. Part of this chapter has been published in the following journal article:

*H. Hlaing, X. Lu, T. Hofmann, K.G. Yager, C.T. Black, B.M. Ocko,* "Nanoimprint induced molecular orientation in semiconducting polymer nanostructures", ACS Nano 5, 7532(2011)

In Chapter 6, the fabrication, optimization, and characterization of OPV devices with planar electron blocking layer are discussed.

In Chapter 7, the improvement in OPV performance achieved by incorporating nanoimprinted electron blocking layer is reported. The novel water-vapor-assisted nanoimprinting technique which is applied to fabricate nanostructured PEDOT:PSS layer is also discussed. Part of this chapter have been prepared to submit for publication in peer-reviewed journal.

Chapter 8 summarizes the results presented in this dissertation, and provides an outlook for further investigation and potential device improvement.

# CHAPTER 2

## Organic Solar Cells

### 2.1 Introduction

Organic Photovoltaic (OPV) cells utilize thin films of organic materials which generate electricity when illuminated. In contrast, most solar cells are made from inorganic materials such as crystalline silicon, cadmium telluride and copper indium gallium selenide.[3] Organic solar cells have the potential to substantially reduce the production costs[4, 5] compared to those made of inorganic materials. While there are valid concerns about the availability and toxicity of some of the inorganic materials (e.g. indium, cadmium), the abundant supply of organic materials combined with a large number of easy and cheap processing techniques may eventually make organic solar cells competitive with other energy sources such as gas/oil with little detrimental environmental impact.[6] In the following section, the electronic and physical properties of organic materials used in OPV devices are reviewed and the advantages and disadvantages compared to inorganic materials are discussed. The significant achievements in device performance with respect to the different device architecture are addressed according to the development of the device structure. The basic operating principle of OPV devices is introduced in conjunction with strategies to improve device performance. Finally, the parameters characterizing the device's performance are discussed.

## 2.2 Organic photovoltaic materials

Edmund Bequerel discovered the photovoltaic effect in 1839, but it took a further 50 years until the first successful PV devices were developed.[7] After the discovery and development of p-n junction doping in crystalline silicon and progress in the fabrication of high quality silicon wafers in the 1950s, this technology rapidly developed into a relatively efficient, commercialized energy source, albeit expensive. Conventional inorganic solar panels are based on mono- or poly-crystalline p-n doped silicon with power conversion efficiency (PCE) of up to 25%.[8] Crystalline silicon cells require a high energy input for production with high fabrication costs. Amorphous silicon with its much lower fabrication cost can also be employed but leads to a lower PCE of ~ 14%.[8] Other PV technologies employing element combinations from group III and V such as gallium arsenide (GaAs) and indium phosphide (InP) have reached high efficiency up to 36% but such devices are limited by the low abundance and high toxicity of these elements.

Organic PVs (OPVs) employ organic material which mainly consists of the elements carbon, sulfur, nitrogen, oxygen and hydrogen. In the following, the semiconducting nature of organic materials, which is necessary to understand the basic operation of OPVs is reviewed.

### 2.2.1 Band structure

Photovoltaic materials absorb sunlight to create photogenerated charge carriers. The sun emits light with a range of wavelengths, spanning the ultraviolet, visible and infrared sections of the electromagnetic spectrum. Figure 2.1 shows the amount of radiant energy received from the sun per unit area per unit time as a function of wavelength at a point outside the Earth's atmosphere (AM 0). The solar spectrum for *Air Mass 1.5* (AM 1.5), corresponding to the sun

being at an angle of elevation of 42°, is also plotted in comparison. Since solar energy is greatest at visible wavelengths (300-800 nm), organic materials need to have the ability to absorb light from the visible range of the solar spectrum.

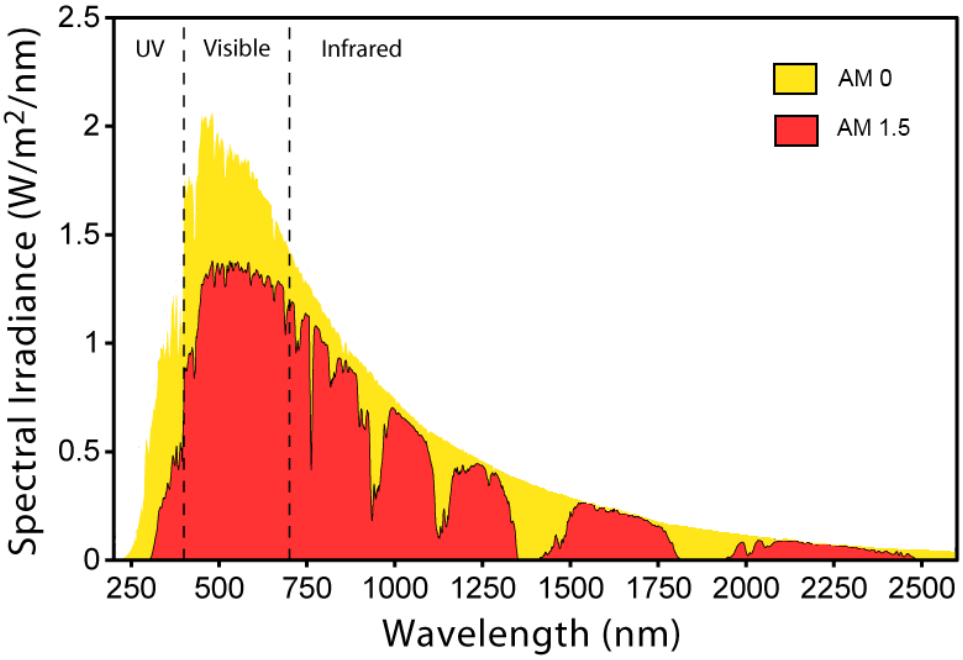


***Figure 2.1*** *Extra-terrestrial (Air Mass 0) solar spectrum (yellow) compared with the standard terrestrial (Air Mass 1.5) spectrum (red).*[7]

For inorganic semiconductors the atoms are tightly bound in all three directions and this gives rise to electronic bands, a range of energy that electrons within the solid are allowed to have, which give these materials their semiconducting properties. The electronic structure consists of a conduction band and a valence band separated by an energy gap the size of which depends upon the material. The incident light photon with sufficient energy will excite an electron from the valence band into the conduction band creating an electron-hole pair. This pair will then be separated into a free electron and a hole by an internal electric field and/or gradient in electron density resulting in photo-generated free charge carriers.[7]

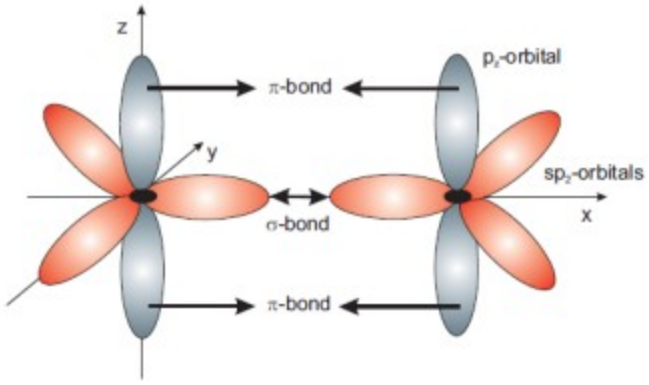


***Figure 2.2*** *$sp_2$-hybridization of the valence electrons of two carbon atoms lead to molecular π and σ bondings.*[2]

The semiconducting nature of organic materials, including π-conjugated polymers, arises from the $sp^2p_z$ hybridized wavefunctions of the carbon atoms.[9] The valence electrons of carbon atoms in ethylene molecules having conjugated π-electron systems are $sp_2$-hybridized as shown in Figure 2.2.[2] The characteristic spatial electron distribution leads to an overlap of the $p_z$ as well as of the $sp_2$ orbitals of adjacent carbon atoms resulting in molecular π and σ bonds, respectively. While the σ-bonds hold the structure of molecule together, the π-bonds are responsible for their semiconducting properties. During the formation of π-bond, the $p_z$ atomic orbitals split into the bonding (π) and anti-bonding (π*) orbitals. The bonding orbital (π) corresponds to the highest occupied molecular orbital (HOMO) while anti-bonding orbital (π*) corresponds to the lowest unoccupied molecular orbital (LUMO). For ethylene, the energy difference between the HOMO and LUMO levels is 6.7 eV and photons with that amount of energy are required to promote an electron from HOMO to LUMO level. However, this is beyond the photon energy of visible solar spectrum which lies between 1.5 eV and 3 eV (see Figure 2.1).

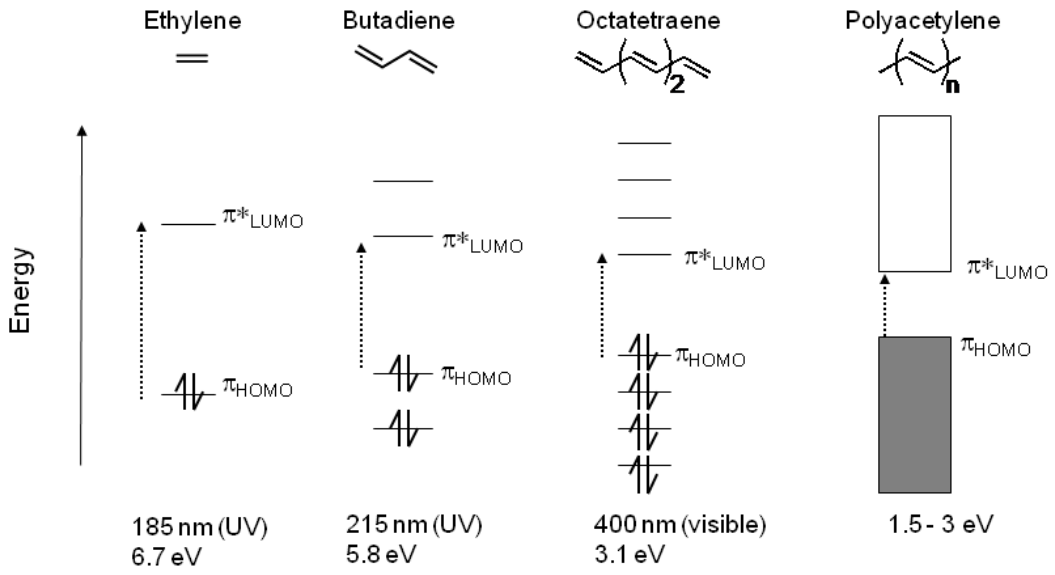


***Figure 2.3.*** *Light absorption of organic materials.*[1]

When two ethylene molecules are brought together to form butadiene, the HOMO level of one ethylene subunit interacts with the HOMO level of the other subunit resulting in a splitting of the two energy levels. The LUMO level of the butadiene splits similarly and the energy difference between HOMO and LUMO level decreases to 5.4 eV as a result. As shown in Figure 2.3, the difference between the HOMO and LUMO levels keeps decreasing as more and more ethylene units are added to the chain. When the conjugation of the polymer reaches a sufficient length they start to exhibit a band structure similar to inorganic crystals with both a conduction and valence band. The band gap (difference in HOMO and LUMO energy levels) of the conjugated polymers also reach within a few eV overlapping well with the solar spectrum. Hence, the photon energy of visible solar spectrum is able to promote an electron from HOMO to LUMO level of the polymer.

### 2.2.2 Advantages of organic materials

Organic materials have several advantages over their inorganic counterparts. One of the main advantages is solution processability of these materials. Due to the added alkyl side chain, most conjugated polymers are soluble in organic solvents and organic thin film devices can be fabricated with low cost manufacturing techniques such as molding, casting, spin coating, roll-to-roll printing etc. These fabrication processes can often be carried out at room temperature allowing the conjugated polymer to be coated on flexible substrates such as polyethylene terephthalate (PET). The flexibility of chemical tailoring to obtain desired properties (e.g. fine tuning of band gap in next generation push-pull polymer) also make conjugated polymers competitive and attractive as active materials for solar cells.

## 2.3 Device architecture

Organic photovoltaic devices were first fabricated based on the idea of inorganic counterpart and later underwent necessary structural changes as our understanding of organic material started to improve. In the following, progress in understanding of OPV devices will be described according to the development of the device structure.

### 2.3.1 Single layer (Single Component) device

The first generation of organic solar cells were fabricated as single layer devices in which thin film of organic semiconductors were sandwiched between two electrodes with different work functions.[10] In this structure, electrons from the low-work-function electrode flow to the

high-work-function electrode until the Fermi levels are equalized throughout the structure providing built-in electric field in the semiconducting layer. As in inorganic semiconductors, this built-in electric field was expected to separate the excitons (electron-hole pairs) which formed in the semiconducting layer after absorbing the incident light. However, a single layer device with 100 nm thick poly (*p*-phenylene vinylene) (PPV) sandwiched between and indium tin oxide (ITO) and aluminum (Al) cathode only provided quantum efficiency of ~ 0.1% under low light condition ($0.1 mW/cm^2$)[10]. Despite various optimizations, the power conversion efficiencies of the single layer devices never exceeds 0.7 % .[11]

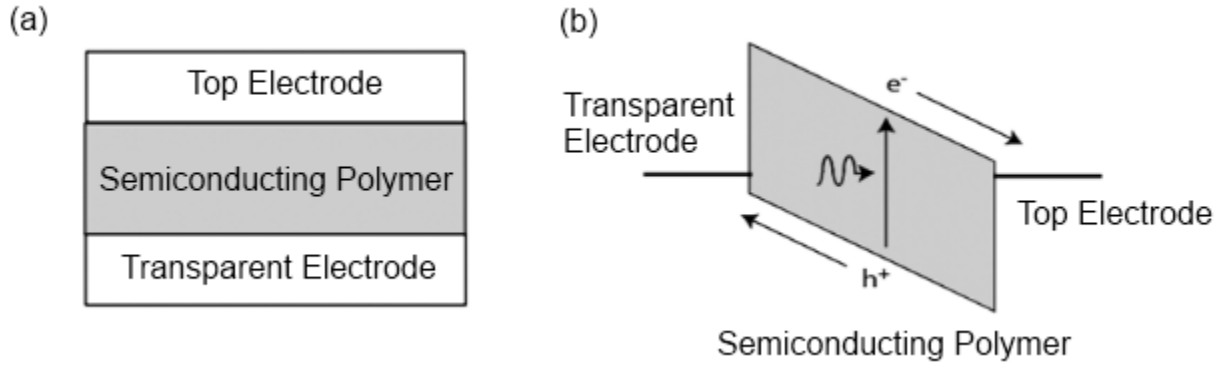


***Figure 2.4.*** *(a) Device structure and (b) schematic energy-band diagram of a single layer device.*

One of the main reasons behind poor device efficiency is the high binding energy of the exciton (0.1-0.4 eV) in semiconducting polymer which is significantly above *kT* (0.026 eV) at room temperature.[9] The built-in electric field provided by the asymmetric work function of the electrodes is insufficient to separate the bound excitons. In a single layer device, the only place to dissociate excitons into free carriers is the interface between semiconducting polymer and a cathode, and most of the excitons generated in the semiconducting polymer are recombined before they can even reach to that interface. Another major problem is intrinsically low mobility

of charge carriers in semiconducting polymer which is often less than $10^{-2}$ $cm^2/V \cdot s$.[6, 9] This is four or five order of magnitude lower than the mobility of single crystalline silicon which is in the range of $10^2$-$10^3$ $cm^2/V \cdot s$.[12] The low mobility of the photogenerated charges in semiconducting polymer prolongs the transit time to the electrodes increasing the recombination rate of the charges in the device.

### 2.3.2 Bilayer device

A bilayer device, first developed by C. W. Tang in 1986, solved the problem of tightly bound excitons by inserting an acceptor semiconductor layer between a donor semiconducting polymer and top electrode (Figure 2.5).[13] In this structure, the energy levels offset between donor and acceptor semiconductor materials provides a sufficient chemical potential energy to overcome the intrinsic exciton-binding energy and excitons that diffuse to the interface can be efficiently separated. Tang's device was fabricated with the layers of ITO/ copper phthalocyanine (CuPc)/ perylene tetracarboxylic derivative (PV)/ silver (Ag)[13] and provided PCE of 1% under AM2 conditions. Another advantage of the bilayer device is that the electrons are transported in the acceptor layer and the holes in the donor layer to their respective electrodes after the excitons are dissociated at the donor/acceptor interface. Therefore, the dissociated holes and electrons are effectively separated from each other and charge recombination is greatly reduced.

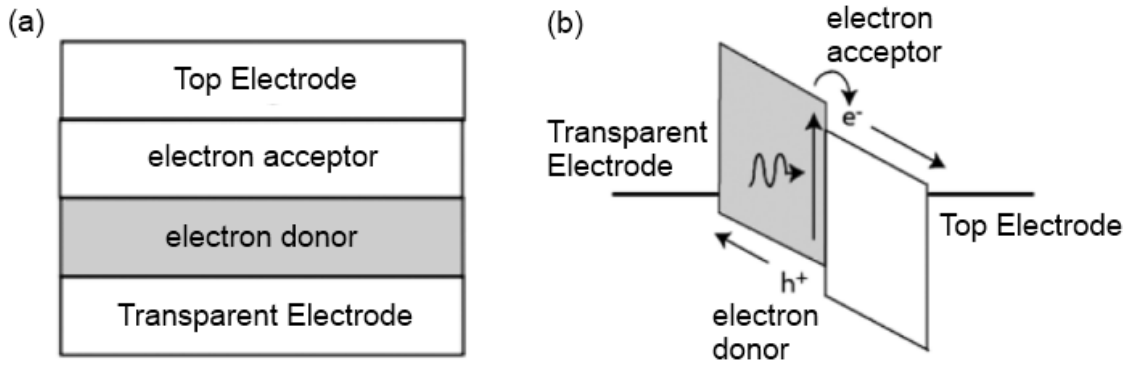


***Figure 2.5.*** *(a) Device structure and (b) schematic energy-band diagram of a bilayer device.*

However, the efficiency of bilayer device is limited by the exciton diffusion length which is the distance that excitons can travel before undergoing non-radiative decay. For soluble semiconducting polymers, the exciton diffusion length is typically in the range of 10-20 nm. Consequently, only the excitons formed within a narrow region adjacent to the donor/acceptor interface can be separated into free charge carriers. On the other hand, even with the high absorption coefficient of semiconducting polymer, film thickness on the order of 100-200 nm are required to absorb most of the incident light. Therefore, a simple bilayer structure cannot reconcile the requirement of two limiting length scales and the majority of the excitons created by incident photons far away from interfacial area are dissipated by recombination. It should be noted, however, that the bilayers devices fabricated from highly crystalline materials with long exciton diffusion length can provide high PCE of up to 3.6 %.[14]

### 2.3.3 Bulk heterojunction device

To address the problem of limited exciton diffusion length in conjugated polymers, Yu et al.[15] and Halls et al.[16] fabricated Bulk heterojunction (BHJ) devices in which two conjugated

polymers were finely intermixed providing large interface area within the reach of exciton. Yu's device consisted of poly[2-methoxy-5(2'-ehtylhexyloxy)-1,4-phenylenevinylene] (MEH-PPV) as a donor and cyano-PPV (CN-PPV) as an acceptor.[15] They observed that the photoluminescence from both polymers was quenched indicating that photogenerated excitons were able to diffuse to the interface and dissociate into free charge carriers before recombining. Following the BHJ device idea, further improvements in PCE were achieved when Gang Li et al. fabricated the OPV device using poly (3-hexylthiophene) (P3HT) and 1-[3-(methoxycarbonyl)propyl]-1-1phenyl)[6,6]$C_{61}$ (PCBM).[17]

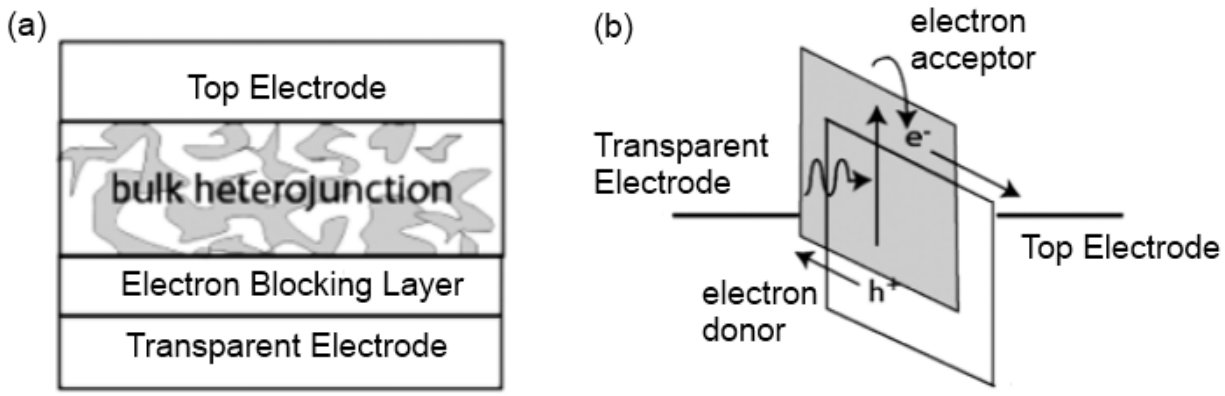


***Figure 2.6.*** *(a) Device structure and (b) schematic energy-band diagram of a bulk heterojunction device. The electron donor is blended with the electron acceptor throughout the active layer and hence the photogenerated excitons can be dissociated into free charges at any place.*

The BHJ device structure, shown schematically in Figure 2.6, depends on forming a bicontinuous and interpenetrating network of the donor and acceptor components in the film such that each absorbing site is within a distance less than the exciton diffusion length of donor-acceptor interface. While bilayer devices have selective and well-defined contacts between the donor phase and anode as well as between the acceptor phases and cathode, the BHJ requires percolated pathways for the hole and electron transporting phases to the right contacts to

minimize the recombination. Therefore, BHJ devices are much more sensitive to the morphology of the blend.[18] The internal film morphology associated with the phase separation between the two materials, domain sizes and crystallinity of the polymers are influenced by the processing parameters including the concentration of materials, film-casting solvent, film thickness, annealing time and temperature, and eventually limited the PCE of the OPV device. BHJ OPV devices have been continuously optimized and improved from 2 percent PCE over the last few years to PCE of 5 percent recently.[6]

## 2.4 Operating principle and strategy to improvement device performance

To understand the limits on the efficiency of BHJ OPV devices and find ways to improve them, it is important to consider all the processes required to convert photon energy into electrical energy. In this section, these processes will be reviewed and the strategy to improve them will be discussed. These processes, shown in Figure 2.7, are: (1) light absorption; (2) exciton diffusion to the D/A interface; (3) exciton dissociation and charge transfer; and (4) charge collection. The external quantum efficiency (*EQE*) characterizes the number of collected charges per incident photon and it can be expressed as the product of the quantum efficiencies of all the processes involved (equation 2.1).

$$EQE = \eta_{abs} \times \eta_{ed} \times \eta_{ct} \times \eta_{cc} \tag{2.1}$$

where $\eta_{abs}$ is the light absorption efficiency, $\eta_{ed}$ is the exciton diffusion efficiency, $\eta_{ct}$ is the charge transfer efficiency and $\eta_{cc}$ is the charge collection efficiency.

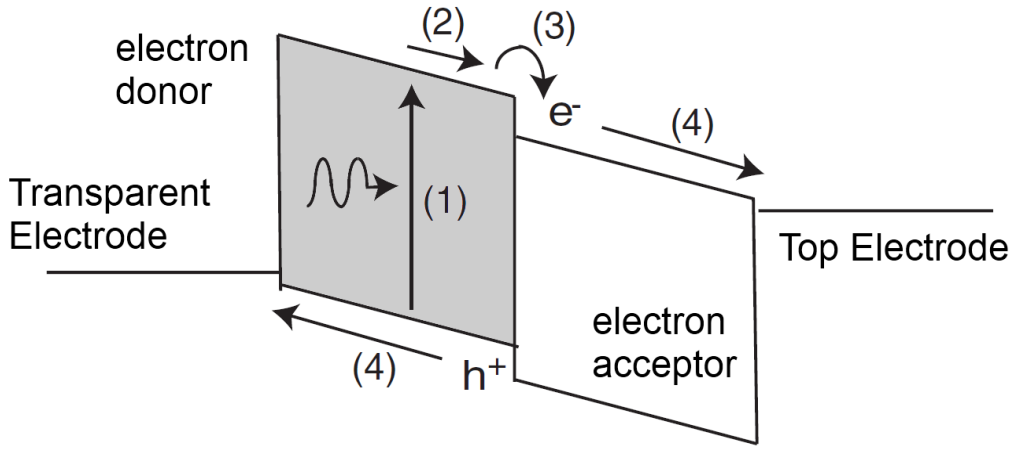


***Figure 2.7.*** *(a) Schematic representation of photocurrent generation in a bulk heterojunction solar cell. The indicated processes are (1) light absorption, (2) exciton diffusion to D/A interface, (3) exciton dissociation and charge transfer, and (4) charge collection.*

### 2.4.1 Light absorption

In order to have efficient light absorption, organic semiconductors need to satisfy two requirements. First, the band gap must be small enough to enable the organic semiconductors to absorb most of the light in the solar spectrum. While a band gap of ~1.1 eV could absorb ~77% of the solar irradiation, most of the organic semiconductors currently employed for OPV have band gaps higher than 2 eV, harvesting only ~30% of the solar irradiation.[19] Second, the film must be thick enough to absorb most of the incident light. As shown in Figure 2.8, the typical absorption coefficient (α) of organic semiconductors is ~ $10^5$/cm, with a spectrum width of ~ 200 nm.[20] To absorb incident light efficiently, organic active layer needs to be thicker than the optical absorption length, $L_A$, which is calculated from absorption coefficient, $L_A = 1/\alpha$. Therefore, an ideal thickness for most organic semiconductors is > 100 nm.

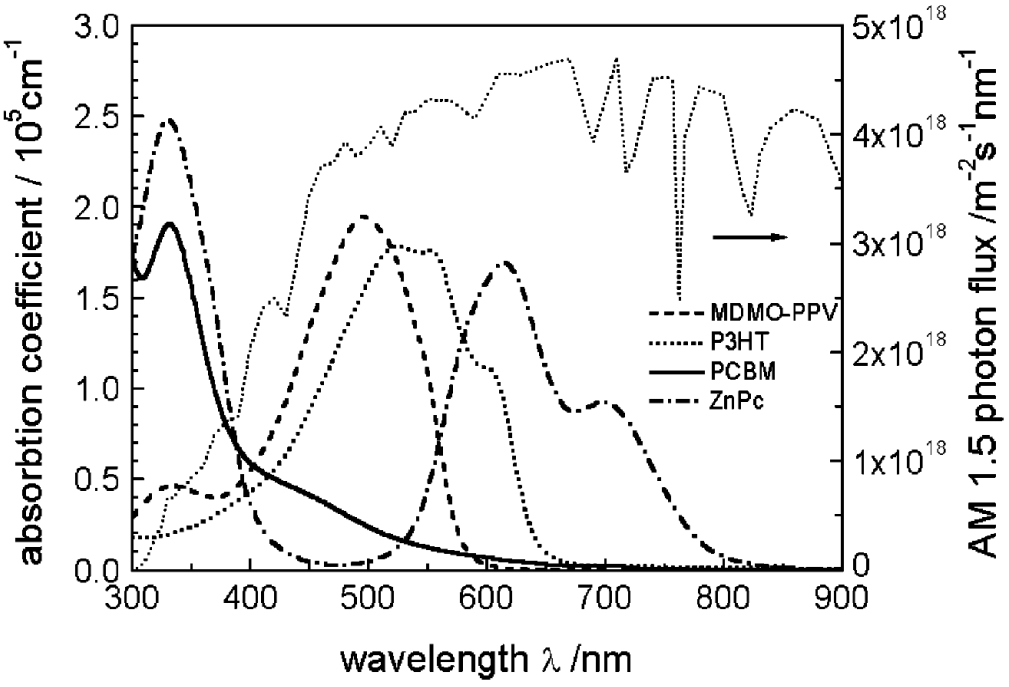


***Figure 2.8.*** *Absorption coefficients of films of commonly used OPV materials are depicted in comparison with the standard AM 1.5 terrestrial solar spectrum. This figure is obtained from reference 19.*

One way to improve light absorption is to synthesize smaller band-gap materials such that the absorption spectrum of the active material matches the solar irradiation for maximum absorption. Significant advances have been made in tuning of the band gap and energy levels of organic semiconductors by chemical synthesis[21] but this will not be discussed further in this thesis.

### 2.4.2 Exciton diffusion

An exciton, formed in the organic semiconductor after absorbing a photon, must diffuse to the interface with the acceptor material and be dissociated into free electrons and holes before it recombines. Generally, the diffusion process is measured by the exciton diffusion length ($L_D$)

which is an average distance exciton can diffuse before its recombination. $L_D$ can vary depending on the structure of the material and the dielectric properties. For instance, $L_D$ for CuPc has been reported between 10 nm and 68 nm[14, 22], for $C_{60}$ around 40 nm,[14] and for SubPc between 8 and 28 nm.[23, 24] For polymeric semiconductors, $L_D$ is in the order of 10 nm.[25] Hence, $L_D$ limits the size of the phase separated donor and acceptor domains in BHJ OPV device.

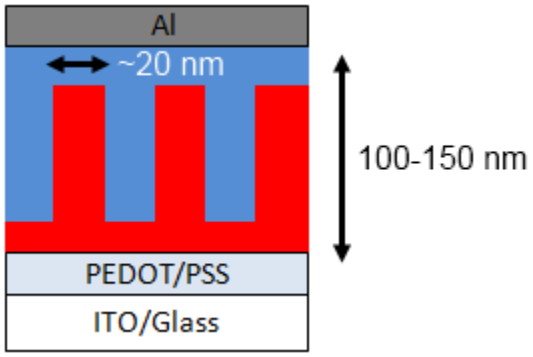


***Figure 2.9.*** *Ordered Heterojunction OPV device with the phase separation distance of ~ 20 nm and thickness of 100-150 nm.*

Due to the random phase separation of donor and acceptor materials, exciton diffusion to an D/A interface in BHJ OPV device can be greatly hindered by early recombination at grain boundaries, defects and trap sites.[4, 6] Therefore, a thin film is preferred for efficient exciton diffusion conflicting with the requirement of a thick film for high photon absorption. One promising approach to achieve full exciton harvesting is to fabricate ordered heterojunction (OHJ) devices with controlled dimensions by templating or nanostructuring of the donor and acceptor phases as shown in Figure 2.9. In OHJ devices, the $L_D$ is decoupled from the absorption length and thick films could be fabricated without affecting the efficiency of exciton diffusion. The effort to fabricate OHJ device utilizing nanoimprint lithography will be presented in Chapter 5.

### 2.4.3 Exciton dissociation

After an exciton in the donor material diffuses to the D/A interface, the exciton will transfer an electron to adjacent acceptor molecule leaving the hole behind in a process known as exciton dissociation. For exciton dissociation to happen efficiently, the offset in LUMO levels of the donor and acceptor must be sufficient to overcome the exciton-binding energy. However, this offset in energy levels must not be too large since the maximum voltage attainable from BHJ OPV is determined by the gap between the HOMO of the electron donor and the LUMO of the acceptor.[26] The optimization of the various energy levels of donor and acceptor materials to balance these two requirements has been a central focus of polymer synthesis groups.[21, 26]

### 2.4.4 Charge collection

After excitons are completely dissociated at the D/A interface, the holes in the donor polymer and the electrons in the acceptor molecule must reach corresponding electrodes. Since the charge transport through organic materials is typically several orders of magnitude slower than inorganic thin film,[27] they are prone to interfacial recombination along collection pathway packed with a high density of recombination sites such as grain boundaries and impurities. The isolated donor or acceptor domains formed due to the uncontrolled phase-separation of BHJ OPV morphology provide another limitation for efficient charge collection. The problem could be mitigated by making thin active layers so that the carriers do not have to travel very far. Unfortunately, this conflicts again with the requirement that the active layer must be thick enough to absorb most of the incident photons.

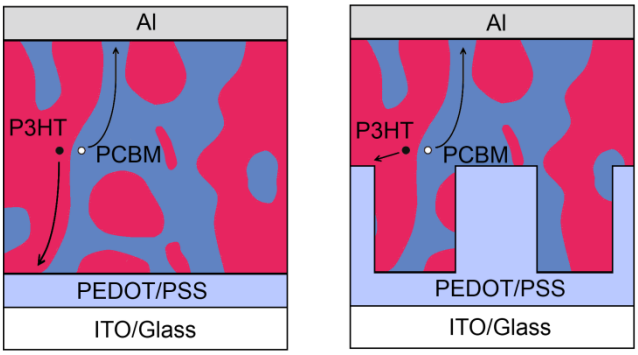


***Figure 2.10.*** *Schematic comparing charge collection in a BHJ solar cells with planar (left) and nanostructured (right) PEDOT:PSS layers.*

The incorporation of nanostructured electrodes in OPV device (see Figure 2.10) should improve the charge collection efficiency since it can satisfy the requirement of separating the light absorption from the charge carrier transport. The effective thickness of the active blend layer can be increased while the distance of the nanostrucured electrodes can be optimized for an efficient charge extraction. The fabrication of nanoimprinted electron blocking layers as part of the nanostructured electrodes in BHJ OPV devices will be studied in more detail in chapter 6.

## 2.5 Characterization of an OPV device

### 2.5.1 Power conversion efficiency (PCE)

PCE is one of the most important parameter to characterize OPV performances. It is defined as the ratio of maximum output of electrical power to the incident light power. The current-voltage characteristics of an OPV device under illumination are shown in Figure 2.11. The curve is characterized by several parameters: (1) the short-circuit current density $J_{sc}$ - the current density at zero applied voltage, (2) the open-circuit voltage $V_{oc}$ - the applied voltage at which the current in the external circuit equals zero, (3) the maximum power point - the point on

the curve with maximum electrical power density $P_{max} = (JV)_{max}$, and (4) the fill factor *FF* - the ratio of $P_{max}$ to $J_{sc} \cdot V_{oc}$ . External work can only be done when the cell operates in the fourth quadrant, i.e., when $0 < V < V_{oc}$. The PCE can now be expressed in terms of $J_{sc}$, $V_{oc}$ and *FF*:

$$PCE = P_{max}/P_{in} = (JV)_{max}/P_{in} = J_{sc} \times V_{oc} \times FF/P_{in} \tag{2.1}$$

$$FF = J_{max} \times V_{max}/J_{sc} \times V_{oc} \tag{2.2}$$

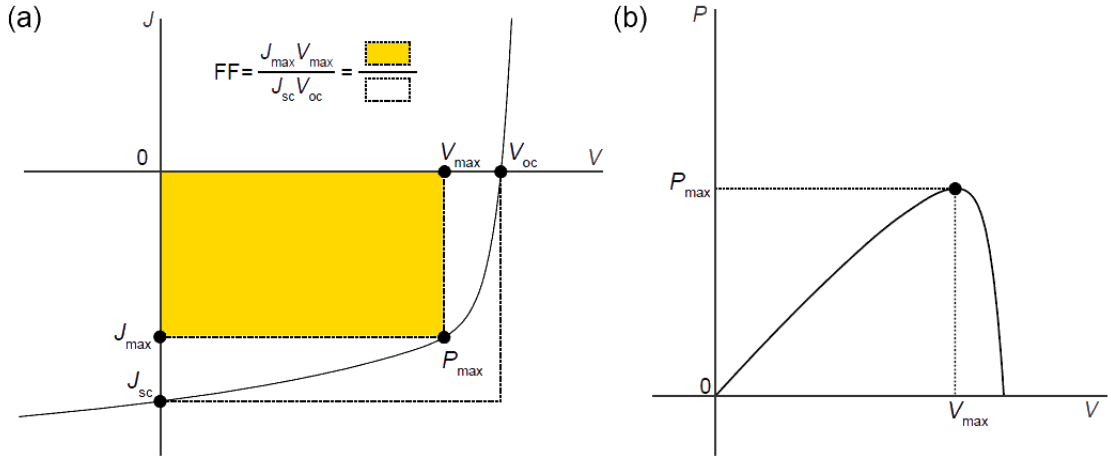


***Figure 2.11.*** *(a) Typical J-V curve of an OPV under illumination. The parameters determining the device efficiency are indicated in the figure and explained in the text. (b) Corresponding power versus voltage plot, from which $P_{max}$ and thus $J_{max}$ and $V_{max}$ are determined.*

### 2.5.2 External quantum efficiency (EQE)

EQE is another important parameter for solar cell characterization. It is calculated by the number of electrons extracted in an external circuit divided by the number of incident photons at a certain wavelength under short-circuit condition as follow:

$$EQE(\lambda) = \frac{number\ of\ electrons}{number\ of\ photons} = \frac{J_{sc}(\lambda)/e}{P_{in}(\lambda)/\left(\frac{hc}{\lambda}\right)} = \frac{J_{sc}(\lambda)hc}{P_{in}(\lambda)e\lambda} \tag{2.3}$$

where λ is the wavelength, *e* is the elementary charge, *h* is the Plank constant, and *c* is the speed of light in vacuum. Note that EQE represents the external quantum efficiency, meaning that the losses due to reflection at the surface and the transmission through the device are also included in EQE. Considering the fraction of the actually absorbed photons by the photoactive layer, EQE can be converted into internal quantum efficiency (IQE):

$$IQE(\lambda) = \frac{EQE(\lambda)}{1-Ref(\lambda)-Tran(\lambda)} \tag{2.4}$$

where Ref(λ) is the fraction of reflected light and Trans(λ) is the fraction of the transmitted light.

### 2.5.3 Spectral mismatch correction

A sun simulator which can simulate natural sunlight is usually used as a light source for repeatable and accurate indoor testing solar cells. In order to compare results from various devices, solar cells are characterized based on internationally accepted standard reporting conditions (SRC), which are referred to a cell temperature of 25 °C under air mass 1.5 global (AM1.5 G) illumination spectrum at an intensity of 1000 W/m$^2$. This AM 1.5 G condition corresponds to the spectrum and irradiance of sunlight incident upon an inclined plane at 37° tilt toward the equator with an elevation of 41.81° above the horizon.

A Si reference solar cell is mostly used as the reference cell for calibrating a sun simulator. Usually there is a spectral mismatch in the measured short-circuit current of the solar cell with respect to a AM1.5 G reference spectrum. The reasons for this spectral mismatch are: 1) the spectrum mismatch between the light source and the AM 1.5G reference spectrum, and 2) the difference of spectral response between Si reference cell and testing cell. The mismatch value can be calculated by using the spectral responsivity data for the testing cell and reference cell

combinations. Once a mismatch factor is known, the Jsc and the PCE of the testing cell can be calibrated.[28]

## 2.6 References


1. Light Absorption of Conjugated Materials. http://photonicswiki.org/images/d/d3/Polyene_series.PNG
2. http://wps.prenhall.com/wps/media/objects/3311/3391094/blb0906.html.
3. Goetzberger, A.; Hebling, C.; Schock, H. W., Photovoltaic materials, history, status and outlook. *Mat Sci Eng R* **2003,** 40, (1), 1-46.
4. Sariciftci, N. S.; Brabec, C. J.; Hummelen, J. C., Plastic solar cells. *Adv Funct Mater* **2001,** 11, (1), 15-26.
5. Service, R. F., Outlook Brightens for Plastic Solar Cells. *Science* **2011,** 332, (6027), 293-293.
6. Brabec, C. J.; Dyakonov, V.; Scherf, U., *Organic photovoltaics : materials, device physics, and manufacturing technologies*. Wiley-VCH: Weinheim, 2008; p xxi, 575 p.
7. Nelson, J., *The physics of solar cells*. Imperial College Press ;

   Distributed by World Scientific Pub. Co.: London

   River Edge, NJ, 2003; p xix, 363 p.
8. Green, M. A.; Emery, K.; Hishikawa, Y.; Warta, W., Solar cell efficiency tables (version 36). *Prog Photovoltaics* **2010,** 18, (5), 346-352.
9. Heeger, A. J., Semiconducting polymers: the Third Generation. *Chem Soc Rev* **2010,** 39, (7), 2354- 2371.
10. Marks, R. N.; Halls, J. J. M.; Bradley, D. D. C.; Friend, R. H.; Holmes, A. B., The Photovoltaic Response in Poly(P-Phenylene Vinylene) Thin-Film Devices. *J Phys-Condens Mat* **1994,** 6, (7), 1379-1394.

11. Sariciftci, N. S., Plastic solar cells. *Abstr Pap Am Chem S* **2001,** 222, U281-U281.

12. Electrical properties of silicon. In.

13. Tang, C. W., 2-Layer Organic Photovoltaic Cell. *Appl Phys Lett* **1986,** 48, (2), 183-185.

14. Forrest, S. R.; Peumans, P.; Yakimov, A., Small molecular weight organic thin-film photodetectors and solar cells. *J Appl Phys* **2003,** 93, (7), 3693-3723.

15. Yu, G.; Heeger, A. J., Charge Separation and Photovoltaic Conversion in Polymer Composites with Internal Donor-Acceptor Heterojunctions. *J Appl Phys* **1995,** 78, (7), 4510-4515.

16. Halls, J. J. M.; Walsh, C. A.; Greenham, N. C.; Marseglia, E. A.; Friend, R. H.; Moratti, S. C.; Holmes, A. B., Efficient Photodiodes from Interpenetrating Polymer Networks. *Nature* **1995,** 376, (6540), 498-500.

17. Li, G.; Shrotriya, V.; Huang, J. S.; Yao, Y.; Moriarty, T.; Emery, K.; Yang, Y., High-efficiency solution processable polymer photovoltaic cells by self-organization of polymer blends. *Nat Mater* **2005,** 4, (11), 864-868.

18. Brady, M. A.; Su, G. M.; Chabinyc, M. L., Recent progress in the morphology of bulk heterojunction photovoltaics. *Soft Matter* **2011,** 7, (23), 11065-11077.

19. Nunzi, J. M., Organic photovoltaic materials and devices. *Cr Phys* **2002,** 3, (4), 523-542.

20. Hoppe, H.; Sariciftci, N. S., Organic solar cells: An overview. *J Mater Res* **2004,** 19, (7), 1924- 1945.

21. Zhou, H. X.; Yang, L. Q.; You, W., Rational Design of High Performance Conjugated Polymers for Organic Solar Cells. *Macromolecules* **2012,** 45, (2), 607-632.

22. Stubinger, T.; Brutting, W., Exciton diffusion and optical interference in organic donor-acceptor photovoltaic cells. *J Appl Phys* **2001,** 90, (7), 3632-3641.

23. Gommans, H.; Schols, S.; Kadashchuk, A.; Heremans, P.; Meskers, S. C. J., Exciton Diffusion Length and Lifetime in Subphthalocyanine Films. *J Phys Chem C* **2009,** 113, (7), 2974-2979.

24. Luhman, W. A.; Holmes, R. J., Investigation of Energy Transfer in Organic Photovoltaic Cells and Impact on Exciton Diffusion Length Measurements. *Adv Funct Mater* **2011,** 21, (4), 764-771.

25. Blom, P. W. M.; Mihailetchi, V. D.; Koster, L. J. A.; Markov, D. E., Device physics of polymer : fullerene bulk heterojunction solar cells. *Advanced Materials* **2007,** 19, (12), 1551-1566.

26. Scharber, M. C.; Wuhlbacher, D.; Koppe, M.; Denk, P.; Waldauf, C.; Heeger, A. J.; Brabec, C. L., Design rules for donors in bulk-heterojunction solar cells - Towards 10 % energy-conversion efficiency. *Advanced Materials* **2006,** 18, (6), 789-+.

27. Dimitrakopoulos, C. D.; Mascaro, D. J., Organic thin-film transistors: A review of recent advances. *Ibm J Res Dev* **2001,** 45, (1), 11-27.

28. Li, G.; Shrotriya, V.; Yao, Y.; Huang, J. S.; Yang, Y., Manipulating regioregular poly(3-hexylthiophene): [6,6]-phenyl-C-61-butyric acid methyl ester blends - route towards high efficiency polymer solar cells. *J Mater Chem* **2007,** 17, (30), 3126-3140.

# CHAPTER 3

## Synchrotron X-ray Scattering Techniques

### 3.1 Introduction

X-rays are electromagnetic radiation with a wavelength in the range of 0.01 to 10 nm, corresponding to energies in the range of 120 eV to 120 keV. Since the first X-ray diffraction experiment in 1912,[1] X-rays have become an invaluable tool to probe the structure of matter. X-rays can be generated from a variety of sources. In a standard x-ray tube, x-rays are generated when a metal anode under vacuum is bombarded by electrons accelerated by a high-voltage electric field. As electrons collide with atoms in the target, they slow down and emit a continuous spectrum of X-rays, which is known as Bremsstrahlung radiation. The high energy electrons also eject the inner shell electrons in atoms through the ionization process. When a free electron fills the shell, X-ray photon with energy characteristic of the target material is emitted. Common targets such as Cu and Mo used in X-ray tubes produce X-ray with corresponding wavelengths of 0.154 nm and 0.07 nm, respectively. However, this way of producing X-ray heats up the metal target and the cooling efficiency of the metal anode eventually restricts the intensity of the x-ray beams.[4] Synchrotron radiation sources of X-rays were introduced in the 1970s.[5] Synchrotron radiation is the electromagnetic radiation emitted when charged particles such as electrons or positrons, traveling at relativistic velocities, are accelerated by a magnetic field.[6] Producing x-rays in this way removes the thermal issue associated with x-ray tube source. Synchrotron sources are much brighter than conventional X-ray sources and allow X-ray studies that are not possible with laboratory based X-ray sources.

X-ray scattering from polymer thin film samples, like those investigated in this thesis work, is relatively weak due to the weak scattering strength of carbon, the small number of scattering planes, and disorder in these films.[7] Therefore, high flux X-ray sources are necessary to achieve considerable scattering intensities. For conventional X-ray sources, long data collection times are required and usually only the strongest peaks are observed. Synchrotron sources also have the advantage of the low angular dispersion allowing for very high resolution measurement of peak widths and positions.

In this chapter, the synchrotron X-ray scattering techniques employed in this work are introduced. First, synchrotron X-ray sources and the experimental setups of synchrotron x-ray scatterings are reviewed. Then X-ray diffraction in grazing incidence geometry is described in detail. Many of the well understood principles of x-ray scattering have been compiled in excellent textbooks[6, 7] and review articles[3, 8], and these are the primary sources of references for this chapter and other references are also cited wherever possible.

## 3.2 Synchrotron radiation X-ray sources

The National Synchrotron Light Source (NSLS) at Brookhaven National Laboratory is a second generation synchrotron X-ray source. The NSLS is a user facility that supports 58 X-ray experimental beamlines (51 are operational).[9] The electrons that generate the synchrotron radiation are first produced by a 100 KeV triode electron gun. These electrons are accelerated through a linear accelerator, which provides them up to 120 MeV. Next, the electrons are guided by a bending magnet toward a circular accelerator (booster ring) where they are strongly accelerated to reach the energy of 750 MeV. Finally, these electrons are injected into the X-ray

ring which further ramped up to 2.8 GeV.[10] X-rays are emitted when the orbiting electrons are accelerated radially by the bending magnets (BM) or insertion devices (ID) such as undulators and wigglers. These X-rays are then guided into the end station (beamlines) to perform experiments. X-ray scattering experiments for this thesis work were performed at the X22B (BM), X21 (ID) and X9 (ID) beamlines.

## 3.3 X-ray scattering methods

There are many X-ray techniques available to study the structures and properties of the materials including diffraction measurements and absorption spectroscopy. In this thesis work, X-ray scattering in grazing-incidence geometry is primarily used to study thin film samples for the following reasons:

1) the substrates are generally too thick for transmission geometry;

1) average statistical information is obtained over the illuminated sample area;

2) the technique can be applied in various environments ranging from ultra-high vacuum to vapor atmospheres;

3) the kinetic studies can be carried out as function of temperature, pressure, etc.;

4) the structures at different depth of the samples can be characterized using different incident angles.

### 3.3.1 Grazing-incidence geometry

The characteristic penetration length of X-ray into bulk material can vary from a few μm to a few mm depending upon the X-ray energy and the properties of materials.[11] This is significantly deeper than most polymer thin film samples that range from a few nm to several hundred nanometers thick. Therefore, it is beneficial to probe the samples with the X-ray beam coming in at a very small grazing incident angle with respect to the sample surface in order to maximize the scattering volume. In this geometry, two common measurements are X-ray reflectivity (XRR) and grazing incident X-ray Scattering (GIXS). In XRR, the intensity of the X-ray reflected along the specular direction from the surfaces is measured. In GIXS, diffraction from the periodic variation in electron densities is observed. In the following, the basics of X-ray scattering under grazing incidence is reviewed, and how these phenomena are exploited to provide structural information from varying length scales and orientations is described.

The index of refraction of organic thin films at X-ray wavelengths is slightly less than unity and can be described as[6]

$$n = 1 - \delta + i\beta \tag{3.1}$$

where the real and imaginary parts of the index of refraction, δ and β, account for the dispersion and absorption of the material, respectively. They are defined as

$$\delta = \rho\lambda^2 r_0/2\pi \tag{3.2}$$

$$\beta = \lambda\mu/4\pi \tag{3.3}$$

where ρ is the number density of electrons, λ is the X-ray wavelength, $r_0$ is the classical electron radius, and μ is the attenuation coefficient. For X-rays, Snell's law predicts that when going from

a material of low electron density (often air with n = 1) to one of higher electron density such as a thin film supported by a substrate, total external reflection occurs below the critical angle, $\alpha_c$ where $\alpha_c$ is given by $\approx \sqrt{2\delta}$. Below the critical angle (typically ~ 0.1° for a polymer thin film with 13.5 keV X-rays), the X-rays travel as an evanescent plane wave along the sample surface. The penetration depth of the X-rays is determined by the incidence angle, allowing precise control of the X-ray intensity through the film depth. Figure 3.1 gives a typical penetration profile for an organic thin film (P3HT) as a function of incident angle.

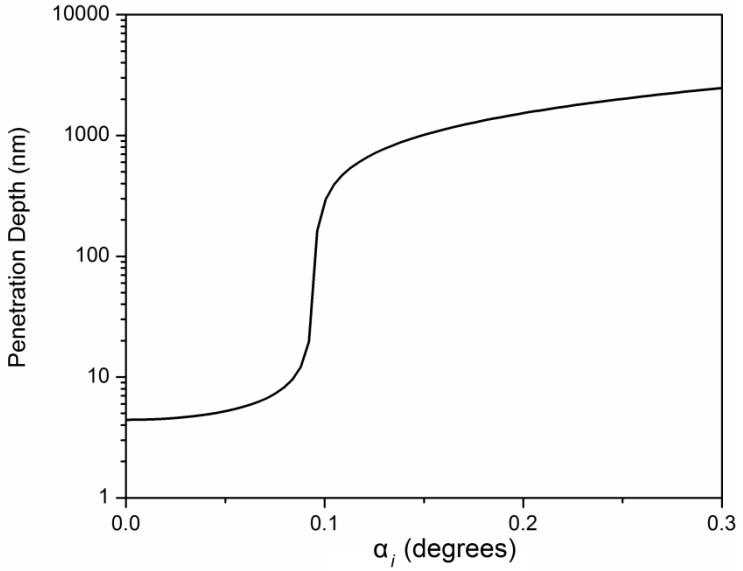


***Figure 3.1.*** *Penetration depth of the incident X-ray beam as a function of incidence angle ($\alpha_i$ ) for a P3HT thin film. The calculation was based on the following parameters ($\lambda = 0.0918\,nm,\ \delta = 3.07 \times 10^{-6}, \beta = 2.20 \times 10^{-8}$) which were obtained from reference 3.*

This property of angle dependent penetration depth can be utilized in the experiments to selectively collect the scattering from the surface region of a film. It can also be used to suppress the scattering from the substrate (usually higher electron density) by operating at an incidence angle such that $\alpha_c(\text{polymer}) < \alpha_i < \alpha_c(\text{substrate})$. However, as shown in Figure 3.1, small changes in the incidence angle can result in a large change in the penetration depth near the

critical angle affecting both the sampling volume and the scattering intensity. Therefore, it is essential to have accurate control of the incident angle, a small beam divergence, and a flat sample for the GIXS experiments.

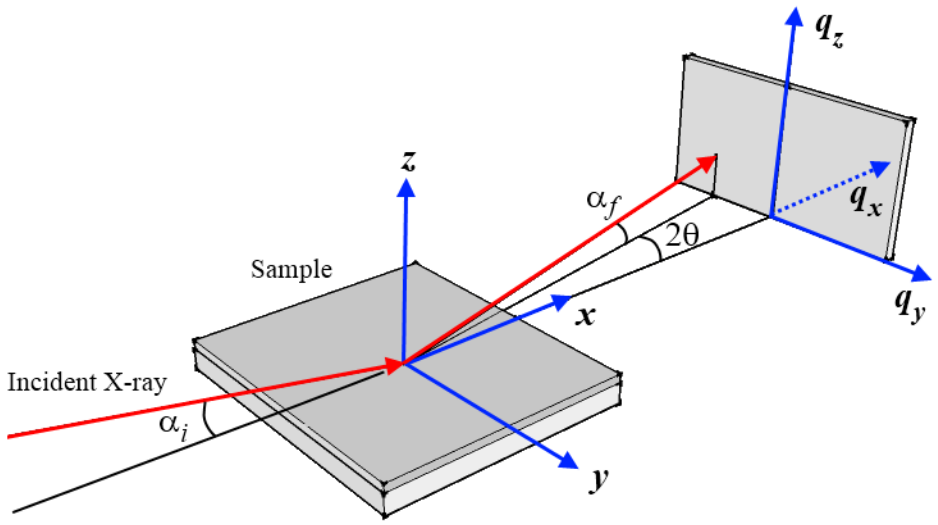


***Figure 3.2.*** *Geometry of GIXS: $\alpha_i$ is the incident angle of the X-ray beam while $\alpha_f$ and $2\theta$ are the exit angles of the X-ray beam with respect to the film surface and to the plane of incidence respectively, and $q_x$, $q_y$, $q_z$ are the components of the scattering vector* ***q****.*

The scattering geometry of the GIXS experiment is shown in Figure 3.2. The sample surface defines the (*x,y*) plane with the *z*-axis along the surface normal. The incident X-ray with wave vector $\mathbf{k_i}$ ($k_0 = 2\pi/\lambda$) impinges onto the sample surface under an incident angle $\alpha_i$ and scattered under an exit angle $\alpha_f$ and an out-of-plane angle $2\theta$. Assuming the energy of X-ray is conserved (i.e. elastic scattering), the X-ray beam is scattered with wave vector $\mathbf{k_f}$ and the scattering wave vector $\mathbf{q}$ is defined as

$$\boldsymbol{q} = (\mathbf{k_f} - \mathbf{k_i}) = (q_x, q_y, q_z) \tag{3.4}$$

with components

$$q_x = \frac{2\pi}{\lambda}\left[\cos(2\theta)\cos(\alpha_f) - \cos(\alpha_i)\right], \quad (3.5)$$

$$q_y = \frac{2\pi}{\lambda}\left[\sin(2\theta)\cos(\alpha_f)\right], \quad (3.6)$$

$$q_z = \frac{2\pi}{\lambda}\left[\sin(\alpha_i) + \sin(\alpha_f)\right]. \quad (3.7)$$

For specular scattering, the wave vector components are $q_x = q_y = 0$ and $q_z \neq 0$, providing information along out-of-plane direction. With off-specular scattering, the lateral component is $q_r = (q_x, q_y) \neq 0$ providing the in-plane structure of the sample.

Depending on the scattering angle, two regimes of GIXS experiments are available: grazing-incidence wide-angle X-ray scattering (GIWAXS) and grazing-incidence small-angle X-ray scattering (GISAXS). GIWAXS probes the length scales on the order of molecular dimensions (0.1-10 nm) and therefore provides information about short range order. GISAXS probes relatively long correlation distances compared to molecular dimensions (typically >10 nm) and can be utilized in characterizing the periodic nanostructures that have correlated changes in electron density such as polymer nanogratings and nanodots.

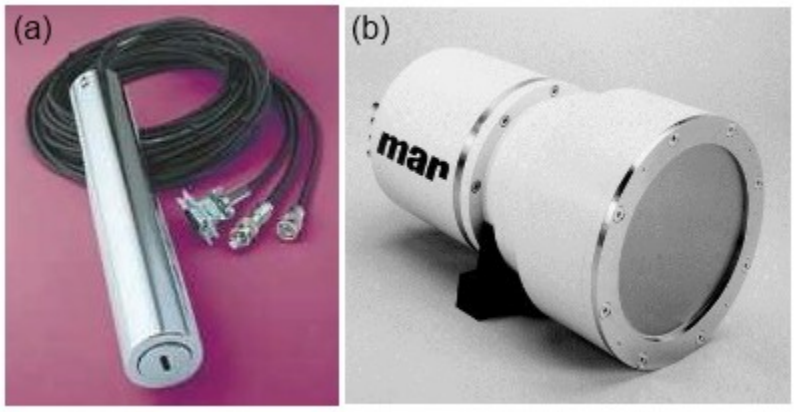


***Figure 3.3.*** *(a) Bicron point-detector[2] and (b) Mar CCD detector*

There are two primary methods for measuring the angle and intensity of the scattered X-rays: a point-detector and an area detector (see Figure 3.3). The two methods have their own advantages and disadvantages. A point-detector is based on amplification of visible fluorescence from a scintillator such as NaI with a photomultiplier. In the point-detector configuration, scattered X-ray is collected by the detector with collimating slits. While the point detector provides high accuracy and high resolution, the measurements are slow since each scattering angle and direction need to be scanned separately. Therefore, it is not suitable for the in-situ experiments with time limitations. It also prolongs the X-ray exposure to the sample and could result in beam damage for some samples such as organic thin films. The area-detector configuration, one the other hand, allows rapid collection from the large range of scattering angles with limited resolution and accuracy. The area detector is usually a charge-couple detector (CCD) array or an image plate. Since a large number of scattering angles are collected simultaneously, the area-detector configuration can provide fast data collection with limited exposure time (< 60 s for typical experiments performed in this thesis). The quick measurements diminish the effects of beam damage and allow time-sensitive measurements such as in situ heating.

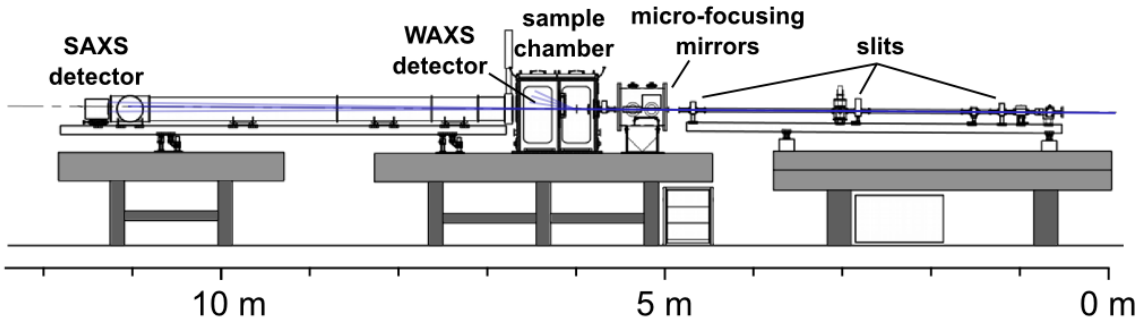


***Figure 3.4.*** *Schematic of the long vacuum-compatible chamber of X9 beamline with both SAXS and WAXS detectors. (Images provided by Kevin Yager, staff scientist at CFN, and used with permission.*

GISAXS measurements require long sample to detector distances (~ 3.5 m) and vacuum systems so that scattering from the ambient air does not affect the measurement. WAXS detectors are usually positioned closed to the samples (< 300 mm). Figure 3.4 shows the typical detectors set up of GIWAXS/GISAXS measurements.

### 3.3.2 Scattering basic

As the X-ray travels through the thin film, it is diffracted based on the internal structure of the materials. The diffraction angle of the X-rays is related to the spacing of the crystallographic planes of the film through Bragg's law (equation 3.8), and the direction of the diffracted beam is related to orientation of the planes.

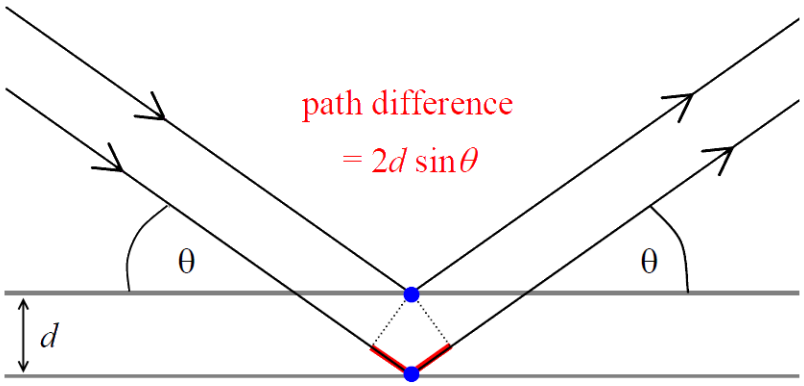


***Figure 3.5.*** *Geometrical construction for the derivation of Bragg's law. Scattering centers are shown as blue dots.*

Consider Figure 3.5 where a series of parallel X-rays strike a set of crystal planes at an angle θ and are scattered. Constructive interference will occur when the difference in the path lengths (highlighted in red) of the two interfering waves is equal to an integer number of

wavelength, $n\lambda$. From the geometric construction, this path length difference is also equal to $2dsin\theta$ where $d$ is the inter-planar spacing. Therefore, the diffraction occurs at the condition well-known as Bragg's law:

$$n\lambda = 2\,d\,sin\theta. \tag{3.8}$$

Hence, for a fixed wavelength (λ), a measure of the diffraction angles (peak position) will allow the associated d-spacing to be calculated. However, equation 3.8 could not tell anything about the scattering intensity.

In an X-ray scattering experiment, the scattered intensity is $I(\boldsymbol{q})$ given by:[6]

$$I(\boldsymbol{q}) \propto |F(\boldsymbol{q})|^2 \tag{3.9}$$

where $F(\boldsymbol{q})$ is the scattering amplitude. First, consider $N$ scattering points having different scattering amplitude $f_j$ and located at different distances $\mathbf{r}_j$ from one of the scattering points O selected as a reference as shown in Figure 3.6.

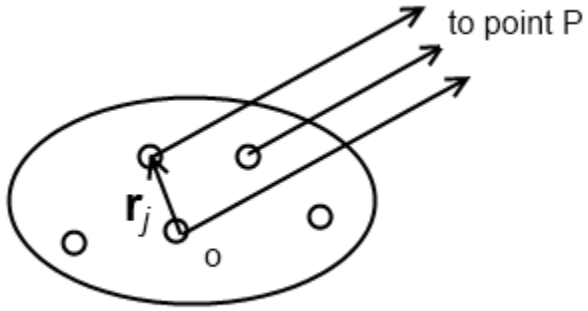


***Figure 3.6.*** *Geometry of scattering by several objects with vector* $\mathbf{r}_j$ *between them and the beams scattered in direction to point P.*

The relative phase difference between a wave scattered at the origin of the atom and one at the relative position $\mathbf{r}_j$ is:

$$\Delta\varphi(\boldsymbol{r}) = (\mathbf{k_f} - \mathbf{k_i}) \cdot \mathbf{r}_j = \boldsymbol{q} \cdot \mathbf{r}_j \tag{3.10}$$

where $\mathbf{q}$ is the scattering vector defined earlier as $\boldsymbol{q} = (\mathbf{k_f} - \mathbf{k_i})$. Then the amplitude from the N scattering points measured at point P is superposition of all N-amplitudes:

$$F(\boldsymbol{q}) = \sum_{j=1}^{N} f_j \exp i(\boldsymbol{q}\mathbf{r}_j). \tag{3.11}$$

For continuous density of scattering points $\rho(\mathbf{r})$, the scattering amplitude is an integral over the scattering volume in the three-dimensional r-space:

$$F(\boldsymbol{q}) = \int \rho(\boldsymbol{r}) e^{i\boldsymbol{q}\cdot\mathbf{r}} d\mathrm{V}. \tag{3.12}$$

Hence, the amplitude of scattering in point P is just a Fourier integral of the electron density function.

Now consider the scattering amplitude of N scattering objects, e.g. by molecules forming a molecular crystal, and write the scattering intensity:

$$I(\boldsymbol{q}) \propto |F(\boldsymbol{q})|^2 = F(\boldsymbol{q})F^*(\boldsymbol{q}) = \sum_j^N \sum_k^N f_j(\boldsymbol{q})\, f_k(\boldsymbol{q}) \exp i\boldsymbol{q}\,(\mathbf{r}_j - \mathbf{r}_k). \tag{3.13}$$

Here $\mathbf{r}_j$ and $\mathbf{r}_k$ are the same vectors corresponding to the distances shown in Fig. 3.6 and minus sign at $\mathbf{r}_k$ comes from the complex conjugation. Both summations are made from 1 to *N*. The same equation may be presented in another form:

$$|F(\boldsymbol{q})|^2 = \sum_{j=k}^{N} f_j(\boldsymbol{q}) f_k(\boldsymbol{q}) \exp i\boldsymbol{q}\left(\mathbf{r}_j - \mathbf{r}_k\right) + \sum_{j\neq}^{N} \sum_{k}^{N-1} f_j(\boldsymbol{q}) f_k(\boldsymbol{q}) \exp i\boldsymbol{q}\,(\mathbf{r}_j - \mathbf{r}_k). \tag{3.14}$$

In the first *N* terms $j = k$, $\boldsymbol{q}\left(\mathbf{r}_j - \mathbf{r}_k\right) = 0$ and, this sum corresponds to the intensity coming from the individual atoms or molecules without interference or diffraction. Thus, the first term becomes $f_j(\boldsymbol{q}) f_k(\boldsymbol{q}) = N F_{form}^2(\boldsymbol{q})$ and is known as **form factor**. For identical objects,

$f_j(\boldsymbol{q})f_k(\boldsymbol{q}) = NF_{form}^2(\boldsymbol{q})$ can also be extracted from the second term and the equation (3.14) take the following form:

$$I(\boldsymbol{q}) \propto NF_{form}^2(\boldsymbol{q})(1 + \sum_{j\neq}^{N}\sum_{k}^{N} \exp i\boldsymbol{q}\left(\mathbf{r}_j - \mathbf{r}_k\right) = NF_{form}^2(\boldsymbol{q})S(\boldsymbol{q}) \qquad (3.15)$$

where $S(\boldsymbol{q}) = \left[1 + \sum_{j\neq}^{N}\sum_{k}^{N} \exp i\boldsymbol{q}\left(\mathbf{r}_j - \mathbf{r}_k\right)\right]$ is known as **structure factor** and is determined by relative positions of the objects (atoms or molecules) in a materials. The peak in intensity will be observed when the term $\boldsymbol{q}\left(\mathbf{r}_j - \mathbf{r}_k\right) = 2\pi m$, where $m$ is the integer.

### 3.3.2 GIWAXS

GIWAXS measurements on the thin films of polymers can provide information about the molecular packing structure, crystallinity, size and orientation of crystalline domains. In order to obtain information on these molecular structures with typical size in the range of ~0.3 nm to ~3 nm, X-ray scattering measurements at large angle, typically >1°, are necessary due to the Bragg condition (equation 2.8).

Bragg's law in real space is equivalent to the Laue condition in reciprocal space which states that diffraction occurs when the scattering vector (**q**) is equal to a reciprocal lattice vector (**G**):[6]

$$\mathbf{q} = \mathbf{G} \qquad (3.9)$$

In this case, lattice spacing ($d$) can be simply calculated as $2\pi/q_o$, where $q_o$ is the diffraction peak position in reciprocal space.

From the diffraction pattern, the orientation of the crystalline domains can also be determined since the direction of the reciprocal lattice vectors depend on that of crystallographic planes. As shown in Figure 3.7 (a), for a film with isotropic crystal orientation the diffraction pattern will form a uniform ring on the 2D detector. For a film with a preferred out-of-plane orientation where the crystallographic planes stack parallel to the surface, the diffraction pattern will consist of spots for each crystallographic plane for a narrow orientation distribution (see Figure 3.7 (b)). The diffraction peak will resemble arcs instead of a spot for a broader orientation distribution (see Figure 3.7 (c)). For a film with both in-plane and out-of-plane orientation, only a small number of diffraction spots will be observed depending on the sample rotation with respect to the incident angle since the sample must be rotated such that the Bragg condition is met.

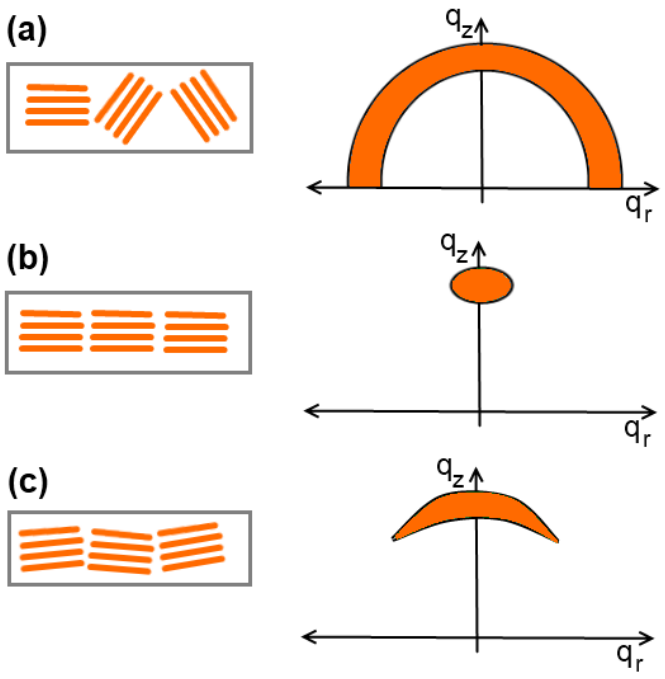


***Figure 3.7.*** *Schematics of the orientation of real space lattice plains and resulting diffraction patterns for different microstructures. (a) Randomly oriented crystallites, (b) highly oriented crystallites in out-of-plane direction, and (c) crystallites with broad orientation distribution.*

While the lattice spacing is obtained from the diffraction peak position, the size of the crystalline domains ($\xi$) of the materials under study can be determined from the full width at half-maximum (FWHM) of a diffraction peak via Scherrer's formula:[11]

$$\xi = K\lambda/(FWHM \times \cos(\theta)), \tag{3.10}$$

where λ is the X-ray wavelength and $\theta$ is the Bragg angle defined in Figure 3.5. In reciprocal space, it can be calculated as[12]

$$\xi = 2\pi K/\Delta q, \tag{3.11}$$

where $\Delta q$ is the FWHM of the diffraction peak in reciprocal space. The Scherrer constant $K$ is derived as $K = 2[2\ln(2)/\pi]^{1/2} \cong 0.93$ for the crystallites with cubic shape and it varies from 0.886 from 1.123 depending on the shape of the crystallites.[12]

In general there is also instrumental broadening arising from the slit dimensions and spread in the wavelength or angular distribution. However, polymer materials studies in this thesis are not precisely crystalline. They are small crystallites embedded in an amorphous matrix, where the crystalline peaks are broad. Therefore, the instrumental corrections can be neglected.

### 3.3.3 GISAXS

The demand for the characterization of nanostructured periodic surfaces with the length scale of 100-1000 nm has increased in recent years due to the rapid progress in the field of nanotechnology.[13-16] Direct imaging techniques such as atomic force microscopy (AFM) and scanning electron microscopy (SEM) are useful in characterizing the surface morphology and the lateral periodicity of the such structures but limited due to the very small scan area (μm range)

and the inability to determine buried and internal structural features. In contrast, GISAXS is able to determine sample surface structures as well as inner electron density variations of the deposited material. Moreover, GISAXS offers the possibility to carry out *in situ* experiments. For instance, the real time structural evolution in polymer thin films during the thermal annealing process could be observed.

In contrast to GIWAXS, GISAXS data is recorded at very small in-plane scattering angle (typically <1°). This angular range contains information about the shape and size of nanostructure and GISAXS is capable of delivering structural information of nanostructures between ~5 nm and ~50 nm, of repeat distances in ordered systems of up to ~250 nm.

## 3.5 References


1. Speakman, J. C., The Discovery of X-Ray-Diffraction by Crystals. *J Chem Educ* **1980,** 57, (7), 489-490.
2. Heeger, A. J., Semiconducting polymers: the Third Generation. *Chem Soc Rev* **2010,** 39, (7), 2354-2371.
3. Ezquerra, T. A., *Applications of synchrotron light to scattering and diffraction in materials and life sciences*. Springer: Berlin, 2009; p xvi, 318 p.
4. Grider, D. E.; Wright, A.; Ausburn, P. K., Electron-Beam Melting in Microfocus X-Ray Tubes. *J Phys D Appl Phys* **1986,** 19, (12), 2281-2292.
5. Shaheen, S. E.; Brabec, C. J.; Sariciftci, N. S.; Padinger, F.; Fromherz, T.; Hummelen, J. C., 2.5% efficient organic plastic solar cells. *Appl Phys Lett* **2001,** 78, (6), 841-843.
6. Als-Nielsen, J.; McMorrow, D., *Elements of modern X-ray physics*. Wiley: New York, 2001; p xi, 318 p.
7. Tolan, M., *X-ray scattering from soft-matter thin films : materials science and basic research*. Springer: Berlin ; New York, 1999; p viii, 197 p.
8. Busch, P.; Rauscher, M.; Smilgies, D. M.; Posselt, D.; Papadakis, C. M., Grazing-incidence small-angle X-ray scattering from thin polymer films with lamellar structures-the scattering cross section in the distorted-wave Born approximation. *J Appl Crystallogr* **2006,** 39, 433-442.
9. Brabec, C. J.; Cravino, A.; Meissner, D.; Sariciftci, N. S.; Fromherz, T.; Rispens, M. T.; Sanchez, L.; Hummelen, J. C., Origin of the open circuit voltage of plastic solar cells. *Adv Funct Mater* **2001,** 11, (5), 374-380.

10. Goetzberger, A.; Hebling, C.; Schock, H. W., Photovoltaic materials, history, status and outlook. *Mat Sci Eng R* **2003,** 40, (1), 1-46.

11. Warren, B. E., *X-ray diffraction*. Dover ed.; Dover Publications: New York, 1990; p vii, 381 p.

12. Smilgies, D. M., Scherrer grain-size analysis adapted to grazing-incidence scattering with area detectors. *J Appl Crystallogr* **2009,** 42, 1030-1034.

13. Wang, C. Q.; Jones, R. L.; Lin, E. K.; Wu, W. L.; Leu, J., Small angle x-ray scattering measurements of lithographic patterns with sidewall roughness from vertical standing waves. *Appl Phys Lett* **2007,** 90, (19).

14. Wang, C. Q.; Fu, W. E.; Li, B.; Huang, H.; Soles, C.; Lin, E. K.; Wu, W. L.; Ho, P. S.; Cresswell, M. W., Small angle X-ray scattering measurements of spatial dependent linewidth in dense nanoline gratings. *Thin Solid Films* **2009,** 517, (20), 5844-5847.

15. Wang, C. Q.; Jones, R. L.; Lin, E. K.; Wu, W. L.; Ho, D. L.; Villarrubia, J. S.; Choi, K. W.; Clarke, J. S.; Roberts, J.; Bristol, R.; Bunday, B., Line edge roughness and cross sectional characterization of sub-50 nm structures using critical dimension small angle x-ray scattering. *Aip Conf Proc* **2007,** 931, 402-406.

16. Wang, C. Q.; Jones, R. L.; Lin, E. K.; Wu, W. L.; Rice, B. J.; Choi, K. W.; Thompson, G.; Weigand, S. J.; Keane, D. T., Characterization of correlated line edge roughness of nanoscale line gratings using small angle x-ray scattering. *J Appl Phys* **2007,** 102, (2).

17. Meyer, A. Form Factor. http://www.gisaxs.de/theory2.html (April 4, 2012),

# CHAPTER 4

## Structural Studies of P3ATs Thin Film

### 4.1 Introduction

The electrical properties of films of semiconducting polymers are closely related to their molecular structure and intermolecular interactions. As discussed in chapter 2, electrical transport in a thin film of semiconducting polymers requires not only transport along single polymer chains, but also transport from one chain to another. Thus, molecular packing is an important factor in determining the electrical properties of semiconducting polymers and it is important to understand how these materials organize in thin films and whether this information can be used to determine their structure-function properties.

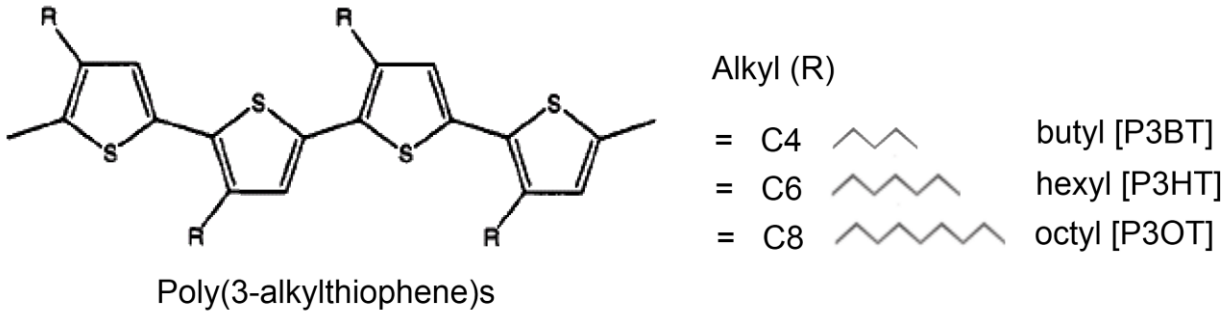


***Figure 4.1.*** *Schematic of molecular structure of Poly(3-alkylthiophene)s with three different side chain lengths (alkyl = butyl [P3BT], hexyl [P3HT], octyl [P3OT]).*

Among the semiconducting polymers, Poly(3-alkylthiophene)s (P3ATs) has attracted considerable attention because the alkyl modification can improve the solubility and processability of the polymers without altering their stability and electrical conductivity. These properties have made P3ATs, promising candidates for technological applications such as

organic photovoltaic, field-effect transistors, and sensor devices.[1-3] In BHJ OPV devices, it has been shown that the processing conditions have strong influence on device performance[4] and devices must either be annealed at elevated temperatures, typically 150 °C, or exposed to the solvent vapors such as toluene to obtain high efficiency. However, the details of how such processing affects the structural rearrangement of polymer remains unclear.

Previous X-ray scattering studies have been carried out to understand the morphology of P3HT thin films[5, 6] and P3HT/PCBM blends[7]. Solvent annealing in P3HT films has been explored by Jaczerska and coworkers[8] using in-situ optical interferometeric methods for regioregular and regiorandom films of several different P3AT exposed to cyclohexane, tetrahydrofuran, and choloroform. At about 25% of the saturated vapor pressure they found that the film thickness expanded by 5-6% for regioregular P3HT and by 3-5% for regioregular P3DDT. Whereas most solvent annealing is carried out subsequent to spin coating, a method has been developed by Kim[9] and coworkers to control the solvent vapor pressure during spin-coating. Here it was found that the length of the P3HT nanowires could be increased at the higher vapor pressures. On the basis of ex-situ x-ray studies it was concluded that the crystallinity of the materials improved with higher vapor pressure. In these two studies, the structural measurements were carried out ex-situ.

In this chapter, the studies of the molecular packing of P3AT thin films at room temperature are first presented. This is followed by a discussion of the results of in-situ x-ray scattering studies on P3HT thin films during the thermal and solvent vapor annealing processes. For solvent vapor annealing, the studies were carried out both at room temperature and elevated temperatures under sealed conditions where the solvent's vapor pressure increases significantly.

## 4.2 Experimental

P3AT powders were purchased from American Dye Source and Rieke Metal. For each P3AT, 2 wt. % solution was prepared by dissolving in chlorobenzene (Sigma-Aldrich) and filtered using PTFE syringe filter (pore size 0.45 μm). Silicon wafers were cut (~ 15 mm x 15 mm) and cleaned with 10 minute oxygen plasma etch. The solutions were then spin-coated onto silicon wafers at 700 rpm for 45 sec and dried in an enclosed sample carrier for ~15-20 min to obtain ~ 100 nm thick film. The film thicknesses were measured using a optical ellipsometer and Dektak Stylus profilometer.

The structure of the P3AT films were studied by GIWAXS at the National Synchrotron Light Source at Brookhaven National Laboratory using three different beam lines, X21, X22B and X9. Each beam line has different wavelengths and hence different incident angles were chosen so that the entire depth of the films could be probed. The experimental setup at these beam lines was described in detail in Chapter 3.

A custom built sample stage (Figure 4.2) was used for in situ heating experiments. A temperature controller (Lakeshore S331) was used to apply the appropriate voltage to the bullet heater (Sunrod cartridge heater, H062-20) and measure the temperature with Pt 100 temperature sensor (Lakeshore PT-103). The films were heated at a rate of 10 °C $min^{-1}$ to the desired temperature and allowed to equilibrate at each temperature for 10 minutes before the collection of data.

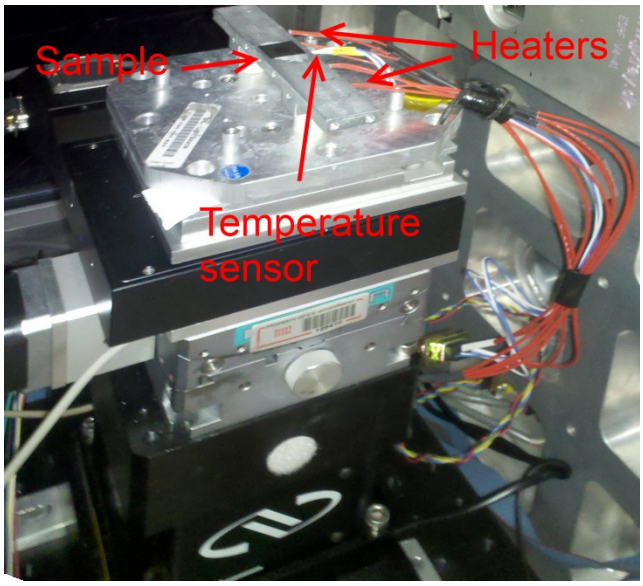


***Figure 4.2.*** *Custom built heater stage with bullet heater and Pt 100 temperature sensor. The sample stage located under the heater stage allows the precise control of incident angle as well as azimuthal rotation angle.*

For in situ solvent annealing experiments, a custom built chamber with beryllium tubular section was utilized. Beryllium was chosen due to its excellent X-ray transparency and high-pressure stability. The beryllium tubular section was sandwiched between the top and bottom aluminum disks, which can be heated to 200 ˚C. The temperature was determined by use of a Pt 100 temperature sensor located inside the sample holder disk. The chamber was fitted with pressure release valve set at 3 bar to prevent over pressurization. The sample was placed on an aluminum disk attached to the bottom plate and a reservoir of the liquid solvent, typically 1-2 ml of toluene, was placed in the trenches surrounding the aluminum disk. Under the sealed condition with sufficient liquid reservoir, the vapor pressure of toluene increased with increasing temperature reaching ~1.3 bar at 135 ºC.[10] During the cooling cycle, condensation and dripping of the liquid on the sample from the top cover plate was minimized by using a slow cooling rate

and an aluminum foil cover on the sample. In some measurements, the solvent was removed from the chamber at elevated temperature by evacuating the vapor with a pump.

## 4.3 Results

### 4.3.1 Molecular packing structure of P3ATs

The repeat unit of most semiconducting polymers consist of one or more aromatic rings and non-conjugated side chains are added to the basic repeat unit to increase the solubility in common solvents. This combination of conjugated and non-conjugated regions leads to ordered structures due to the phase separation of these two regions. [11, 12] Semiconducting polymers may arrange in either lamellar or hexagonal structure (see Figure 4.3) depending on the molecular structure of the side chains and their attachment to the conjugated backbones.[13] It is usually not possible to determine a unique unit cell of the semi-crystalline polymers from X-ray data since only a few scattering peaks are observed. However, the scattering data can be used to form a basic understanding of the packing structure based on the known molecular structure of the polymer.

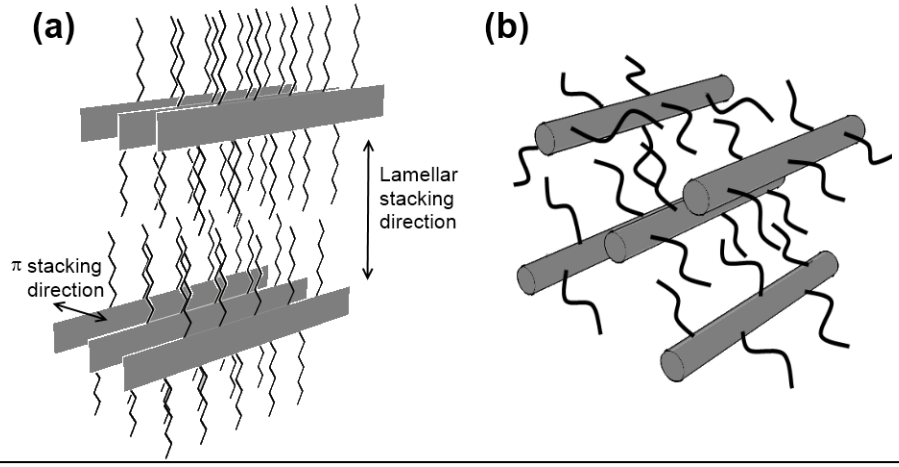


***Figure 4.3.*** *Schematic of (a) lamellar and (b) hexagonal packing of conjugated polymers. The lamellar stacking and π-stacking direction are indicated for the lamellar packing.*

The GIWAXS measurements were carried out on the P3AT thin films with three different side chains lengths (alkyl = butyl [P3BT], hexyl [P3HT], octyl [P3OT]). Typical 2D GIWAXS diffraction patterns acquired on thin films of P3BT, P3HT and P3OT deposited on Si substrate are shown in Figure 4.4 (a), (b) and (c) respectively. Previous studies on the structures of P3ATs by several groups[14-17] have confirmed the semicrystalline nature of the materials where the crystalline domains are embedded in the amorphous regions. The crystalline fraction forms lamellar structure where flexible side chains separate the stiffer polythiophene backbones and the lamellar spacing is determined by the alkyl side chain length. In the diffraction patterns of P3ATs (figure 4.4 a-c), the appearance of a well-defined (100) peak along the $q_z$ direction indicated that the lamellar stacking direction was predominately aligned along the surface normal direction. Second- and third-order reflection, (200) and (300), were visible only in P3HT and P3OT due to the higher X-ray intensity of the X9 beamline where these experiments were carried out. With increasing side chain length, the position of the (100) peak moved to the lower $q_z$ indicating a larger lamellar spacing for the longer side chains as expected. The (100) peak from the P3HT film appeared as arcs indicating that the films were not highly oriented whereas (100) peaks from both P3BT and P3OT had less angular distribution. The low intensity beam line used for measuring P3BT film does not affect the angular distribution of the (100) peak. The (010) peak, originated from the π-π stacking of the polymer backbones, was observed along $q_r$ in the scattering pattern of P3HT indicating that the π-π stacking direction was parallel to the substrate. In all P3ATs films, the invariance of the scattering patterns with azimuthal sample rotation verified the absence of preferred in-plane orientation.

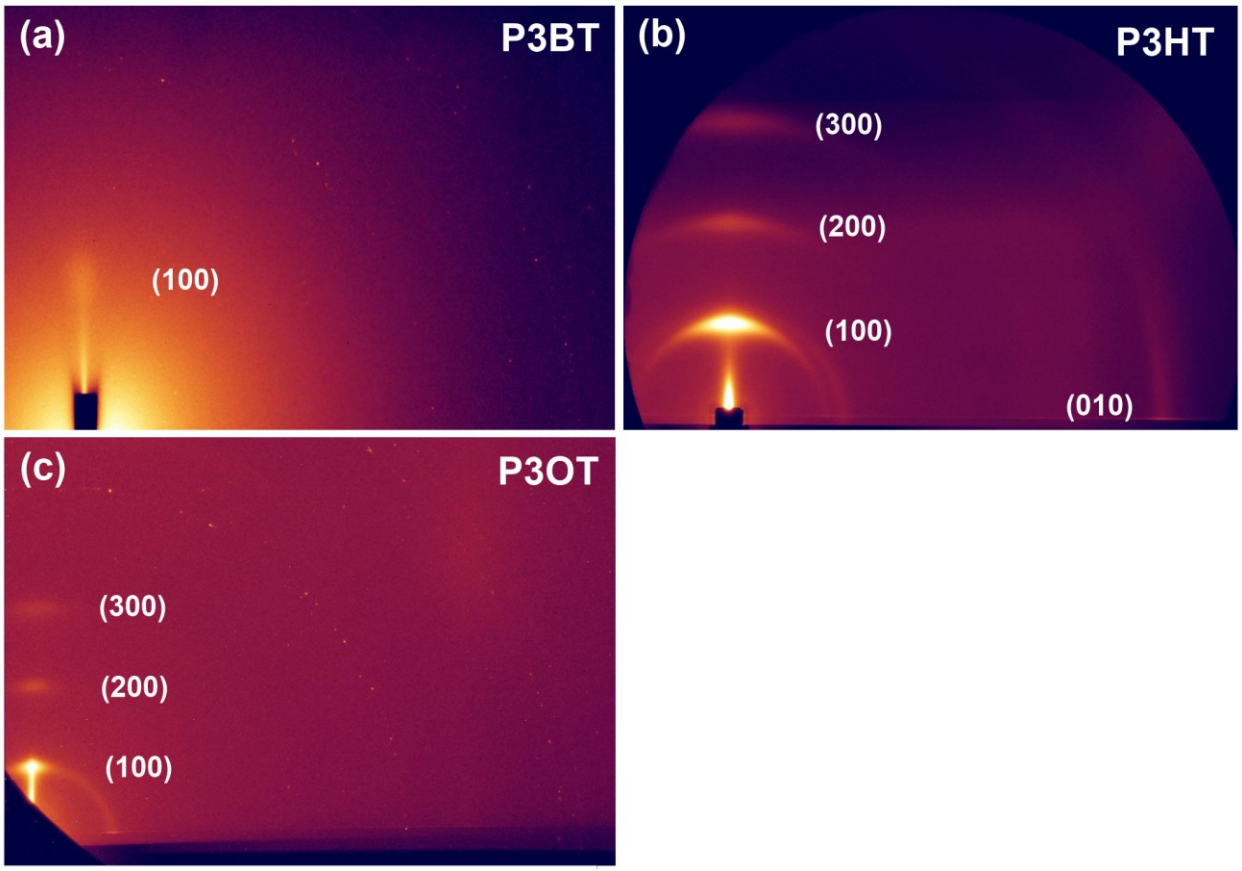


***Figure 4.4.*** *Typical 2-dimensional grazing-incident wide-angle X-ray scattering patterns from (a) P3BT, (b) P3HT and (c) P3OT which adopt a lamellar packing structure on Si substrate. The diffraction peaks are labeled in the images. Second- and third-order reflection, (200) and (300), were visible only in P3HT and P3OT due to the higher X-ray intensity of the X9 beamline where these experiments were carried out. The measurements on P3BT samples were carried out at X22B beamline.*

To investigate the molecular packing of the P3ATs in detail, radial scattering profiles were extracted along the (100) peak from the 2D scattering patterns such as those shown in Figure 4.4. Representative scattering profiles, displayed as open circles in Figure 4.5, were fitted to a Gaussian profile with a smoothly varying background (solid line). The layer spacing ($a$) was calculated from the Gaussian's center ($q_o$) by $a = {}^{2\pi}/_{q_o}$ and the coherence length ($\zeta$), a value

associated with the average grain size, was calculated from the FWHM obtained from the Gaussian fits with a Scherrer constant K = 1, as discussed in Chapter 3.

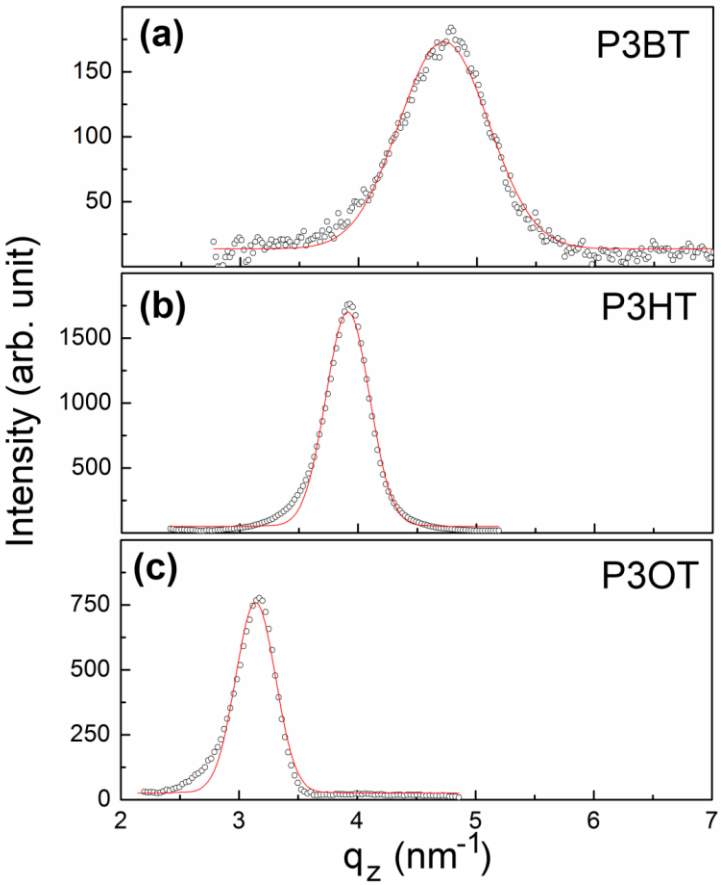


***Figure 4.5.*** *Radial scattering profiles (open circles) along the ⟨100⟩ directions extracted from the 2D scattering patterns of (a) P3BT, (b) P3HT, and (c) P3OT with the corresponding Gaussian fits (solid lines).*

The layer spacing of the P3BT, P3HT and P3OT were 1.32 nm, 1.61 nm and 2.02 nm respectively. The corresponding coherence lengths were 6 nm, 13 nm and 14 nm indicating that the coherence length also increased with increasing side chain length. For P3HT, a π-π stacking distance of 0.382 nm and a coherence length of ~9 nm were obtained from the scattering profiles of the (010) peaks.

Another important factor contributing to the crystallinity of the P3AT domains is how the side chains are packed within the lamellar layers of P3ATs. While many studies agreed that thin films of P3ATs form lamellar structures, it is unclear whether the side chains are interdigitated (Figure 4.6 a) or form an end-to-end structure (Figure 4.6 b). Schematics showing interdigitation[3, 18, 19] and discussion about interdigitation effects on morphology[20] appeared in literature although there were no reports confirming the interdigitation of side chains. The scattering data from individual P3AT was not sufficient to discriminate between the two different side chain packing structures. However, it can be determined indirectly by plotting the lamellar spacing as a function of side chain length as shown in Figure 4.6 c. Similar analysis has been successfully applied in confirming the side chain packing of conjugated polymer[21] as well as non-conjugated rigid rod polymers.[23, 24]

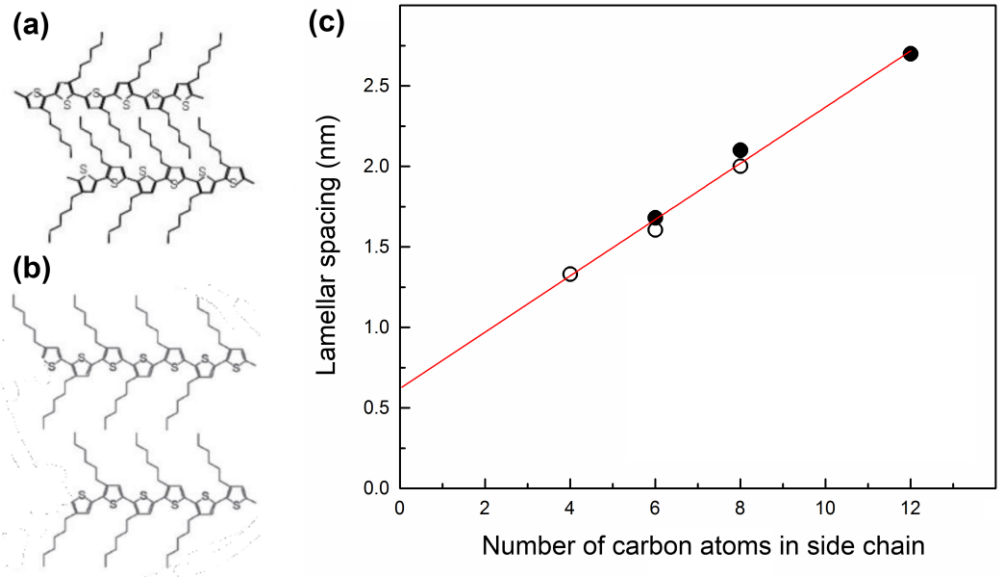


***Figure 4.6.*** *Schematic of lamellar packing structure with (a) interdigitated and (b) end-to-end side chains. (c) Lamellar spacing as a function of side chain length for P3ATs. The lamellar spacings for P3BT, P3HT and P3OT, obtained from the fit of the scattering data presented above, is shown in open circle. Spacing for P3HT, P3OT and P3DT, obtained from the reference 23, is shown as filled circle. The solid line is the linear fit of the data points.*

The lamellar spacing of P3BT, P3HT and P3OT were determined from the GIWAXS data as discussed in previous section. The lamellar spacing of P3HT, P3OT and P3DT, obtained from reference 25[25], was added to provide more data points for fitting the slope. The lamellar spacing exhibits a linear relationship with side chain length with a slope of 0.17 ± 0.01 nm with a *y*-intercept of 0.60 ± 0.05 nm (Figure 4.6 c). For end-to-end structures, the slope should be ~ 0.25 nm per carbon atom since each methylene ($CH_2$) unit should add ~ 0.125 nm. For interdigitated structures, the slope should be close to ~0.125 nm per carbon. However, these values should be taken as the upper limit since the tilt of the chains relative to the backbone can lower the slope. Therefore, the slope of 0.17 nm from Figure 4.6 (c) suggests an end-to-end packing structure for P3ATs' side chain. The intercept of ~ 0.6 nm is consistent with the molecular dimension of the backbone as well as the value obtained from a simple calculation based on the volume contribution of the alkyl region and the conjugated core region of the unit cell of P3HT described in the next section. This end-to-end structure is further supported by infrared spectroscopy that shows that the alkyl chains of the P3ATs are likely to be in the intermediate states between the all trans, crystalline structure and disordered liquid-like structure.[26]

The lack of interdigitation in P3ATs side chains is probably due to the high attachment density of the side chains (one side chain per two aromatic rings) to the polymer backbones since other conjugated polymer such as pBTTT and PQT-12 which have one side chain per four aromatic rings exhibit interdigitated side chain packing structure. [21, 27, 28] Without side chain interdigitation, correlation between P3HT lamellar layers could not extend very long leading to the small P3ATs domain sizes (<20 nm). In contrast, interdigitated side chains of the PQT and pBTTT polymer preserves the correlation of the lamellar layers resulting in the greatly increased domain size (up to micrometers).[21]

### 4.3.2 Thermal annealing of P3HT thin films

Current P3HT based devices are mainly fabricated by spin-coating or blade-coating and hence thin film formation involves a complex process of solvent evaporation and molecular aggregation. This relatively fast film forming process may kinetically limit the formation of crystalline domains and post-annealing provides a way to re-organize the polymer chains in the film and remove the packing defects after deposition. In the following section, the structural changes in the P3HT thin film during thermal annealing process was studied in detail by probing the lamellar spacing (lattice constant *a*) and π-π stacking distance (lattice constant b) as a function of temperature. The lattice constant a and b were determined from the peak position of the (100) and (010) scattering peaks respectively as discussed in the previous section.

Typical 2D GIWAXS diffraction patterns acquired on 100 nm thick P3HT thin films deposited on Si substrate at 27 ºC and 185 ºC are shown in Figure 4.7 (a) and (b) respectively. Figure 4.7 (c) shows the 1D line scans extracted along the ⟨100⟩ direction from the scattering patterns at 27 °C and 185 °C and the variation in intensity, width and position of the (100) peaks between the two temperatures can be clearly observed. At 185 ºC, the (100) peaks exhibited higher intensity and sharper peaks indicating the improvement of ordering in out-of-plane direction. Due to thermal expansion, the positions of the peaks also shifted towards lower $q_z$. However, the orientation of the P3HT domains remained the same at high temperature.

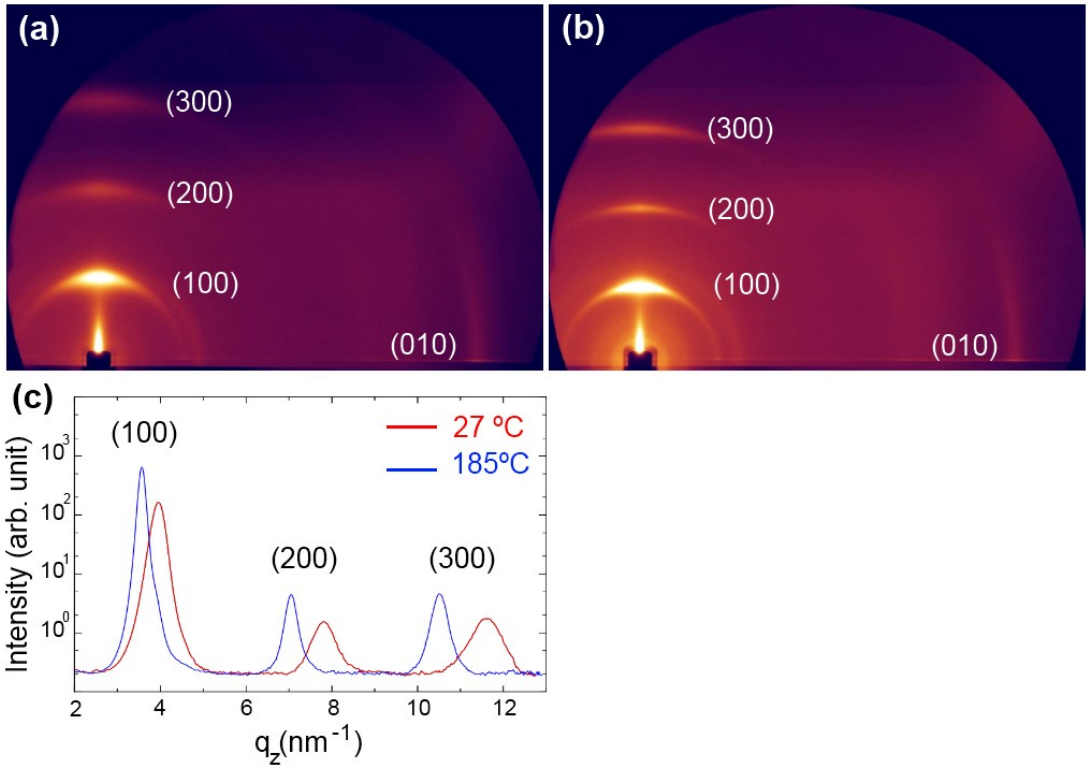


***Figure 4.7.*** *Typical x-ray grazing incident angle x-ray scattering pattern from a 100 nm thick film of P3HT at (a) 27 ºC and (b) 185ºC. The diffraction peaks are labeled in the images. (c) Comparison of line scans along the ⟨ 100⟩ directions at these two temperatures.*

In order to study the structural changes in the P3HT thin film during thermal annealing process, the scattering pattern was obtained both in heating and cooling cycles at intervals of 10-20 ºC. At each temperature the sample was equilibrated for 10 minutes before acquiring the scattering pattern. The lattice constant ($a$) and coherence length ($\zeta$) extracted from the scattering profile of (100) peak are plotted against temperature in Figure 4.8 (a) and (b).

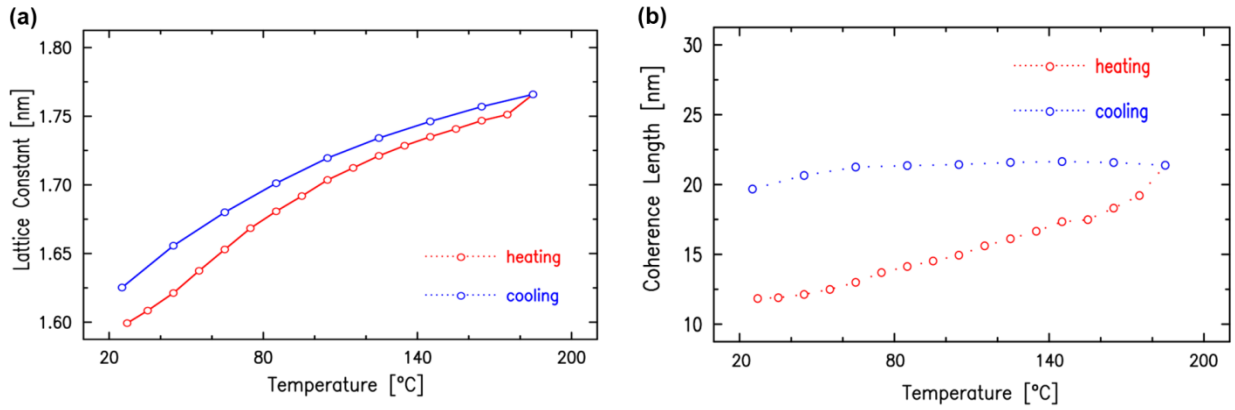


***Figure 4.8.*** *Thermal behavior of pure P3HT films. (a) The lattice constant and (b) coherence length of the (100) peak as a function of temperature during in situ thermal annealing. Results were obtained both for heating (red) and cooling (blue).*

At 27 ºC, the lattice constant (*a*) of the as-cast film was 1.59 nm, consistent with previous results.[4,21] The lattice constant increased monotonically with increasing temperature and reached 1.76 nm at 185 ºC, a ~10% increase from room temperature value. Upon cooling, the lattice constant decreased monotonically, but did not completely return to the original value from the as-cast film. The lattice constant measured during the cooling cycle was always a few percentage higher than the lattice constant during the heating cycle. Waiting longer than 10 minutes to equilibrate the temperature did not reduce the hysteresis. At 27 ºC, after the cooling cycle, the lattice constant (*a*) was 1.62 nm, slightly higher than the as-spun film value. It indicated that improved ordering of the alkyl chains during the heating cycle led to a more extended conformation of the alkyl chains and hence a larger layer spacing after annealing.

The coherence length, a value often associated with the average grain size, was 13 nm for as-spun film at 27 ºC. This corresponded to about 8 lamellar layers in out of plane direction. The coherence length increased with increasing temperature and it reached 21 nm at 185 ºC, corresponding to the about 13 lamellar layers. Unlike lattice constant, there was very little

corresponding change in the coherence length when the temperature was subsequently lowered indicating that improvement in the coherence length was irreversible.

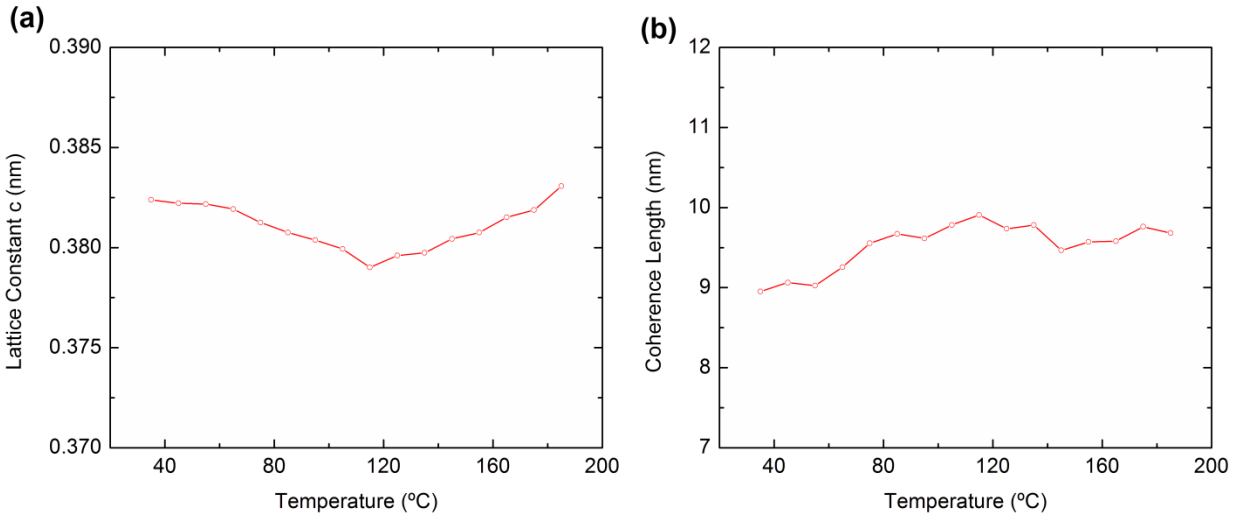


***Figure 4.9.*** *(a) The lattice constant and (b) coherence length of the (010) peak as a function of temperature during in situ thermal annealing.*

Similar analysis was performed for the scattering profiles of the (010) peaks to obtain lattice constant *b* and coherence length of the P3HT domains parallel to the plane of substrate (Figure 4.9). In contrast to lattice constant *a*, the lattice constant *b* of the as-cast film initially contracted with increasing temperature up to ~120 °C and then expanded upon further annealing. A similar negative thermal expansion was also observed for other polymer system such as polyethylene, polypropylene and polyoxymethylene.[29] However, temperature dependence of lattice constant *b* was weak compared to lattice constant *a*. For the temperature range from 27 to 180 ºC, the variation in lattice constant *b* was less than 1% compared with the ~10% change in lattice constant *a*. Similarly, there was only a small improvement in the coherence length of the (010) peak upon annealing. The coherence length of the (010) peak was ~ 9 nm for as-spun film at 27 ºC and annealing to 185 ºC improves the coherence length by less than 1 nm.

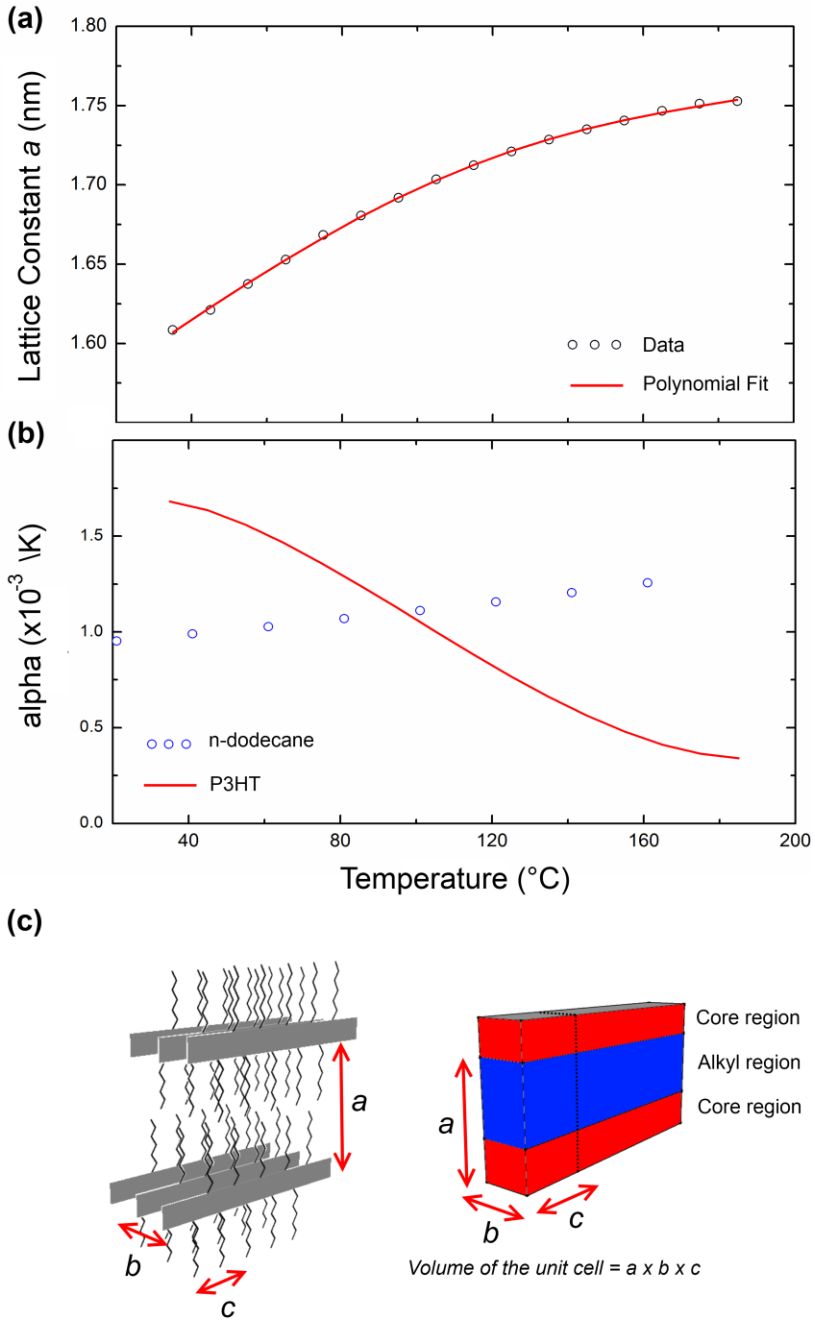


***Figure 4.10. (a)*** *The lattice constant a of P3HT (open circle) fitted with fourth-order polynomial(solid line).* ***(b)*** *The polynomial fit of the lattice expansion provides the thermal expansion coefficient of P3HT(solid) while the thermal expansion coefficient for n-Dodecane (open circle) is obtained from reference 22.* ***(c)*** *Molecular packing of the P3HT crystallite and corresponding schematic showing alkyl region and core region.*

In the following, a simple calculation based on the volume contribution of the alkyl region and the conjugated core region of the unit cell of P3HT crystallite showed that thermal

expansion of lattice constant *a* is mainly contributed by the expansion of alkyl side chains. In this calculation, the volume of the unit cell ($a \times b \times c$) was first divided into a volume filled entirely with alkyl chains and a volume occupied by the conjugated backbones (see Figure 4.10 (c)). The expected alkyl volume, 0.322 $nm^3$, in the crystalline phase of n-dodecane was calculated from the molecular weight (170.33 g/mol) by estimatin the density to be 0.88 $g/cm^3$. The density of the crystalline n-dodecane is estimated from the 0.186 $nm^2$ cross-sectional area of the alkyl chain in crystalline phase[32] and the 1.72 nm chain length.[33] An effective thickness of the alkyl region, 1.03 nm, was obtained by dividing the alkyl volume with the cross-sectional area of the unit cell ($b \times c = 0.383\ \text{nm} \times 0.82\ \text{nm} = 0.314\ \text{nm}^2$). The difference between the measured 1.61 nm lamellar thickness and the 1.03 nm effective thickness of the alkyl region is 0.58 nm, the thickness of the conjugated region. This is in good agreement with the 0.60 nm obtained from the intercept of the chain length dependent thickness (see 4.3.1). If the chains are assumed to be liquid with their corresponding lower density (0.75 $g/cm^3$), then the thickness of the conjugated region is about 0.40 nm, less than that found from the intercept discussed above.

In order to understand the anisotropy in the thermal expansion of P3HT domains, the temperature dependent lattice constant *a* was fitted with fourth-order polynomial to obtain the coefficient of thermal expansion ($\alpha$) as shown in Figure 4.10 (a). Assuming the rigid polymer backbone region did not expand, resulting thermal expansion coefficient of the ~$1.5 \times 10^{-3} K^{-1}$ was comparable to the thermal expansion coefficient of n-Dodecane[22] (~$1 \times 10^{-3} K^{-1}$) indicating that expansion of the P3HT lamellar layers was mostly due to the alkyl side chains. Thermal contraction was observed for the *b* axis up to 120 °C, but the absolute value of the corresponding coefficient is only ~10% of that of the *a*-axis. Hence, the net result was a volume expansion for P3HT.

The increase in the coherence length of the (100) peak indicates the growth of P3HT crystalline domains in out-of-plane direction while the relatively small changes in the coherence length of the (010) peak indicates that there are no changes to the size of crystallites in π-π stacking direction. Upon thermal annealing, the expanded P3HT lamellar layers may allow the polymer chains to become more mobile and slip within a given lamella leading to the crystallite growth in out-of-plane direction.

### 4.3.3. Solvent vapor annealing of P3HT thin films

Another proven approach to improve the electrical properties of P3HT thin film devices is solvent annealing.[9,30] In this process, solvent vapor was introduced to re-organize the polymer chains in the film and remove the packing defects after deposition. Most solvent annealing processes in the literature were carried out at room temperature by enclosing the samples in the Petri dishes filled with solvent vapor. Extended annealing time (up to 24 hours) were required to obtain significant improvement in structural properties of P3HT thin films.[9, 29, 30] In the following, the results of GIWAXS studies carried out in the presence of solvent vapors both at room temperature and elevated temperatures are presented. Although toluene vapor increases the background scattering, the positions and widths of the (100) peaks could be readily obtained.

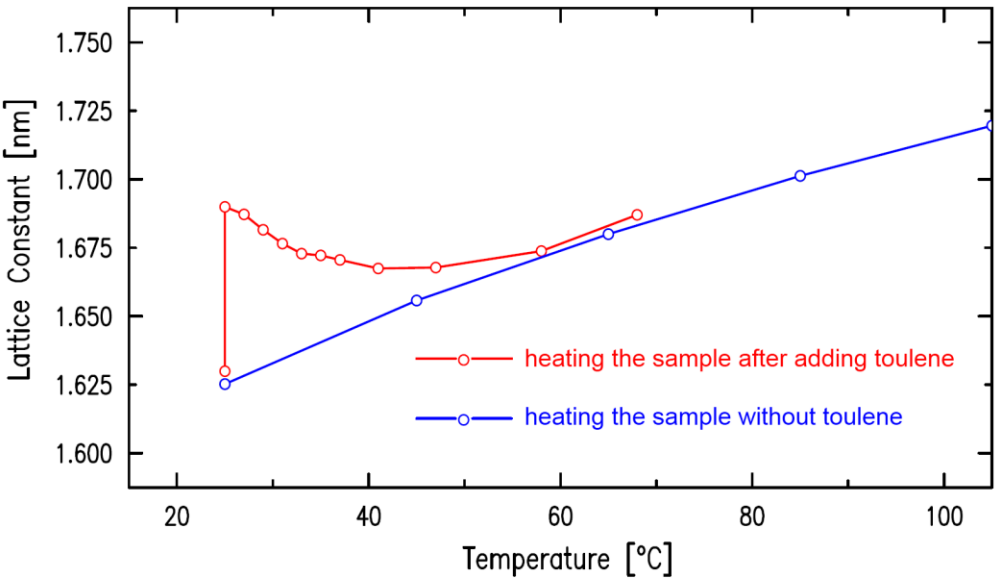


***Figure 4.11.*** *Thermal expansion of lattice constant a during the thermal annealing with and without toulene.*

Figure 4.11 shows the variation in the lattice constant *a* after introducing the toluene solvent. In the absence of solvent, the as-spun sample exhibited $a$ = 1.63 nm, similar to the thermal annealing sample. With the addition of toluene, the lattice constant increased to 1.68 nm. The expansion of 0.05 nm is much less than the size of a toluene molecule suggesting that only a small amount of solvent was adsorbed between the lamellar layers. No significant change in the coherence length of (100) peak was observed. Hence, at room temperature, P3HT layers expanded in the presence of solvent but did not improve their order, at least during the time of scattering experiment (up to ~1 hour). When the sample (not the whole cell) was heated up to elevated temperatures, the lattice constant *a* started to decrease indicating that the solvent molecules were driven out from the films. Therefore, for the subsequent studies, the whole cell was heated in a sealed condition in order to prevent the solvent molecules from leaving the thin film.

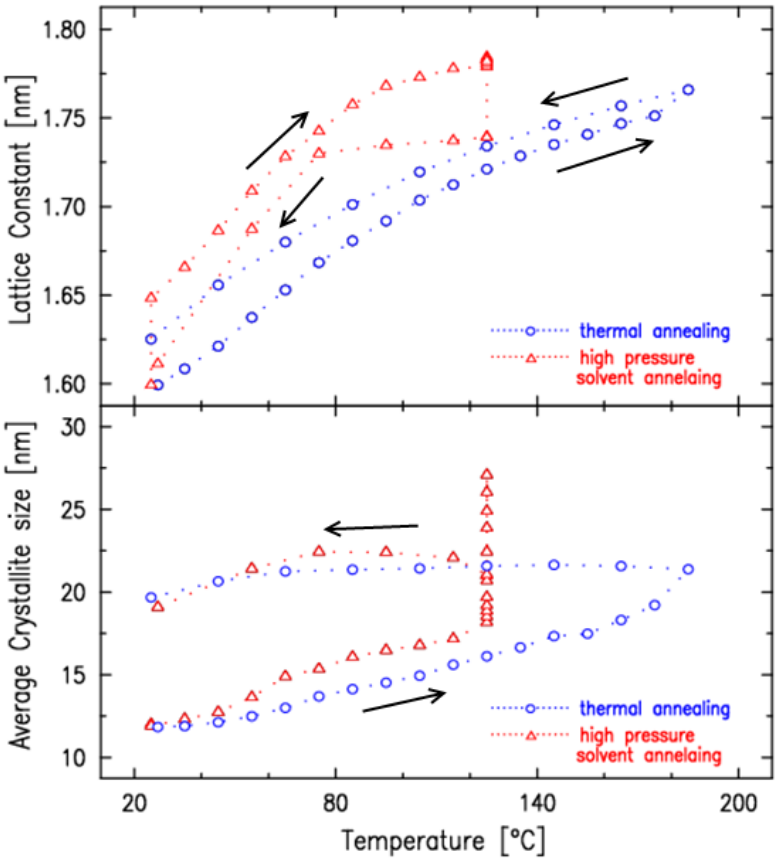


***Figure 4.12.*** *Temperature dependent lattice constant (top) and coherence length (bottom) obtained in the absence of toulene solvent (blue) and in the presence of toulene solvent (red). Results were obtained for both heating and cooling (indicated by black arrows).*

A sufficient quantity of toluene was placed in the bottom of the cell and as the temperature increased in the sealed cell the solvent's vapor pressure increased, achieving a pressure of 0.13 MPa at 135 ºC. The temperature dependent lattice constants and coherence lengths of (100) peaks were compared for dry annealing and pressurized solvent annealing in Figure 4.12. At room temperature, the lattice constant *a* increased from 1.6 nm to 1.65 nm with the addition of toluene, a similar relative increase as previous experiment. With increasing temperature, the lattice constant increased at a faster rate than in the case of the dry sample. The lattice constant appeared to saturate at ~ 1.77 nm at 135 ºC, an expansion of about 11% over the

dry value at 27 ºC. Note that the coefficient of thermal expansion was higher in the presence of solvent. After the toluene vapor was entirely removed from the cell at 135 ºC (pumping on the sealed cell) the lattice constant *a* was equal to 1.73 nm. This is nearly identical to the value obtained at the same temperature for the dry sample. The 0.04 nm expansion at 135 ºC in the presence of toluene is similar to that observed at 27 ºC. Upon cooling, the lattice constant was also slightly expanded compared with the as-spun sample. The temperature range of the solvent annealing experiment was limited to 135 ºC to avoid the over-pressurization of the beryllium sample cell.

Although the lattice expands slightly with the presence of the solvent at room temperature, the coherence length was virtually unchanged. Above 60 ºC a slight improvement in the coherence length was observed in the presence of solvent compared to the dry sample. However, the biggest improvement occurred at 135 ºC where the coherence length increased with equilibration time. After an equilibration time of 20 minutes, the coherence length improved from 17 to 25 nm. An equivalent improvement was not observed for the dry samples. This result suggested that solvent annealing at elevated temperature improved the order of P3HT in crystallite domains in comparison to either thermal or solvent annealing. However, the improved order was lost when the solvent was removed. Attempts to remove the solvent at a slower rate did not allow us to keep the better coherence observed in the presence of the solvent. However, the improvement in the coherence length provided by dry annealing at 180˚C can be obtained using pressurized toluene annealing at 135˚C.

## 4.4 Conclusion

The inner structure and morphologies of a P3BT, P3HT, and P3OT thin film on silicon substrate were characterized, and the packing of these polymers were correlated with the structure and alkyl side chain length of P3ATs. GIWAXS studies of the P3BT, P3HT, and P3OT thin film indicates that the inner part of each thin film had a well-ordered, multilayered structure with an edge-on orientation. Furthermore, the studies show that (1) with increasing temperature, in the absence of solvent that the P3HT layers expand significantly and improve their order, (2) that the coherence length provided by dry annealing at 180˚C can be obtained using pressurized toluene annealing at 135˚C, and (3) the large volume expansion is consistent with the calculated expansion based on that of the n-dodecane chains.

## 4.5 References


1. Gunes, S.; Neugebauer, H.; Sariciftci, N. S., Conjugated polymer-based organic solar cells. *Chem Rev* **2007,** 107, (4), 1324-1338.

2. Sirringhaus, H., Device physics of Solution-processed organic field-effect transistors. *Adv Mater* **2005,** 17, (20), 2411-2425.

3. Sirringhaus, H.; Tessler, N.; Friend, R. H., Integrated optoelectronic devices based on conjugated polymers. *Science* **1998,** 280, (5370), 1741-1744.

4. Li, G.; Shrotriya, V.; Yao, Y.; Huang, J. S.; Yang, Y., Manipulating regioregular poly(3-hexylthiophene): [6,6]-phenyl-C-61-butyric acid methyl ester blends - route towards high efficiency polymer solar cells. *J Mater Chem* **2007,** 17, (30), 3126-3140.

5. Joshi, S.; Grigorian, S.; Pietsch, U., X-ray structural and crystallinity studies of low and high molecular weight poly(3-hexylthiophene). *phys. stat. sol. (a)*, 2008; Vol. 205, pp 488-496.

6. Woo, C.; Thompson, B.; Kim, B.; Toney, M.; Fréchet, J., The Influence of Poly(3-hexylthiophene) Regioregularity on Fullerene-Composite Solar Cell Performance. *J. Am. Chem. Soc.*, 2008; Vol. 130, pp 16324-16329.

7. Ma, W.; Yang, C.; Gong, X.; Lee, K.; Heeger, A. J., Thermally Stable, Efficient Polymer Solar Cells with Nanoscale Control of the Interpenetraging Network Morphology. *Adv. Funct. Matt.* **2005,** 15, 1617-1622.

8. Jaczewska, J.; Raptis, I.; Budkowski, A.; Goustouridis, D.; Raczkowska, J.; Sanopoulou, M.; Pamuł, E.; Bernasik, A.; Rysza, J., *Swelling of P3HT films exposed to solvent vapors an humidity: Evaluation of solubility parameters*, 2007; pp 1-6.

9. Kim, D.; Park, Y.; Jang, Y.; Kim, S.; Cho, K., Solvent Vapor-Induced Nanowire Formation in Poly(3-hexylthiophene) Thin Films. *Macromol. Rapid Commun.*, 2005; Vol. 26, pp 834-839.

10. http://webbook.nist.gov/cgi/cbook.cgi?ID=C108883&Mask=4

11. Osterbacka, R.; An, C. P.; Jiang, X. M.; Vardeny, Z. V., Two-dimensional electronic excitations in self-assembled conjugated polymer nanocrystals. *Science* **2000,** 287, (5454), 839-842.

12. Sirringhaus, H.; Brown, P. J.; Friend, R. H.; Nielsen, M. M.; Bechgaard, K.; Langeveld-Voss, B. M. W.; Spiering, A. J. H.; Janssen, R. A. J.; Meijer, E. W.; Herwig, P.; de

Leeuw, D. M., Two-dimensional charge transport in self-organized, high-mobility conjugated polymers. *Nature* **1999,** 401, (6754), 685-688.

13. Stepanyan, R.; Subbotin, A.; Knaapila, M.; Ikkala, O.; ten Brinke, G., Self-organization of hairy-rod polymers. *Macromolecules* **2003,** 36, (10), 3758-3763.

14. Prosa, T. J.; Winokur, M. J.; McCullough, R. D., Evidence of a novel side chain structure in regioregular poly(3-alkylthiophenes). *Macromolecules* **1996,** 29, (10), 3654-3656.

15. Tashiro, K.; Kobayashi, M.; Kawai, T.; Yoshino, K., Crystal structural change in poly(3-alkyl thiophene)s induced by iodine doping as studied by an organized combination of X-ray diffraction, infrared/Raman spectroscopy and computer simulation techniques. *Polymer* **1997,** 38, (12), 2867-2879.

16. Xie, H. W.; Corish, J.; Morton-Blake, D. A., Thermochromic distortions in a poly(3-alkylthiophene): an atomistic simulation investigation. *Synthetic Met* **2000,** 113, (1-2), 65-72.

17. Yamamoto, T.; Komarudin, D.; Arai, M.; Lee, B. L.; Suganuma, H.; Asakawa, N.; Inoue, Y.; Kubota, K.; Sasaki, S.; Fukuda, T.; Matsuda, H., Extensive studies on pi-stacking of poly(3-alkylthiophene-2,5-diyl)s and poly(4-alkylthiazole-2,5-diyl)s by optical spectroscopy, NMR analysis, light scattering analysis, and X-ray crystallography. *J Am Chem Soc* **1998,** 120, (9), 2047-2058.

18. McCullough, R. D., The chemistry of conducting polythiophenes. *Adv Mater* **1998,** 10, (2), 93-98.

19. Kim, D. H.; Park, Y. D.; Jang, Y. S.; Yang, H. C.; Kim, Y. H.; Han, J. I.; Moon, D. G.; Park, S. J.; Chang, T. Y.; Chang, C. W.; Joo, M. K.; Ryu, C. Y.; Cho, K. W., Enhancement of field-effect mobility due to surface-mediated molecular ordering in regioregular polythiophene thin film transistors. *Adv Funct Mater* **2005,** 15, (1), 77-82.

20. Malik, S.; Nandi, A. K., Crystallization mechanism of regioregular poly(3-alkyl thiophene)s. *J Polym Sci Pol Phys* **2002,** 40, (18), 2073-2085.

21. Kline, R. J.; DeLongchamp, D. M.; Fischer, D. A.; Lin, E. K.; Richter, L. J.; Chabinyc, M. L.; Toney, M. F.; Heeney, M.; McCulloch, I., Critical role of side-chain attachment density on the order and device performance of polythiophenes. *Macromolecules* **2007,** 40, (22), 7960-7965.

22. Khasanshin, T. S.; Shchamialiou, A. P.; Poddubskij, O. G.; Thermodynamic Properties of Heavy n-Alkanes in the Liquid State: n-Dodecane, *Int. J of Thermophysics* **2003**, 24, (5), 1277-1289.

23. Ballauff, M., Stiff-Chain Polymers - Structure, Phase-Behavior, and Properties. *Angew Chem Int Edit* **1989,** 28, (3), 253-267.

24. Watanabe, J.; Harkness, B. R.; Sone, M.; Ichimura, H., Rigid-Rod Polyesters with Flexible Side-Chains .4. Thermotropic Behavior and Phase Structures in Polyesters Based on 1,4-Dialkyl Esters of Pyromellitic Acid and 4,4'-Biphenol. *Macromolecules* **1994,** 27, (2), 507-512.

25. Yang, C.; Orfino, F. P.; Holdcroft, S., A phenomenological model for predicting thermochromism of regioregular and nonregioregular poly(3-alkylthiophenes). *Macromolecules* **1996,** 29, (20), 6510-6517.

26. Gurau, M. C.; Delongchamp, D. M.; Vogel, B. M.; Lin, E. K.; Fischer, D. A.; Sambasivan, S.; Richter, L. J., Measuring molecular order in poly(3-alkylthiophene) thin films with polarizing spectroscopies. *Langmuir* **2007,** 23, (2), 834-842.

27. Ong, B. S.; Wu, Y. L.; Liu, P.; Gardner, S., High-performance semiconducting polythiophenes for organic thin-film transistors. *J Am Chem Soc* **2004,** 126, (11), 3378-3379.

28. I, M.; Heeney, M.; Bailey, C.; Genevicius, K.; I, M.; Shkunov, M.; Sparrowe, D.; Tierney, S.; Wagner, R.; Zhang, W. M.; Chabinyc, M. L.; Kline, R. J.; Mcgehee, M. D.; Toney, M. F., Liquid-crystalline semiconducting polymers with high charge-carrier mobility. *Nat Mater* **2006,** 5, (4), 328-333.

29. Barrera, G. D.; Bruno, J. A. O.; Barron, T. H. K.; Allan, N. L.; Negative thermal expansion. J. Phys. Cond. Matt. 17, R217 (2005).

30. Park, J. H.; Kim, J. S.; Lee, J. H.; Lee, W. H.; Cho, K., Effect of Annealing Solvent Solubility on the Performance of Poly(3-hexylthiophene)/Methanofullerene Solar Cells. *J Phys Chem C* **2009,** 113, (40), 17579-17584.

31. Li, G.; Yao, Y.; Yang, H.; Shrotriya, V.; Yang, G.; Yang, Y., "Solvent annealing" effect in polymer solar cells based on poly(3-hexylthiophene) and methanofullerenes. *Adv Funct Mater* **2007,** 17, (10), 1636-1644.

32. Kaganer, V. M.; Mohwald, H.; Dutta, P., Structure and phase transitions in Langmuir monolayers. *Rev Moder Phys* **1999,** 71, (3), 779-819.

33. Craievich, A. F.; Denicolo, I.; Doucet, J., Molecular motion and conformational defects in odd-numbered paraffins. Phys Rev B 1984, 30, (8), 4782-4787

# CHAPTER 5

## Morphological Studies of Nanoimprinted P3HT Thin Film

### 5.1 Introduction

Nanoimprinting provides a route for controlling the morphology of functional polymer nanostructures[1-5] in addition to its originally-intended application as a high-resolution lithographic technique.[6-8] Thin organic films, including light-emitting conjugated polymers,[1] block copolymers,[2] piezoelectric polymers,[3] and semicrystalline polymers[4, 5] have been directly patterned using nanoimprinting to obtain desired morphological features. More recent studies have shown that nanoimprinting can control the molecular chain configurations of liquid-crystalline polymers such as poly(9,9-dioctylfluorene-*co*-benzothiadiazole).[9] For thermoplastic fluoropolymers (*e.g.,* polyvinylidene fluoride), this method also induces preferential polymer chain alignment.[3, 10]

In this chapter, nanoimprinting as a means to control both the morphology and molecular chain orientation of thin-film conjugated polymers is investigated. These properties are inherently difficult to control in conjugated polymers such as poly-3(hexyl thiophene) (P3HT), and have a profound effect on the electrical and optical performance. For example, a thin film's molecular chain orientation depends on processing conditions such as the casting solvent, method of deposition (*e.g.*, spin coating, blade-coating), and substrate surface treatment.[11-14] P3HT films cast from slowly-evaporated solvents exhibit polymer chains oriented with their π-π stacking direction in the plane of the substrate and their corresponding side-chain induced lamellar structure stacked substrate-normal (figure 5.1(a), edge-on orientation), with the degree

of crystallinity, domain size, and orientation dependent on the polymer's molecular weight and regio-regularity.[14-16] In contrast, P3HT films cast from fast-evaporating solvents (*e.g.*, chloroform) have some degree of π-π stacking along the substrate-normal with their lamellar structure arranged substrate-parallel (figure5.1(b), face-on orientation) but with the polymer backbone randomly oriented in the surface plane.[11] The thermal stability of the face-on orientation has not been studied in detail, and it is possible that some of these structures are kinetically-trapped, rather than thermodynamically stable orientations. Controlling the P3HT polymer chain orientation is important because of its strongly anisotropic electrical conductivity, where the charge-carrier mobility in the plane of π-π stacking and the conjugated backbone can be several orders of magnitude higher than that in the lamellar stacking direction, where carriers must traverse the insulating P3HT alkyl chains.[13, 17] While an edge-on chain orientation is desirable for devices having in-plane charge transport (*e.g.*, transistors), a face-on orientation benefits architectures with charge transport normal to the substrate plane, such as solar cells or light-emitting diodes.

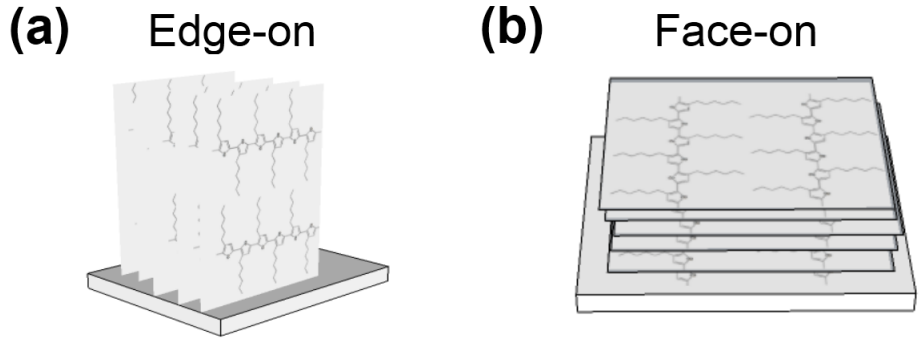


***Figure 5.1.*** *Schematics of (a) edge-on and (b) face-on orientation of P3HT domains*

This chapter presents results that show that nanoimprint methods can transfer topographical features from the imprint master to a P3HT film with high fidelity, and further that

the imprint process reorients some of the polymer material from edge-on to face-on. The P3HT backbones are also well-aligned along the grating direction. The utilization of a synchrotron x-ray source, coupled with area detectors and precise control of the sample angles, has enabled unambiguous mapping of the polymer chain orientation.

## 5.2 Experimental

### 5.2.1 Nanoimprint technology

Nanoimprint is an emerging lithography technology that promises high throughput patterning of nanostructures. Based on the mechanical replication process, nanoimprint can achieve pattern resolutions beyond the limitation set by the diffraction limit encountered in optical lithography.[18]

The nanoimprint process (figure 5.2. (a)) and imprint instruments (figure 5.2. (b) and (c)) are conceptually very simple. In principle, there are two basic versions of nanoimprint. One is based on the thermal embossing of thermoplastic polymers, while the other is based on UV-curable polymers. In thermal nanoimprinting, which we use for our experiments, the thermoplastic polymer is heated above the glass transition point of the polymer, a temperature where the polymer goes from a hard, glass like state to a soft, rubber like state[18] before the template is brought into contact with the polymer. Once the polymer has filled all the cavities of the template, the substrate and the template are cooled down to room temperature and the template is separated from the substrate.

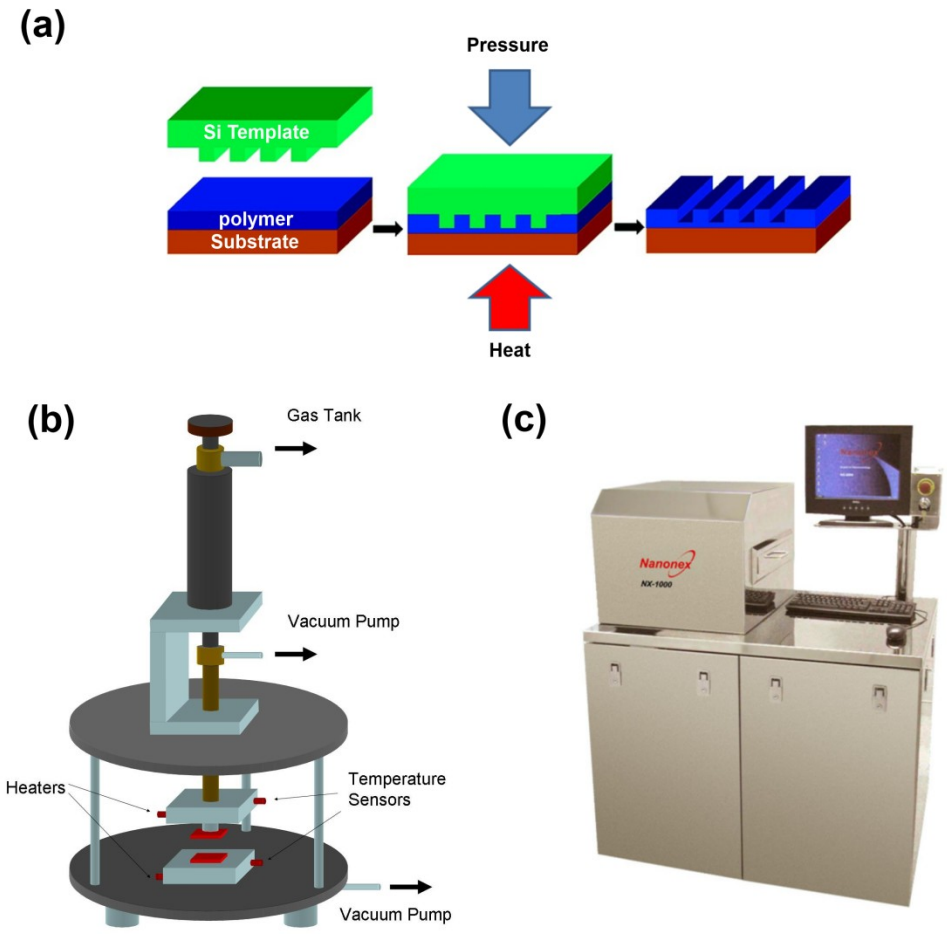


***Figure 5.2.*** *(a) Schematics of thermal nanoimprint process. (b) Home-built nanoimprint setup and (c) commercial Nanonex nanoimprinter.*

### 5.2.2 Fabrication of the $SiO_2$ master templates

The template in the nanoimprint plays has similar role as the photomask in photolithography and defines the resolution of the imprinted patterns in polymer materials. Therefore, the fabrication of a high quality master template is critical for nanoimprint process. Various materials such as Si, $SiO_2$, SiC, silicon nitride, metals, sapphire, and diamond film have been employed in the fabrication of nanoimprint templates.[18] In our experiments, Si with its native oxide was selected as template material due to its durability and the compatibility with

traditional fabrication process. The fabrication of a Si master template typically involves three steps as shown in figure 5.3. (a). First, etch masks are patterned on the silicon wafer by various methods. Second, these patterns are transferred into a Si substrate by reactive ion etching (RIE). Finally, the etch masks are removed either by $O_2$ plasma or wet chemistry. In our experiments, two alternative methods were used for the creation of etch masks on the Si master template. The first method used high-resolution electron beam lithography (EBL) while the second method relied on self-assembly nature of the PS-*b*-PMMA block copolymer on the Si substrate.

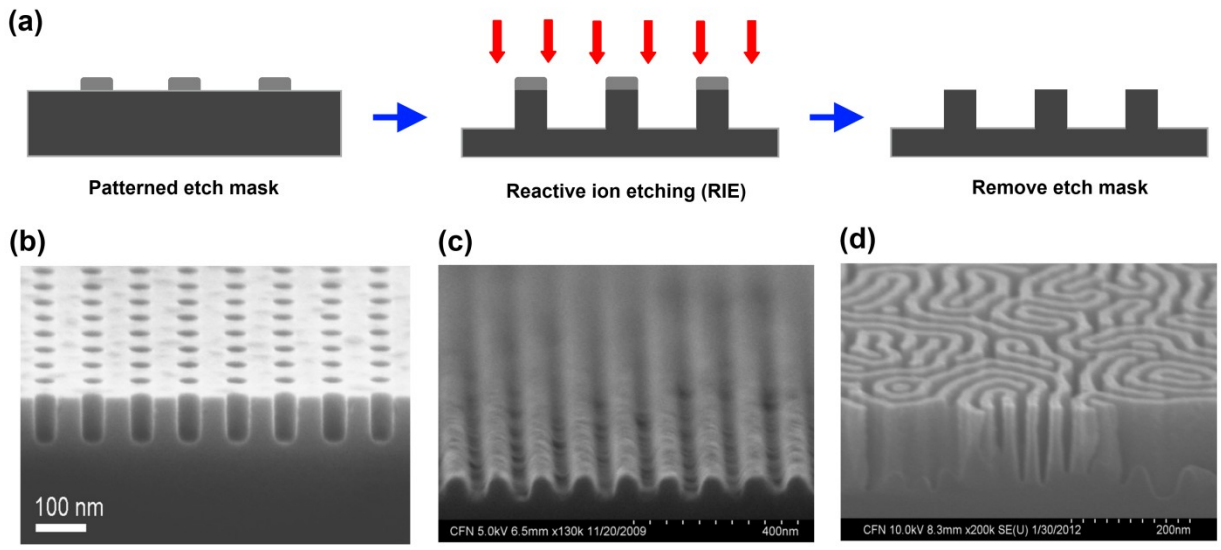


***Figure 5.3.*** *(a) Schematics illustration of the Si template fabrication process. SEM images of the templates fabricated with etch masks patterned by (b) E-beam lithography, (c) laser interference lithography, and (d) block copolymer self-assembly.*

For the EBL patterning we used a JEOL JBX6300-FS. The EBL system was operated at 100 kV with an electron probe current of 150 pA. Single pixel lines were exposed in a writing field of 500 x 500 $\mu m^2$ with 220 $mC/cm^2$ dose. A <100> orientation p-doped Si wafer (1–12 □-cm) was used as substrate. After cleaning the wafer in acetone and isopropanol, a film of

ZEP-520A resist (Zeon Corporation) was spin coated to a thickness of 50 nm for use as the resist and etch mask. Following the exposure with e-beam, the resist was developed in hexyl acetate (90 s), followed by isopropanol (90 s) and rinse in deionized water (90 s) providing the patterned etch mask for RIE process.

The block copolymer patterned etch masks were developed based on hardening parts of the PS-*b*-PMMA film through exposure to metal-organic precursors. This fabrication method, discovered by researchers at Argonne National Laboratory, significantly improved the mask etch resistance compared to pure polymer film.[19-21] In this process, exposure of the PS-*b*-PMMA thin film to a vapor pressure of trimethylaluminum (TMA) (10 Torr, 300 seconds) leads to selective incorporation of the metal-organic molecule into the PMMA block. The TMA is subsequently converted into aluminum oxide by a exposure to water vapor (~10 Torr, 300 seconds). For these experiments, we performed 3 TMA/water cycles in a commercial Cambridge NanoTech Savannah 100 atomic layer deposition tool. Following incorporation of aluminum oxide into the polymer film, we remove all organic material using an oxygen plasma (20 W RF power, 100mT $O_2$, March Plasma CS-1701 tool). The resulting aluminum oxide pattern is the inverse tone of a chemically developed PS-*b*-PMMA self-assembled pattern, with the PMMA block (converted to aluminum oxide) remaining as the etch mask.

Pattern transfer to the Si was performed by inductively-coupled RIE using an Oxford Instruments Plasmalab 100 where $SF_6$ was used as the etch gas. The temperature of the chamber was pre-cooled to −100˚C. The flow of $SF_6$, $O_2$ and the pressure in the chamber were kept constant at 40 sccm, 18 sccm and 12 mTorr, respectively. The plasma power and etch time were adjusted to achieve suitable pattern profiles and etch depths. The remaining etch mask film was removed using a March plasma etch tool ($O_2$, 100 mTorr, RF power 20 W for 1 min) while the

aluminum oxide etch mask was removed by dipping into aluminum etchant (Transene, Type A, 1 min, 50 °C).

Si master templates fabricated by laser interference lithography[22] were also employed in our experiments. This lithographic method utilizes the interference of two coherence laser beams that form an interference pattern on the substrate. Using photoresists similar to those used in optical lithography, this interference pattern can be transferred to the photoresist and subsequently to the Si substrate. This methods can produce patterns over large areas with periodic patterns where the pitch is determined by the wavelength of the lasers. The Si master templates fabricated by laser interference lithography were obtained from Prof. Tim Savas (MIT) and LightSmyth technologies. Typical SEM images of the Si template fabricated with etch masks patterned by e-beam lithography, laser interference lithography, and block copolymer self-assembly are shown in figure 5.3 (b), (c) and (d) respectively.

## 5.3 Imprinting on P3HT thin films

We imprinted (Nanonex NX-B200 instrument) 10×10 $mm^2$ areas of 100 nm thick P3HT films (Rieke Metals, $M_w \approx 50{,}000$ g·$mol^{-1}$, regioregularity ~ 95%, 2 wt. % in Chlorobenzene) spin-cast onto silicon substrates using a silicon master imprint template prepared using interference lithography.[22] The master template pattern consisted of a uniform 100 nm pitch grating with 50 nm deep trapezoidal-shaped grooves. To facilitate release of the master after imprinting, a 1-2 nm thick low-energy coating (perfluorodecyltrichlorosilane) was deposited on the template using a vapor deposition process.

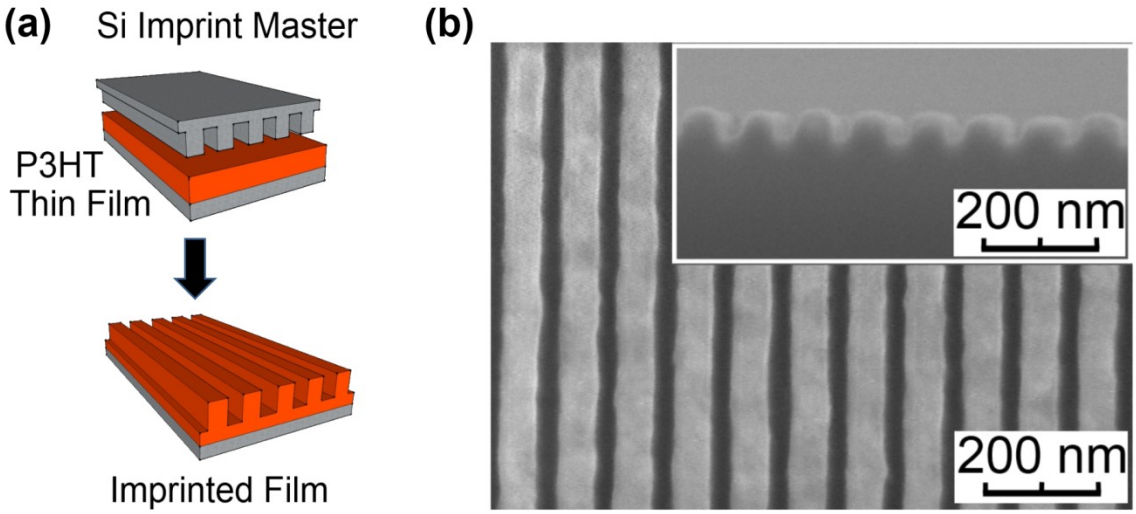


***Figure 5.4.*** *(a) the nanoimprint process. (b) SEM image of the imprinted P3HT gratings with a 100 nm period. (Inset: grating cross-sectional view.)*

The imprinting process involved applying a pressure of 3.4 MPa between the master and the coated polymer substrate stack at 150 °C for 5 minutes (schematic in Figure 5.4 (a)); the stack was then quenched to room temperature before releasing the applied pressure. Top-down and cross-sectional SEM images confirm a uniformly imprinted P3HT film (Figure 5.4 (b)).

GISAXS and GIWAXS measurements were performed at the X9 undulator-based beamline at the National Synchrotron Light Source, Brookhaven National Laboratory and the experimental geometry of the x-ray measurements is shown in figure 5.5. The incident X-ray beam ($\lambda$=0.0886 nm) was collimated using slits and focused onto the sample position using Kirkpatrick-Biez mirrors. This provides a 200 μm wide by 80 μm high spot at the sample position whose footprint along the sample spreads out by the inverse incident angle. The sample stage was located inside the vacuum chamber (Pressure ~ 40 Pa) where both the incident angle and azimuthal rotations are computer controlled. A two dimensional charged-coupled device (CCD) detector was positioned ~270 mm from the center of the sample stage to collect the GIWAXS images inside the same vacuum chamber. The GISAXS images were collected by a

second CCD detector located at a distance 3.5 m from the sample. A rectangular beam stop was positioned to block the primary and the reflected beams. Data conversion to $q$-space was accomplished by calibration using Silver Behenate powder.

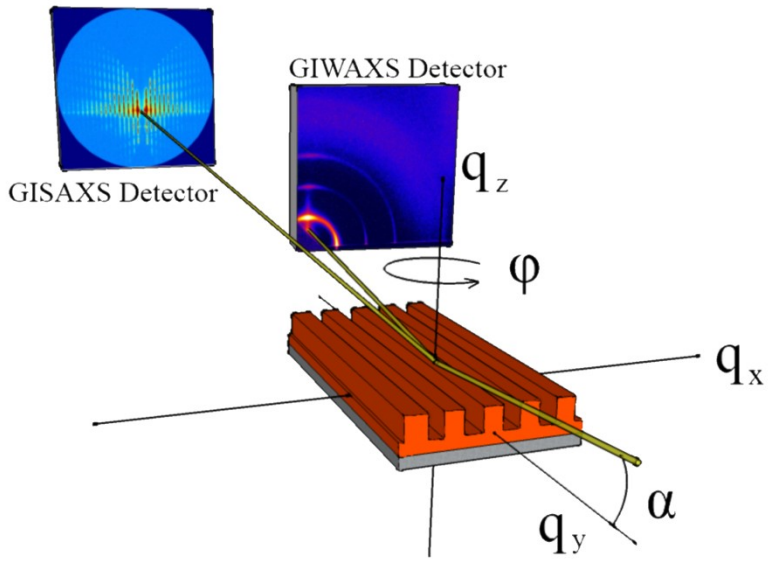


***Figure 5.5.*** *Geometry of GISAXS/GIWAXS measurements.*

We define the scattering vector, $\mathbf{q} = (q_x, q_y, q_z)$ with $q_y$ aligned along the groove direction, $q_x$ orthogonal to $q_y$ in the film plane, and $q_z$ pointing along the surface normal as described in Chapter 4. The relationship between each scattering vector component and the scattering angles ($\alpha_i$, $\alpha_f$ and $2\theta$) are described in Equation 3.5-3.7. Since a CCD image for a sample with a fixed azimuthal angle $\phi$ has both $q_x$ and $q_y$ components, it is convenient to define the surface radial component $q_r = \sqrt{(q_x^2 + q_y^2)}$ whose value is independent of $\phi$, the angle between the direction of the grooves and the incident x-rays. To acquire the GISAXS images, the sample was rotated at a constant speed over a limited $\phi$ range.[23] Note that the maximum $q_z$ increases with the $\phi$ range and that at the smallest $q_r$ the $q_z$ range is restricted (See figure 5.6 (a) and (b)).

For thermal annealing experiment, the scattering patterns were obtained every 30 °C and the effective heating rate was 10° C $min^{-1}$. At each temperature the sample was equilibrated for 10 minutes before collecting the x-ray scattering patterns.

### 5.3.1 Results and discussion

The imprinted film's nanostructure and its molecular chain configurations were investigated in-situ using GISAXS and GIWAXS. From the GISAXS pattern analysis we extracted the periodicity, height, sidewall angle, and the relative roughness of the top and bottom surfaces of the P3HT nanostructure. Detailed characterizations of the P3HT structure, including their molecular orientations within the nanostructure, were obtained from the GIWAXS measurements. In order to obtain insight into the thermal stability of the nano-imprinted P3HT films, essential information for fabrication process, and to assess the impact of heating effects for organic photovoltaic applications, temperature dependent studies were also carried out on the nano-imprinted P3HT films.

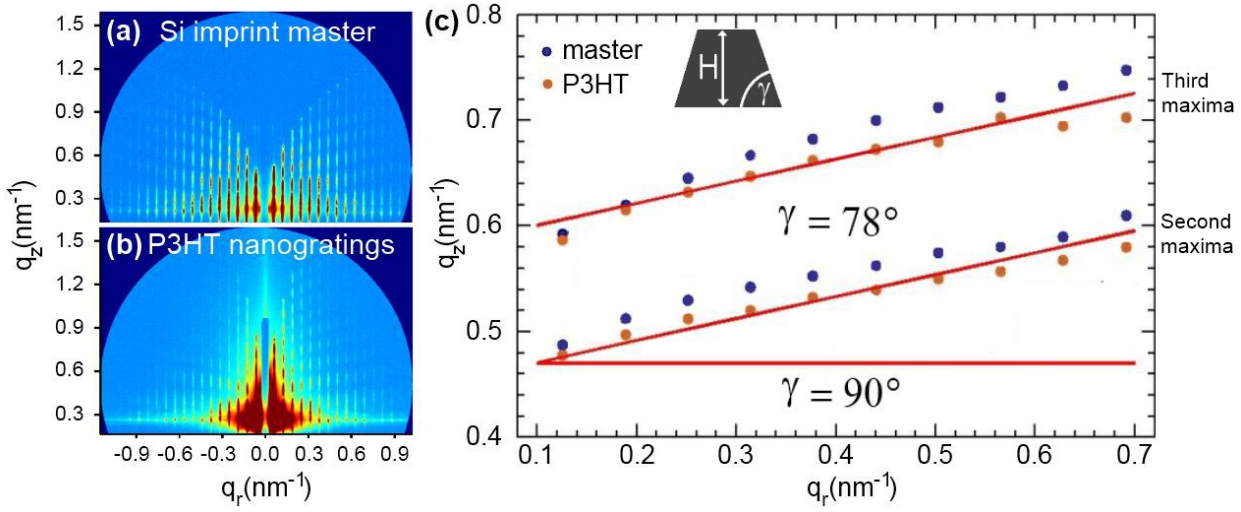


***Figure 5.6.*** *Two-dimensional GISAXS patterns of (a) silicon imprint master and (b) nano-imprinted P3HT. (c) Diffraction peak positions of the second and third BR maxima for the imprint master (blue circles) and P3HT nanogratings (red circles) in the $q_r$-$q_z$ plane. Solid lines represent the calculated peak positions with the corresponding side-wall angles. Inset: Schematic master trapezoidal cross- section.*

The GISAXS patterns from the silicon imprint master and imprinted P3HT film are sensitive to morphological features and exhibit a high degree of similarity (figures 5.6 (a) and (b)). Both patterns exhibit scattering features along $q_z$ at evenly-spaced values of $q_r$, known as Bragg rods (BRs). The BR's sinusoidal-like intensity modulation is characteristic of a relative scattering phase-factor equal to $H \times q_z$, where H is the height difference between the top and bottom of the pattern. According to Babinet's Principle,[25] diffraction from a pattern and its complement are equal apart from an intensity scale factor, and thus the similar scattering images from the master and the imprinted P3HT provide a measure of the high fidelity of the imprinting process, even in the absence of detailed analysis. However, refractive effects at small $q_z$ are different for the imprint master (silicon) and the imprinted material (polymer) due to their different electron densities, resulting in differences in the two patterns at small $q_z$. In addition, the dynamic scattering effects give rise to a streak of enhanced scattering along $q_r$, shown in figure 5.6 (a) and (b) when the outgoing angle ($\alpha_f$) is equal to the critical angle for the materials.

Detailed quantitative morphological information can be obtained by analyzing the BRs. The position of the BRs along $q_r$ is related to the grating periodicity, while the BR intensity modulation along $q_z$ contains information about the pattern feature height (H). For both the silicon master and imprinted P3HT, the spacing between the two adjacent BRs is 0.063 $nm^{-1}$, corresponding to a 99.7 ± 0.4 nm grating periodicity and consistent with the lithographically defined distance of 100 nm. The imprint master feature height of 54.6 ± 0.5 nm is obtained from the 0.115 $nm^{-1}$ modulation period along each BR. The imprinted polymer film has a feature height of 52.4 ± 0.5 nm, implying that nearly the entire depth of the master was imprinted into the P3HT film. The relative roughness of the top and bottom surfaces is primarily responsible for the damping of the intensity modulation along BRs; we can estimate a relative roughness less than 1.3 nm between top and bottom surfaces, based upon the $q_z$ distance over which the intensity falls by $1/e$ . This simple calculation does not include the form factor and inclusion of this factor only reduces the estimated roughness of 1.3 nm. The GISAXS measurements confirm an excellent fidelity of the imprinting process.

The sidewall slope angle can be directly measured from the BR phase shift modulation along $q_x$.[26] In figure 5.6 (c), the positions of the second and third maxima along the BRs are shown for both the master and the imprinted polymer film. Theoretically, for a sidewall angle ($\gamma$), the diffraction maxima of the same order (along the BR) will form a straight line with a slope of (90°- $\gamma$).[26] From the data shown in figure 5.6 (c), we approximate the sidewall angles for both the master and imprinted P3HT (open circles) of 78° ± 1° (solid line). These measurements are consistent with cross-sectional SEM images (Figure 5.4 (b)).

The packing structure including the lattice constants, coherence lengths, and orientations of the P3HT domains could be obtained from the GIWAXS patterns as described in previous

chapter. Before describing the GIWAXS patterns from the imprinted sample, the possible arrangement of the scattering peaks on the 2D detector with corresponding P3HT domains orientations were reviewed. The P3HT crystalline domains have three principle orientations with respect to the substrate, namely edge-on, face-on and vertical orientation, as shown in Figure 5.7. Since different crystallographic planes scatter X-rays in different directions, it is possible to determine the orientation of the P3HT crystalline domains from the position of the two distinct scattering peaks resulting from the lamellar stacking (100) and π-π stacking (010) on the 2D scatting patterns. In the illustrations of corresponding scattering patterns (Figure 5.7) for different domain orientations, the lamellar stacking (100) peak is represented by the circular spot closer to the origin while the π-π stacking (010) scattering peak is represented by the elongated spot further away from the origin reflecting the difference in lattice spacing. The polar angle (η) is defined as 0° for the $q_r$ axis and 90° for the $q_z$ axis.

First, we consider the three cases where one of the principle axis is along $q_z$ and the other two are randomly aligned within the plane. For edge-on oriented domain, the scattering pattern consist of the (100) peak along the $q_z$ direction and the (010) peak along the $q_r$ direction (see Figure 5.7 a). This configuration is commonly observed for as-cast P3HT thin films as discussed in Chapter 4. For face-on oriented domains, the (010) peak is located along the $q_z$ direction while the (100) peak is located along the $q_r$ direction (see Figure 5.7 b). For vertically oriented domains, both (100) and (010) peaks are aligned along the $q_r$ direction (see Figure 5.7 c). The scattering peak positions on the 2D detector with the corresponding domain orientations are summarized in the table in the Figure 5.7. Since only isotropic in-plane orientation is considered in this example, the sample rotation with respect to the incident X-ray does not affect the scattering patterns.

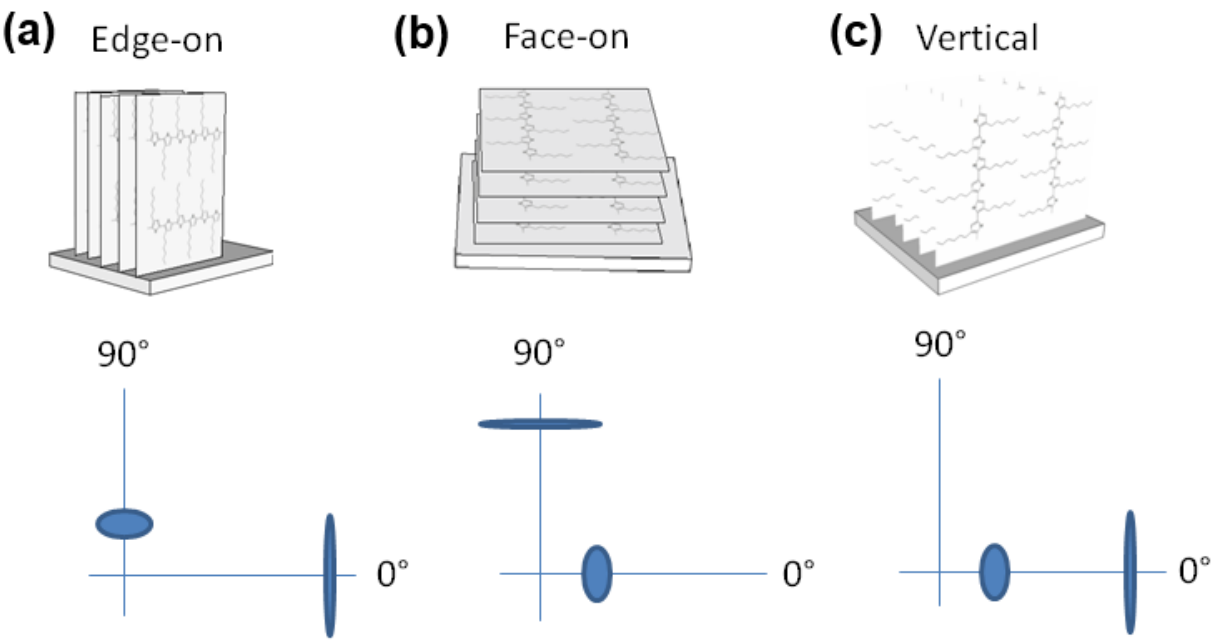


Polar angle of the scattering peak on 2D detector

| | Edge-on | Face-on | Vertical |
|---|---|---|---|
| (100) | 90 | 0 | 0 |
| (010) | 0 | 90 | 0 |

***Figure 5.7.*** *Illustration of example diffraction patterns from P3HT domains with different orientations. a) Edge-on domains with isotropic in-plane orientation, (b) face-on domain with isotropic in-plane orientation, and (c) vertically oriented domains with isotropic in-plane orientation.*

In the following, we will also consider in-plane orientation as well as the surface normal orientation. In this case, the in-plane scattering peaks only appears when the incident X-rays satisfy the Bragg conditions of the corresponding P3HT crystallites. It is convenient to define the principle axis as <1>, <2>, and <3>, as defined in Figure 5.8 (a). As shown in Figure 5.8 (b), the incident X-rays direction is defined to be along <3>. The lattice along <2> will lead to scattering peak along $q_z$ direction and the lattice along <1> will lead to a scattering peak along $q_r$ direction. Note that the small rotation required to satisfy the Bragg conditions is not considered. We

enumerate all other possibilities which will help identify the orientation of the P3HT domains from the observed scattering patterns.

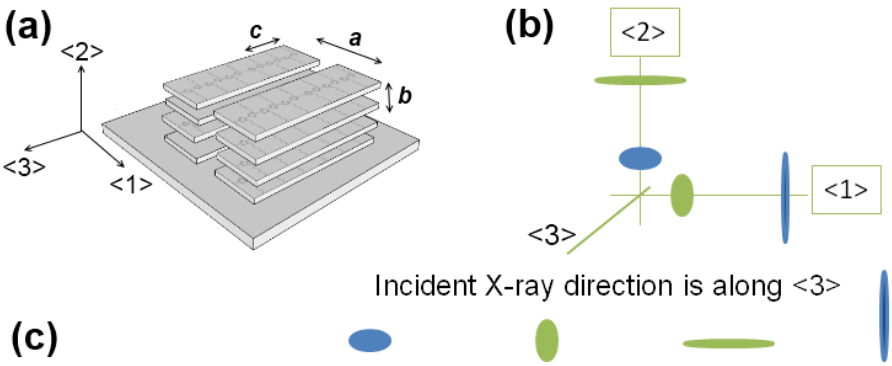


(c)

| | <1> | <2> | (100) along $q_z$ | (100) along $q_r$ | (010) along $q_z$ | (010) along $q_r$ |
|---|---|---|---|---|---|---|
| Face-on | a | b | | X | X | |
| Vertical | a | c | | X | | |
| Vertical | b | c | | | | X |
| Edge-on | b | a | X | | | X |
| Edge-on | c | a | X | | | |
| Face-on | c | b | | | X | |

***Figure 5.8.*** *(a) P3HT crystallite with corresponding lattice constant a, b and c. (b) Illustration of possible diffraction spots from P3HT crystallite with incident X-ray along the <3> direction. The $q_z$ direction is defines as direction <2> and $q_r$ direction as <1> to identify various P3HT crystallite orientations. (c) Table of all observable diffraction spots from P3HT crystallite with edge-on, face-on and vertical orientations.*

As discussed in Chapter 4 and illustrated again in Figure 5.8 (a), the lattice constant *a* of the P3HT crystallite is the lamellar stacking direction; lattice constant *b* is the π-π stacking direction and lattice constant *c* is the repeat distance along the backbone. Diffraction along the backbone is not observed. For instance, when (100) is oriented along <1> direction and (010) is along <2> direction, the (100) scattering peak will be observed along $q_r$ direction and the (010) scattering peak will be observed along $q_z$ direction. This corresponds to one of the two face-on

orientation and its configuration is listed in the first row of the table (see Figure 5.8 (c)). Similarly, the other five orientations are listed in the Figure 5.8 (c).

It is also possible that two or more different orientations coexist in the film. In such scenarios, the scattering peaks from the domains with two different orientations will overlap. Consider a situation where vertically oriented domains coexist with edge-on oriented domains. The resulting scattering peaks from each individual orientations are shown with red (x) in Figure 5.8 (c). Notice here that both orientations produce (010) scattering peak along $q_r$ direction. Therefore, the observation of (100) and (010) scattering peaks alone is not enough to identify the presence of vertically oriented P3HT domains. However, the presence of vertical orientation can be inferred by comparing the ratio of the intensity between the (100) and the (010) peaks. Since the scattering intensity of the overlapping peak is the linear combination of the intensity of the individual scattering peaks, the ratio of the (100) peak and the (010) peak from the mixed orienation is different from that of single orientation. Therefore, by comparing the ratio of integrated intensity of the (100) and the (010) peaks, additional orientation presented in the film can be identified. As we will show below, the ratio of the integrated intensity of the (100) and the (010) peaks is nearly constant for the nanoimprinted P3HT grating at $\phi = 0°$ and $\phi = 90°$ indicating that there is no vertical orientation with preferred in-plane alignment.

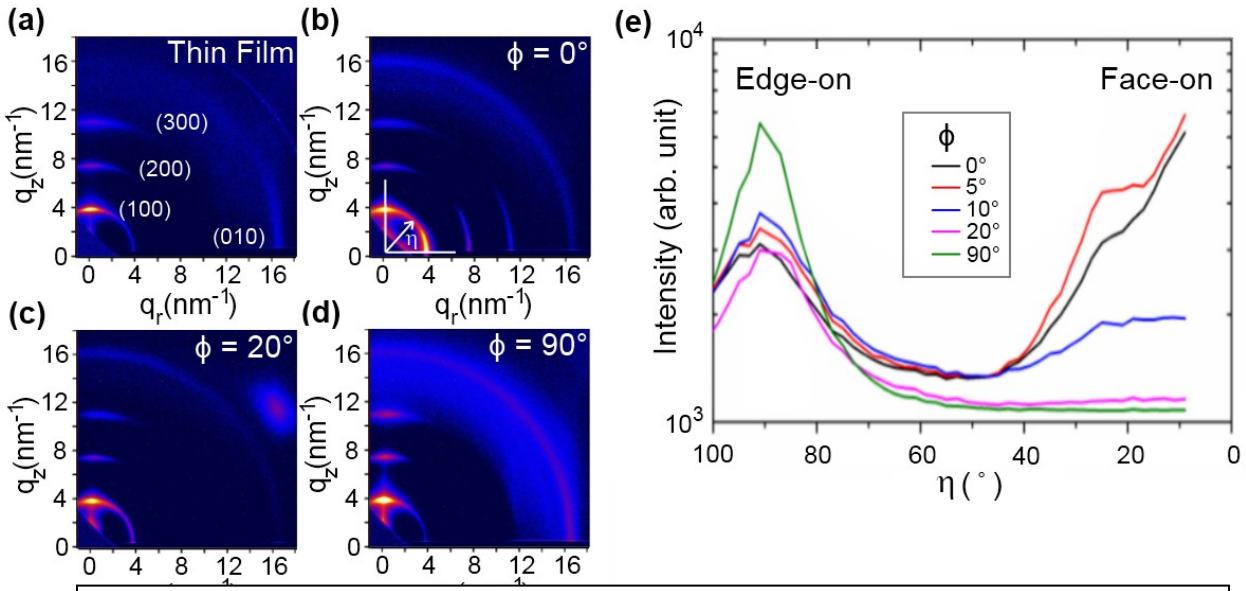


***Figure 5.9.*** *2D GIWAXS patterns of (a) uniform P3HT thin film and (b-d) imprinted P3HT taken with azimuthal angle (b) ϕ = 0°, (c) ϕ = 20° and (d) ϕ = 90°. The azimuthal angle (ϕ) is defined as zero when the grating is parallel to the direction of incident x-rays. (e) Polar angle (η) scans along the (100) peak positions for various ϕ.*

The GIWAXS pattern of a nanoimprinted P3HT film differs significantly from that of the control film. Although we observe scattering peaks at the same radial positions, they no longer exhibit a simple edge-on conformation. Further, the scattering pattern depends on the azimuthal alignment of the imprinted grating pattern with respect to the direction of the incident x-rays. In figures 5.9 (b-d), GIWAXS scattering patterns are shown for ϕ values ranging from 0 to 90˚. At ϕ = 0° (figure 5.9 (b)) we observe (100), (200), and (300) lamellar scattering peaks along both the $q_z$ and $q_r$ directions, indicating that the imprinting process has realigned some of the lamella parallel to the surface. For the ϕ = 90° imprinted film the (010) reflection exhibits intensity along the $q_z$ axis that is not observed for the control film. Together, these results indicate both edge-on and face-on orientations for the imprinted film. While all polymer domains with edge-on orientations contribute to the (100) peak along $q_z$, only face-on domains with their backbones aligned with the imprinted grooves satisfy the Bragg condition for the (100) peak along $q_r$. The

absence of the (100) peak along $q_r$ for $\phi > 20°$ (shown in figures 5.9 (c, d)) demonstrates that the backbones associated with the face-on domains are preferentially-aligned along the imprinted grooves. The (010) peak along the $q_z$ direction, arising from π-stacking of the face-on domains, satisfies the Bragg condition regardless of in-plane sample rotation and hence remains visible at all $\phi$. The 1D polar scans obtained at (100) peak position from the scattering patterns with different $\phi$ (figure 5.9 (e)) confirm the narrow in-plane orientation distribution of the P3HT backbones with respect to the imprinted grating pattern. In the polar scans, the peak at $\eta = 90°$ and 0° corresponds to the edge-on and face-on oriented P3HT domains, respectively. The intensity of the $\eta = 0°$ peak decreases rapidly with increasing $\phi$, and completely disappears at $\phi = 20°$, indicating that the backbones of the face-on domains are well-aligned along the grating grooves within an angular range of ~ 20° Full-Width-Half-Maximum (FWHM). However, the presence of the (010) peak along $q_r$ for all $\phi$ suggests that the backbones of the edge-on domains are still randomly-oriented in the plane of substrate. *Moreover, the ratio of the integrated intensity between the (010) peak along $q_r$ and (100) peak along $q_z$ remains the same for both $\phi = 0°$ and $\phi = 90°$ indicating that there is no in-plane oriented vertical orientation with preferred in-plane alignment as discussed in previous paragraph.* This is in contrast to a previously published study where the observation of vertically oriented P3HT domains with π-stacking direction aligned along the grating was reported.[27] However, it is possible that vertically oriented P3HT domains *with isotropic in-plane orientation* coexist with both face-on and edge-on domains in the imprinted film. The vertically oriented P3HT domains with isotropic in-plane orientation will contribute equally to the intensity of (010) peak at all $\phi$ values and hence the ratio of the integrated intensity between the (010) peak along $q_r$ and (100) peak along $q_z$ will remain constant for both $\phi = 0°$ *and* $\phi = 90°$. Moreover, in previous study,[27] the existence of

face-on oriented P3HT domains in nanoimprinted film was ruled out based on the absence of the (010) reflection along the $q_z$ (out-of-plane) direction.[27] Since this reflection is clearly observed in our study, their "missing reflection" might result from the following: (1) the much higher background scattering, (2) poor counting statistics and (3) the much weaker x-ray source (conventional source compared to the synchrotron based source used in the present study).

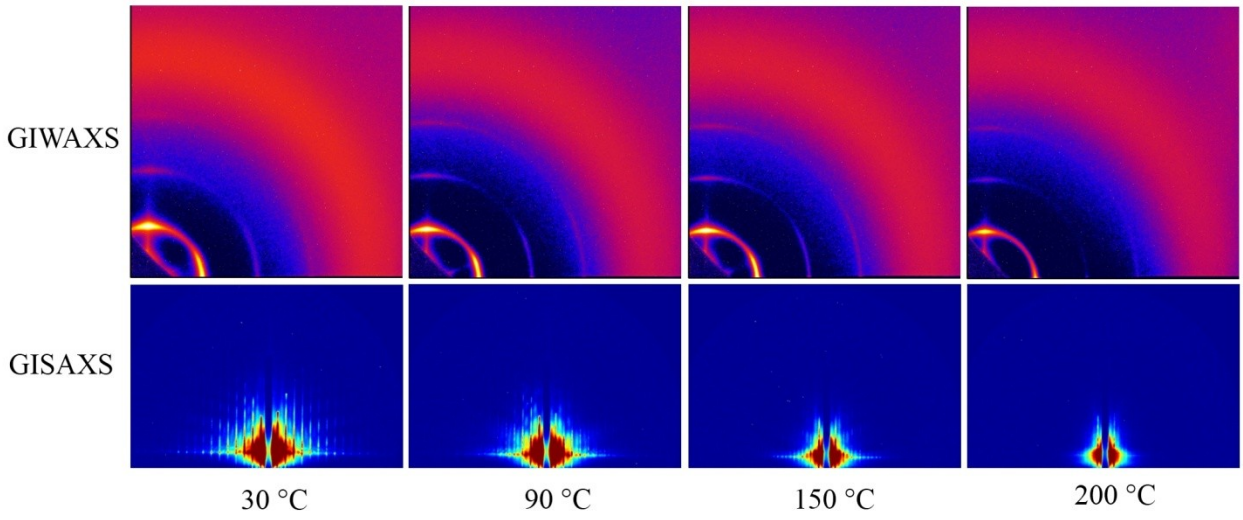


***Figure 5.10.*** *GIWAXS (top) and GISAXS (bottom) patterns of P3HT nano-grating at selected temperature during in-situ thermal annealing.*

In-situ GISAXS measurements of imprinted P3HT films at increasing temperatures show a rapid decay of higher-order BRs, indicating a smoothing-out of the imprinted pattern features (see figure 5.10). However, the first-order BR peak remains at temperatures as high as 200 °C, showing that remnants of the imprinted profile exist even at this elevated temperatures. The extinction of higher order BRs indicates a transformation from a trapezoidal imprinted profile to a sinusoidal-like height profile, consistent with previous studies of imprinted polystyrene films using critical dimension small-angle x-ray scattering, specular x-ray reflectivity, and optical measurements.[28-31]

Although the imprinted P3HT morphology largely disappears at elevated temperatures, the imprint-induced molecular orientation remains present. The GIWAXS pattern of an imprinted P3HT film at 200 °C at $\phi = 0$ shows evidence of face-on oriented P3HT domains (figure 5.10). The 1D scattering profiles along the $q_z$ and $q_r$ radial directions were extracted from 2D scattering images in the vicinity of the (100) peak, and fitted to a Gaussian line shape. In the fitting analysis, we have included the effects of refraction, beam divergence, beam bandwidth, and geometric smearing.[32] The fit-determined temperature-dependent lattice constant (see figure 5.11 (a)) and coherence length (see figure 5.11 (b)) are similar for both the edge-on and face-on orientations whereas the angular scattering width differs significantly for the two orientations. With increasing temperature the lattice constants for both domain orientations increases monotonically from 1.65 nm at 30 ºC to 1.80 nm at 200 ºC. Within our resolution, after accounting for refraction effects, there is no significant difference between the lattice constants for the face-on and edge-on configurations. At 30 ºC the coherence lengths for edge-on and face-on oriented P3HT domains, 25 nm and 30 nm, were similar to those of P3HT control films heated to 150 ºC and about a factor of two larger than the same films at 30 ºC prior to annealing. During a second heating cycle of the imprinted film (the first heating cycle was carried out during the imprinting) the coherence length increased by about ~5 nm for the edge-on oriented domains and ~10 nm for the face-on oriented domains. This increase may be due to the relaxation of temperature dependent strain effects after removing the master.

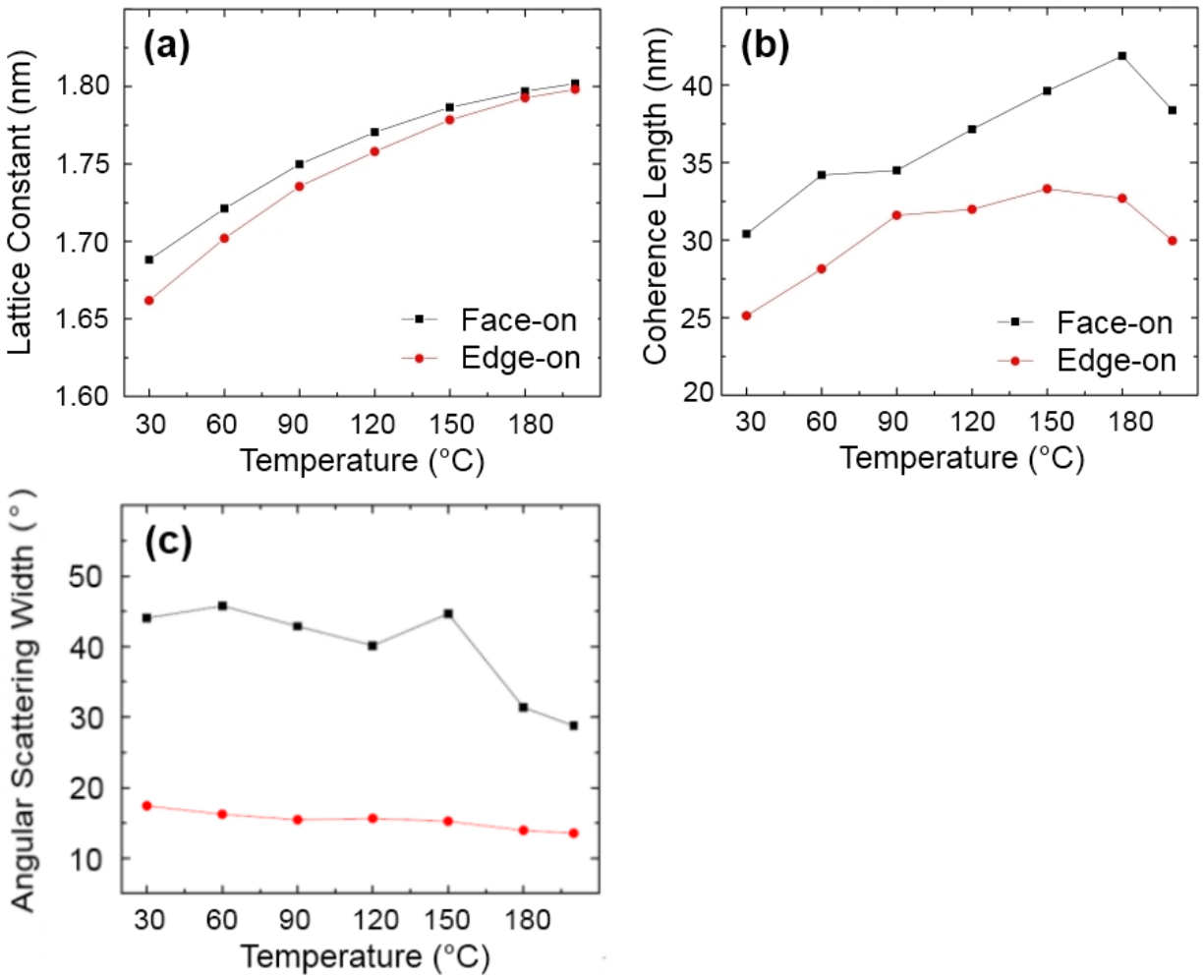


***Figure 5.11.*** *The (a) lattice constant, (b) coherent length, and (c) angular scattering width of the edge-on and face-on oriented P3HT crystallites calculated from the corresponding (100) peak as a function of temperature during in-situ thermal annealing.*

The bimodal distribution of the scattering profiles for the <100> peak at $\phi = 0$ provides information on the polar angular widths of the edge-on and face-on orientations. To obtain the profile widths, $\Delta\eta$, we have fit the data in two regions, $70° < \eta < 110°$ for the edge-on orientation and $8° < \eta < 45°$ for the face-on orientation to Gaussian profiles. The data for $\eta < 8°$ was not used due to the strong refraction affects and the peak position was fixed to $\eta = 0°$ due to the symmetry. At 30 °C for the face-on orientation, $\Delta\eta = 44°$ FWHM (calculated from the Gaussian widths)

which is more than twice the 17° FWHM of the edge-on orientation. For comparison, the edge-on domains of the control film exhibit a 13° FWHM. This relatively narrower angular spread of the edge-on domains results from crystal nucleation which occurs at the flat silicon substrate.[14] Similarly, the rough and titled sidewalls of the imprint master may contribute to the broader angular spread observed for the face-on domains. Upon annealing of the imprinted film - in the absence of the master - $\Delta\eta$ decreases (see figure 5.11 (c)) with increasing temperature suggesting that the vapor interface has a strong effect on the P3HT orientation.

## 5.4 Conclusions

This study provides insight into the structure and morphology of flat and imprinted P3HT thin films. The edge-on configuration observed on flat substrates is likely the lowest energy configuration since it maximizes the coverage of the low-energy methyl groups at both interfaces. This same driving force is believed to be the origin of surface freezing in chain molecules.[33] For the imprinted film, with its considerable sidewall area, the observed ~90º reorientation is likely driven by the reduction of the sidewall interfacial energy, which induces the ⟨100⟩ direction to be along the local surface normal. However, we cannot rule out other factors such as flow-induced reorientation,[10] which may also contribute. Despite the smoothing out of the topographical profile with increasing temperature, the molecular orientation does not simply restore to the edge-on configuration; rather both orientations remain. Evidently, annealing (to 200ºC) does not randomize the molecular orientation, but instead relaxes imprint-induced strain while simultaneously allowing the imprint-induced orientations to grow and become better defined. This suggests that a wide range of methods that induce mild orientational bias may be

amenable to directing P3HT assembly, when coupled with suitable annealing. Finally, the imprint process partially aligns the P3HT chain backbones along the imprinted groove direction. Combined, these results demonstrate that nanoimprint is a powerful tool for controlling molecular orientation in semiconducting polymer materials. The ability to simultaneously control nanometer-scale order and topography, while selecting the desired molecular orientation, should provide new opportunities for an improved understanding of the structure-properties relationship in organic devices since their anisotropic structural and electronic properties are difficult to ascertain in conventional, poorly oriented samples.

## 5.5 References


1. Mele, E.; Di Benedetto, F.; Persano, L.; Cingolani, R.; Pisignano, D., Multilevel, room-temperature nanoimprint lithography for conjugated polymer-based photonics. *Nano Lett* **2005,** 5, (10), 1915-1919.

2. Li, H. W.; Huck, W. T. S., Ordered block-copolymer assembly using nanoimprint lithography. *Nano Letters* **2004,** 4, (9), 1633-1636.

3. Hu, Z. J.; Baralia, G.; Bayot, V.; Gohy, J. F.; Jonas, A. M., Nanoscale control of polymer crystallization by nanoimprint lithography. *Nano Lett* **2005,** 5, (9), 1738-1743.

4. He, X., Gao, F., Tu, G., Hasko, D. G., Hüttner, S., Greenham, N. C., Steiner, U., Friend, R. H. and Huck, W. T. S., Formation of Well-Ordered Heterojunctions in Polymer:PCBM Photovoltaic Devices. *Adv Funct Mater* **2011,** 21, (1), 139-146.

5. He, X. M.; Gao, F.; Tu, G. L.; Hasko, D.; Huttner, S.; Steiner, U.; Greenham, N. C.; Friend, R. H.; Huck, W. T. S., Formation of Nanopatterned Polymer Blends in Photovoltaic Devices. *Nano Lett* **2010,** 10, (4), 1302-1307.

6. Austin, M. D.; Ge, H. X.; Wu, W.; Li, M. T.; Yu, Z. N.; Wasserman, D.; Lyon, S. A.; Chou, S. Y., Fabrication of 5 nm linewidth and 14 nm pitch features by nanoimprint lithography. *Appl Phys Lett* **2004,** 84, (26), 5299-5301.

7. Jung, G. Y.; Johnston-Halperin, E.; Wu, W.; Yu, Z. N.; Wang, S. Y.; Tong, W. M.; Li, Z. Y.; Green, J. E.; Sheriff, B. A.; Boukai, A.; Bunimovich, Y.; Heath, J. R.; Williams, R. S., Circuit fabrication at 17 nm half-pitch by nanoimprint lithography. *Nano Lett* **2006,** 6, (3), 351-354.

8. Chou, S. Y.; Krauss, P. R.; Renstrom, P. J., Imprint lithography with 25-nanometer resolution. *Science* **1996,** 272, (5258), 85-87.

9. Zheng, Z. J.; Yim, K. H.; Saifullah, M. S. M.; Welland, M. E.; Friend, R. H.; Kim, J. S.; Huck, W. T. S., Uniaxial alignment of liquid-crystalline conjugated polymers by nanoconfinement. *Nano Lett* **2007,** 7, (4), 987-992.

10. Hu, Z. J.; Muls, B.; Gence, L.; Serban, D. A.; Hofkens, J.; Melinte, S.; Nysten, B.; Demoustier-Champagne, S.; Jonas, A. M., High-throughput fabrication of organic nanowire devices with preferential internal alignment and improved performance. *Nano Lett* **2007,** 7, (12), 3639-3644.

11. DeLongchamp, D. M.; Vogel, B. M.; Jung, Y.; Gurau, M. C.; Richter, C. A.; Kirillov, O. A.; Obrzut, J.; Fischer, D. A.; Sambasivan, S.; Richter, L. J.; Lin, E. K., Variations in semiconducting polymer microstructure and hole mobility with spin-coating speed. *Chem Mater* **2005,** 17, (23), 5610-5612.

12. Yang, H. H.; LeFevre, S. W.; Ryu, C. Y.; Bao, Z. N., Solubility-driven thin film structures of regioregular poly(3-hexyl thiophene) using volatile solvents. *Appl Phys Lett* **2007,** 90, (17), -.

13. Sirringhaus, H.; Wilson, R. J.; Friend, R. H.; Inbasekaran, M.; Wu, W.; Woo, E. P.; Grell, M.; Bradley, D. D. C., Mobility enhancement in conjugated polymer field-effect transistors through chain alignment in a liquid-crystalline phase. *Appl Phys Lett* **2000,** 77, (3), 406-408.

14. Kline, R. J.; Mcgehee, M. D.; Toney, M. F., Highly oriented crystals at the buried interface in polythiophene thin-film transistors. *Nat Mater* **2006,** 5, (3), 222-228.

15. Yang, H. C.; Shin, T. J.; Yang, L.; Cho, K.; Ryu, C. Y.; Bao, Z. N., Effect of mesoscale crystalline structure on the field-effect mobility of regioregular poly(3-hexyl thiophene) in thin-film transistors. *Adv Funct Mater* **2005,** 15, (4), 671-676.

16. Chang, J. F.; Sun, B. Q.; Breiby, D. W.; Nielsen, M. M.; Solling, T. I.; Giles, M.; McCulloch, I.; Sirringhaus, H., Enhanced mobility of poly(3-hexylthiophene) transistors by spin-coating from high-boiling-point solvents. *Chem Mater* **2004,** 16, (23), 4772-4776.

17. Sirringhaus, H.; Brown, P. J.; Friend, R. H.; Nielsen, M. M.; Bechgaard, K.; Langeveld-Voss, B. M. W.; Spiering, A. J. H.; Janssen, R. A. J.; Meijer, E. W.; Herwig, P.; de Leeuw, D. M., Two-dimensional charge transport in self-organized, high-mobility conjugated polymers. *Nature* **1999,** 401, (6754), 685-688.

18. Guo, L. J., Nanoimprint lithography: Methods and material requirements. *Adv Mater* **2007,** 19, (4), 495-513.

19. Peng, Q.; Tseng, Y. C.; Darling, S. B.; Elam, J. W., Nanoscopic Patterned Materials with Tunable Dimensions via Atomic Layer Deposition on Block Copolymers. *Adv Mater* **2010,** 22, (45), 5129-+.

20. Peng, Q.; Tseng, Y. C.; Darling, S. B.; Elam, J. W., A Route to Nanoscopic Materials via Sequential Infiltration Synthesis on Block Copolymer Templates. *Acs Nano* **2011,** 5, (6), 4600-4606.

21. Tseng, Y. C.; Peng, Q.; Ocola, L. E.; Elam, J. W.; Darling, S. B., Enhanced Block Copolymer Lithography Using Sequential Infiltration Synthesis. *J Phys Chem C* **2011,** 115, (36), 17725-17729.

22. Savas, T. A.; Schattenburg, M. L.; Carter, J. M.; Smith, H. I., Large-area achromatic interferometric lithography for 100 nm period gratings and grids. *J Vac Sci Technol B* **1996,** 14, (6), 4167-4170.

23. Hofmann, T.; Dobisz, E.; Ocko, B. M., Grazing incident small angle x-ray scattering: A metrology to probe nanopatterned surfaces. *J Vac Sci Technol B* **2009,** 27, (6), 3238-3243.

24. Born, M.; Wolf, E., *Principles of optics; electromagnetic theory of propagation, interference, and diffraction of light*. Pergamon Press: London, New York, 1959, p 803.

25. Hu, T. J.; Jones, R. L.; Wu, W. L.; Lin, E. K.; Lin, Q. H.; Keane, D.; Weigand, S.; Quintana, J., Small angle x-ray scattering metrology for sidewall angle and cross section of nanometer scale line gratings. *J Appl Phys* **2004,** 96, (4), 1983-1987.

26. Aryal, M.; Trivedi, K.; Hu, W. C., Nano-Confinement Induced Chain Alignment in Ordered P3HT Nanostructures Defined by Nanoimprint Lithography. *Acs Nano* **2009,** 3, (10), 3085-3090.

27. Jones, R. L.; Hu, T. J.; Soles, C. L.; Lin, E. K.; Reano, R. M.; Casa, D. M., Real-time shape evolution of nanoimprinted polymer structures during thermal annealing. *Nano Lett* **2006,** 6, (8), 1723-1728.

28. Lee, H. J.; Soles, C. L.; Ro, H. W.; Jones, R. L.; Lin, E. K.; Wu, W. L.; Hines, D. R., Nanoimprint pattern transfer quality from specular x-ray reflectivity. *Appl Phys Lett* **2005,** 87, (26), -.

29. Ding, Y. F.; Ro, H. W.; Germer, T. A.; Douglas, J. F.; Okerberg, B. C.; Karim, A.; Soles, C. L., Relaxation Behavior of polymer structures fabricated by nanoimprint lithography. *Acs Nano* **2007,** 1, (2), 84-92.

30. Patrick, H. J.; Germer, T. A.; Ding, Y. F.; Ro, H. W.; Richter, L. J.; Soles, C. L., Scatterometry for in situ measurement of pattern reflow in nanoimprinted polymers. *Appl Phys Lett* **2008,** 93, (23), -.

31. Smilgies, D. M., Scherrer grain-size analysis adapted to grazing-incidence scattering with area detectors. *J Appl Crystallogr* **2009,** 42, 1030-1034.

32. Ocko, B. M.; Wu, X. Z.; Sirota, E. B.; Sinha, S. K.; Gang, O.; Deutsch, M., Surface freezing in chain molecules: Normal alkanes. *Phys Rev E* **1997,** 55, (3), 3164-3182.

# CHAPTER 6

## Bulk Heterojunction Solar Cells with Planar PEDOT:PSS Layer

### 6.1 Introduction

In order to study the effect of nanostructured PEDOT:PSS layer on the device performance, control OPV devices with planar PEDOT:PSS layers were first investigated. It is well known that the efficiency of P3HT:PCBM based solar cells depends on the polymers properties (molecular weight, regioregularity, polydispersity), concentration ratio of donor and acceptor materials,[1, 2] casting solvent, [3, 4] the active layer thickness[2, 5, 6] and thermal annealing conditions.[7, 8] A PCE around 3% is commonly reported for P3HT:PCBM based solar cells in the literature.[7-9] In this chapter, experimental conditions were explored to obtain PCE values comparable to literature values.

### 6.2 Materials optimization

Regioregular poly(3-hexylthiophene) (RR-P3HT) and [6,6]-phenyl-$C_{61}$-butyric acid methyl ester (PCBM) are the most commonly used polymer and fullerene derivative combination in OPV devices and are commercially available. In order to determine the best material to use, we compared P3HT from three suppliers: Plextronics (Plexcore OS 2100), Rieke Metals (4002-EE) and American Dye Source (ADS306PT), respectively. According to the supplier, P3HT from Plextronics has a regioregularity > 99%, molecular weight between 45K and 65K, and polydispersity about 2.0; P3HT from Rieke has regioregularity > 95%, and Mn at about 26K;

P3HT from ADS has regioregularity >95%, Mn between 10K and 35K, and polydispersity about 2.0. PCBM with purity >99.95% from two suppliers, ADS and NanoC were also evaluated. All materials were used as received without further purification.

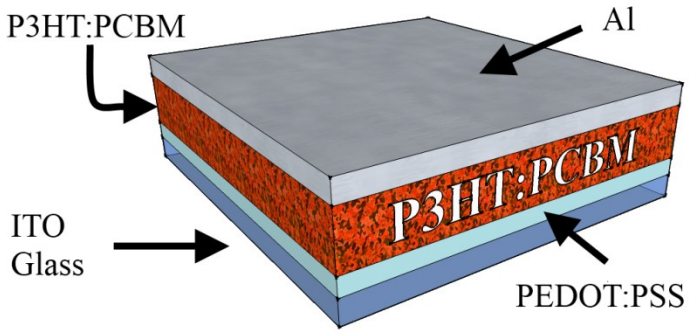


***Figure 6.1.*** *Schematic of the standard structure of reference OPV device.*

The standard structure of the reference bulk heterojunction OPV device is schematically shown in Figure 6.1. All the reference devices are fabricated according to the following procedure. First, ITO coated glass slides were cleaned with $O_2$ plasma for 5 min. In the second step, a PEDOT:PSS (Aldrich 655201) layer was then spin-coated (5000 rpm, 45s) on the cleaned ITO and baked for 10 min at 140°C on hot plate in air to remove the residual water. In the third step, P3HT and PCBM solutions (2 wt% in chlorobenzene) were stirred separately over 24 hours at 70 °C in a glove box. The two solutions were then mixed in a 1:1 weight ratio after filtering with PVDF filter (Whatman, 45 μm pore size) to obtain a blend solution. During the preparation of these solutions, extra care was taken to avoid long exposure to light. The spin coating speed, the solution concentration, and the choice of the solvent all affect the final thickness. Here the desired thickness was adjusted through the angular speed of the spin-coater. In the last step, an aluminum top electrode (~ 100 nm thick) was deposited via thermal evaporation (Lesker PVD)

under 5 × $10^{-7}$ torr with contact size defined by a shadow mask (500 μm to 2 mm diameter circles). The samples were annealed at 140°C for 10 min in a vacuum oven before characterization.

All devices were characterized with an illumination intensity of 100 mW/cm$^2$. The device curves, I-V plots, were recorded first in the dark and then under illumination using a Rucker-Kolls semiconductor analyzer. I-V curves are measured in three regions: the negative voltage region where the device is under reversed bias, through the power generation region ($0 < V < V_{oc}$), and $V > V_{oc}$. From the I-V curve, the open circuit voltage, the short circuit current, and the fill factor can be extracted. Provided that the intensity of the illuminated light is known, power conversion efficiency of the device can be calculated using equation 2.1 as described in Chapter 2.

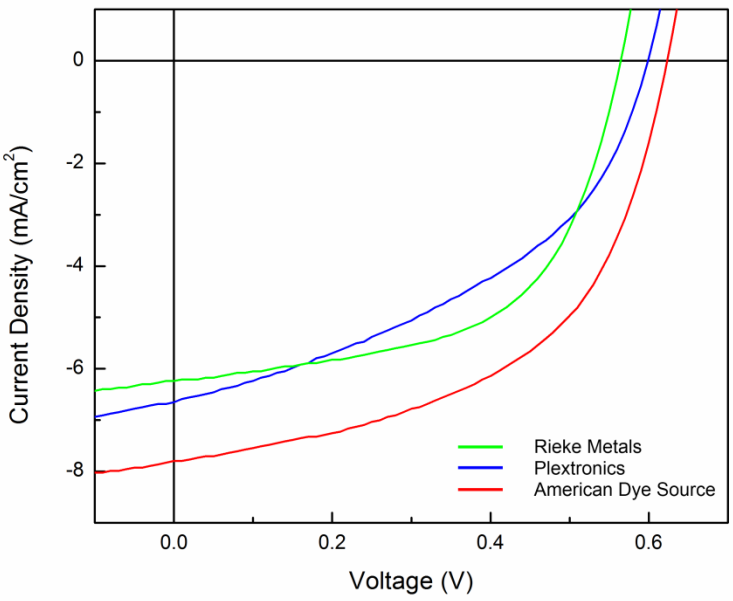


***Figure 6.2.*** *Typical I-V characteristics of devices made of P3HT materials from Rieke Metals, Plextronics and American Dye Source.*

The representative I-V characteristics obtained from the devices fabricated with P3HT from three different suppliers are plotted in Figure 6.2 and the corresponding parameters extracted from the I-V curves are compared in table 6.1.

***Table 6.1.*** *Summary of the parameters extracted from the devices with P3HT from different suppliers.*

| Suppliers | PCE (%) | $J_{sc}$ (mA/cm$^2$) | $V_{oc}$ (V) | FF (%) |
|---|---|---|---|---|
| Rieke | 1.6 | 6.3 | 0.54 | 48 |
| Plextronics | 1.7 | 6.7 | 0.59 | 43 |
| ADS | 2.3 | 7.8 | 0.63 | 47 |

Among those devices, the ADS P3HT device exhibits the highest $J_{sc}$ and $V_{oc}$ with reasonable FF, and hence the best overall PCE. It is important to note that $J_{sc}$ and FF can be further optimized by varying the thickness. Therefore, $V_{oc}$ is essential in determining the materials performance properties. Similar device performance was obtained for both NanoC and ADS PCBM. From the ADS P3HT and PCBM, less batch to batch variation (3 batches were used during the studies) in overall device performance were also observed. Based on these experiments, the ADS P3HT was chosen to fabricate the devices in the subsequent experiments.

## 6.3 Effect of device thickness

With the best available polymer (P3HT) and fullerene (PCBM) materials, $V_{oc}$ of the devices was consistently obtained at about 0.63 V. Here, the $J_{sc}$ and FF of the devices were further optimized by varying the thickness of the blend layer.

The correlation between the device thickness and $J_{sc}$ has been studied extensively[10, 11] and it has been shown that that the photon absorption in the active layer does not increase smoothly as a function of active layer thickness, but rather it is oscillatory because of the interference between forward and reflected light. The competition between exciton generation upon photoexcitation and carrier recombination during the charge transport process also influences the short circuit current ($J_{sc}$). Increasing the film thickness will improve the light absorption and hence generate more excitons. However, a thicker film also requires the dissociated carriers to travel a longer distance before they can be extracted, thus resulting in more carrier recombination. Therefore, the thickness of the active layer has to be optimized such that it is thick enough to absorb most of the incident light but thin enough to allow efficient charge collection.

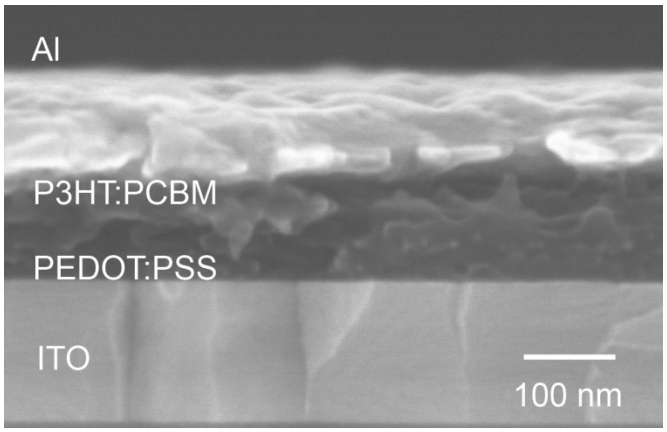


***Figure 6.3.*** *Cross-sectional SEM image of the reference OPV*

For these thickness dependent measurements, the P3HT/PCBM solution was prepared at a 1:1 mass ratio in chlorobenzene (2 wt%) using the ADS P3HT and PCBM. Samples were spin-coated at different spin speeds for 45 seconds to adjust the film thickness. The thickness of the devices was measured by profilometer (Dektak 150) and cross sectional SEM (Hitachi 4800) as shown in Figure 6.2.4. All devices were made under the same conditions except for spin speed.

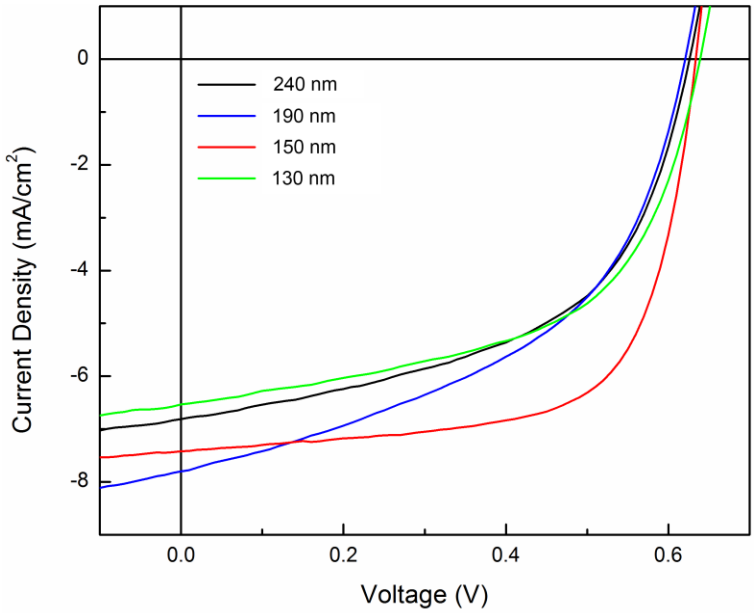


***Figure 6.4.*** *Selected I-V characteristics of the reference devices with different active layer thickness fabricated by spin-coating at different spin speeds.*

Figure 6.4 shows the I-V characteristics of the best devices fabricated at different spin speeds and the average parameters from five different devices with corresponding spin speeds are tabulated in table 6.2. The active layer thickness decreased with increasing spin speed according to Figure 6.5. The devices fabricated with 1300 rpm resulted in the thinnest film, ~130 nm and exhibited a $J_{sc}$ of 6.5 mA/cm$^2$. As the spin speed was decreased, the active layer thickness increased and initially this provided higher light absorption and hence higher $J_{sc}$. When the film thickness was increased beyond 180 nm, $J_{sc}$ started to decrease, and at a thickness of 240 nm it was down to ~ 6.5 mA/cm$^2$, indicating the competition between charge generation and

recombination. Although the highest $J_{sc}$ is obtained at 900 rpm, FF improves substantially for 1100 rpm devices resulting in the best PCE of ~3.0%.

| Spin Speed | PCE (%) | $J_{sc}$ (mA/cm$^2$) | $V_{oc}$ (V) | FF (%) |
|---|---|---|---|---|
| 700 rpm | 2.1 | 6.5 | 0.63 | 52 |
| 900 rpm | 2.3 | 7.5 | 0.62 | 49 |
| 1100 rpm | 3.0 | 7.1 | 0.64 | 67 |
| 1300 rpm | 2.3 | 6.5 | 0.63 | 57 |

**Table 6.2.** *Summary of the parameters extracted from the devices fabricated with different spin speeds.*

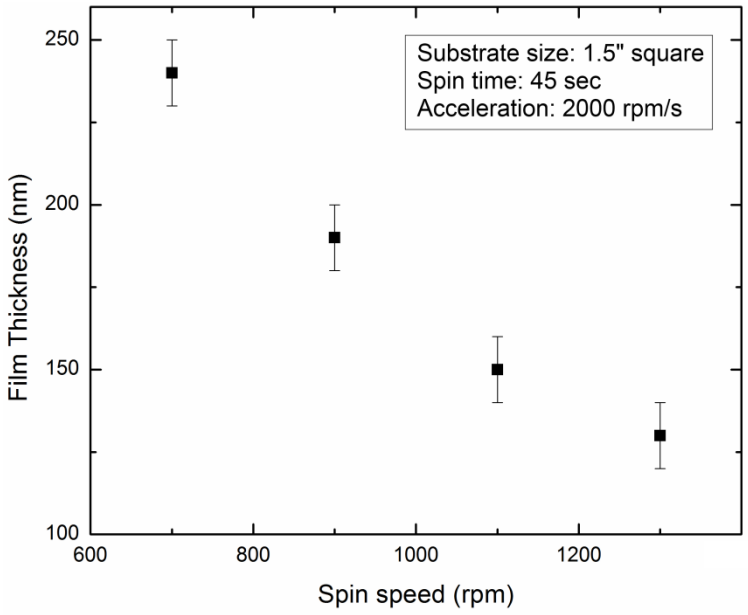


***Figure 6.5.*** *Spin curve of ADS P3HT:PCBM (1:1) blend taken on a Brewer Science Cee 200CB spin-coater in ambient condition. The insert describes the parameter settings.*

## 6.4 Conclusion

We concluded that the best active layer thickness for our devices is $140 \pm 10$ nm, obtained from a 1100 rpm spin speed. These devices exhibited $J_{sc}$ ~ 7.1 mA/cm$^2$, $V_{oc}$ ~ 0.64 V, FF ~ 67% and PCE ~ 3%, comparable to the values reported for P3HT:PCBM devices in the literatures.

## 6.5 References


1. van Duren, J. K. J.; Yang, X. N.; Loos, J.; Bulle-Lieuwma, C. W. T.; Sieval, A. B.; Hummelen, J. C.; Janssen, R. A. J., Relating the morphology of poly(p-phenylene vinylene)/methanofullerene blends to solar-cell performance. *Adv Funct Mater* **2004,** 14, (5), 425-434.

2. Moule, A. J.; Bonekamp, J. B.; Meerholz, K., The effect of active layer thickness and composition on the performance of bulk-heterojunction solar cells. *J Appl Phys* **2006,** 100, (9).

3. Shaheen, S. E.; Brabec, C. J.; Sariciftci, N. S.; Padinger, F.; Fromherz, T.; Hummelen, J. C., 2.5% efficient organic plastic solar cells. *Appl Phys Lett* **2001,** 78, (6), 841-843.

4. Rispens, M. T.; Meetsma, A.; Rittberger, R.; Brabec, C. J.; Sariciftci, N. S.; Hummelen, J. C., Influence of the solvent on the crystal structure of PCBM and the efficiency of MDMO-PPV : PCBM 'plastic' solar cells. *Chem Commun* **2003**, (17), 2116-2118.

5. Li, G.; Shrotriya, V.; Yao, Y.; Yang, Y., Investigation of annealing effects and film thickness dependence of polymer solar cells based on poly(3-hexylthiophene). *J Appl Phys* **2005,** 98, (4).

6. Lenes, M.; Koster, L. J. A.; Mihailetchi, V. D.; Blom, P. W. M., Thickness dependence of the efficiency of polymer : fullerene bulk heterojunction solar cells. *Appl Phys Lett* **2006,** 88, (24).

7. Ma, W. L.; Yang, C. Y.; Gong, X.; Lee, K.; Heeger, A. J., Thermally stable, efficient polymer solar cells with nanoscale control of the interpenetrating network morphology. *Adv Funct Mater* **2005,** 15, (10), 1617-1622.

8. Li, G.; Shrotriya, V.; Huang, J. S.; Yao, Y.; Moriarty, T.; Emery, K.; Yang, Y., High-efficiency solution processable polymer photovoltaic cells by self-organization of polymer blends. *Nat Mater* **2005,** 4, (11), 864-868.

9. Reyes-Reyes, M.; Kim, K.; Carroll, D. L., High-efficiency photovoltaic devices based on annealed poly(3-hexylthiophene) and 1-(3-methoxycarbonyl)-propyl-1-phenyl-(6,6)C-61 blends. *Appl Phys Lett* **2005,** 87, (8).

10. Hoppe, H.; Arnold, N.; Sariciftci, N. S.; Meissner, D., Modeling the optical absorption within conjugated polymer/fullerene-based bulk-heterojunction organic solar cells. *Sol Energ Mat Sol C* **2003,** 80, (1), 105-113.

11. Pettersson, L. A. A.; Roman, L. S.; Inganas, O., Modeling photocurrent action spectra of photovoltaic devices based on organic thin films. *J Appl Phys* **1999,** 86, (1), 487-496.

# CHAPTER 7

## Bulk Heterojunction Solar Cells with Nanoimprinted PEDOT:PSS Layer

### 7.1 Introduction

One of the most promising routes to increase the power conversion efficiency in organic photovoltaic (OPV) devices is to employ high surface area nanostructured electrodes.[1-4] Nanostructured electrodes not only provide larger surface area for charge extraction but might also improve other important aspects in charge carrier collection compared to planar electrodes. One of the limiting factors which affects the efficiency of OPV thin film devices is the competition between the absorption and charge collection.[5, 6] The active layer must be thick enough to absorb most of the incident photons but also thin enough to maintain the efficient charge collection. However, since the charge transport through organic materials is typically several orders of magnitude slower than with inorganic thin film,[7] they are prone to interfacial recombination along collection pathways which are associated with grain boundaries and impurities. Hence, the thickness of the active layer has been difficult to optimize even for the high absorbing low-bandgap polycarbazole-based polymer such as PCDTBT in which the active layer thickness is limited to < 80 nm before offseting the efficiency of charge collection.[8]

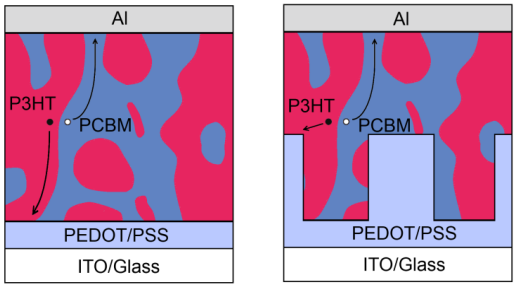


***Figure 7.1.*** *Schematic comparing charge collection in a BHJ solar cells with planar (left) and nanostructured (right) PEDOT:PSS layers.*

The incorporation of nanostructured electrodes into OPV devices is appealing since it provides a means of increasing the light absorption without compromising the charge carrier transport. Specifically, the effective thickness of the active blend layer can be increased while the distance of the nanostrucured electrodes can be optimized for an efficient charge extraction. There have been many attempts to implement nanostructured electrodes in various types of photovoltaic devices including polymer[1, 2, 4], dye-sensitized[9, 10] and hybrid organic-inorganic[11, 12] solar cells. Nanostructuring transparent electrodes itself such as indium tin oxide (ITO) into fibers[9], nanowires[10] and pillars[1, 2] requires complex fabrication procedures and under these conditions it is difficult to maintain highly conductive transparent films. In this chapter, results for bulk heterojunction solar cells which incorporated nanoimprinted PEDOT:PSS layer, are reported.

## 7.2. Fabrication and characterization of nanostructured PEDOT:PSS layer

PEDOT:PSS (Poly(3,4-ethylenedioxythiophene):poly(styrenesulfonate)) is a blend of an oxidatively doped, cationic, conducting polythiophene derivative (PEDOT) electrostatically bound to a PSS polyanion. The molecular structure of the species present in the PEDOT:PSS thin film is shown in Figure 7.2. Interfacial layers of PEDOT:PSS have been used in various organic electronic applications including sensors, organic field-effect transistors (OFETs), organic photovoltaics (OPVs) and organic light-emitting diodes (OLEDs) due to their superior optical, electrical, chemical and mechanical properties.[13-15]

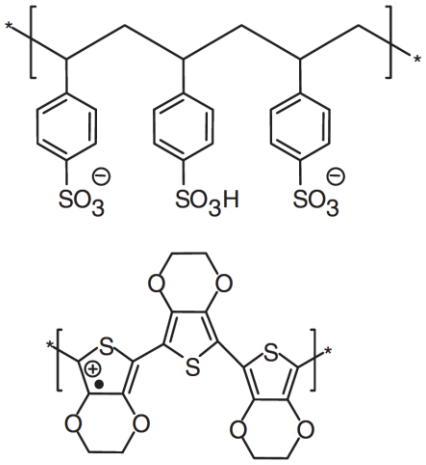


***Figure 7.2.*** *Molecular structure of PEDOT:PSS.*

Although it is highly desirable to pattern PEDOT:PSS layers in organic electronic devices, the fabrication of such patterns has been challenging due to its incompatibility with most standard lithographic methods. For instance, the acidic nature of PEDOT:PSS can damage acid-sensitive photoresists such as those used in conventional photolithography.[16, 17] The standard aqueous developers are also incompatible with the water-soluble PEDOT:PSS films. Since PEDOT:PSS lacks a distinct glass-transition temperature ($T_g$),[18] heating at elevated temperatures does not provide enough fluidity of the polymer chains for conventional thermal imprinting. Hence, dry thermal imprinting on PEDOT:PSS films at 150 °C with polydimethylsiloxane stamp resulted in shallow and non-uniform pattern transfer.[19] Organic vapors have been used to lower the viscosity of other polymer films during nanoimprinting,[18, 20, 21] but PEDOT:PSS is not soluble in most organic solvents hence its viscosity cannot be easily lowered by the introduction of organic solvents. On the other hand, water may be a suitable solvent for nanoimprinting of PEDOT:PSS films since PEDOT:PSS thin films swell up to 25% of their dry thicknesses due to the hygroscopic nature of the sulfonic acid groups.[22] Other techniques for patterning PEDOT:PSS such as self-assembled block copolymer lithography[23] and

laser ablation[24] either require elaborate fabrication processes or they are not efficient in producing large-area patterns. Therefore, water-vapor-assisted nanoimprinting were introduced to pattern PEDOT:PSS thin films in the following section.

### 7.2.1 Water-vapor assisted nanoimprinting

The schematic representation of the experimental water-vapor-assisted imprinting set-up is shown in Figure 7.3 (a) and the procedure is summarized in Figure 7.3 (b).

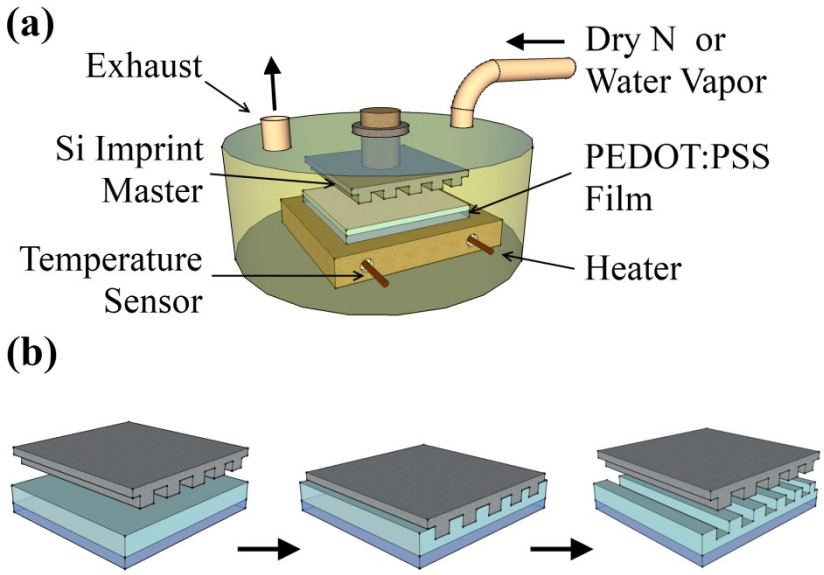


***Figure 7.3*** *(a) Schematic diagram of the experimental set-up. (b) Three-step process for water-vapor-assisted nanoimprinting.*

The sample chamber contained the PEDOT:PSS thin film mounted on the lower heating stage (made of copper to ensure good thermal conductivity). The silicon master template was attached to a second copper block with the patterned side facing downward above the

PEDOT:PSS thin film. The water-vapor was introduced into the chamber by flowing the nitrogen ($N_2$) stream through a water bubbler (room temperature) before entering the chamber. Vapor-assisted, room temperature imprinting did not provide successful pattern transfer suggesting that elevated temperatures are required to improve the film's viscoelastic properties. Vapor-assisted thermal imprinting of PEDOT:PSS films was carried out using an imprinting pressure of 3.4 MPa (applied for 10 minutes) at a range of temperatures between 25 and 100 °C and SEM images of the resulting imprinted PEDOT:PSS patterns are shown in Figure 7.4. The quality of pattern transfer improves with increasing temperature and the best results were obtained at 150 °C. The 150 °C maximum temperature has been chosen since this is the drying temperature typically used to remove excess water from PEDOT:PSS films used in organic electronic devices. [1,8]

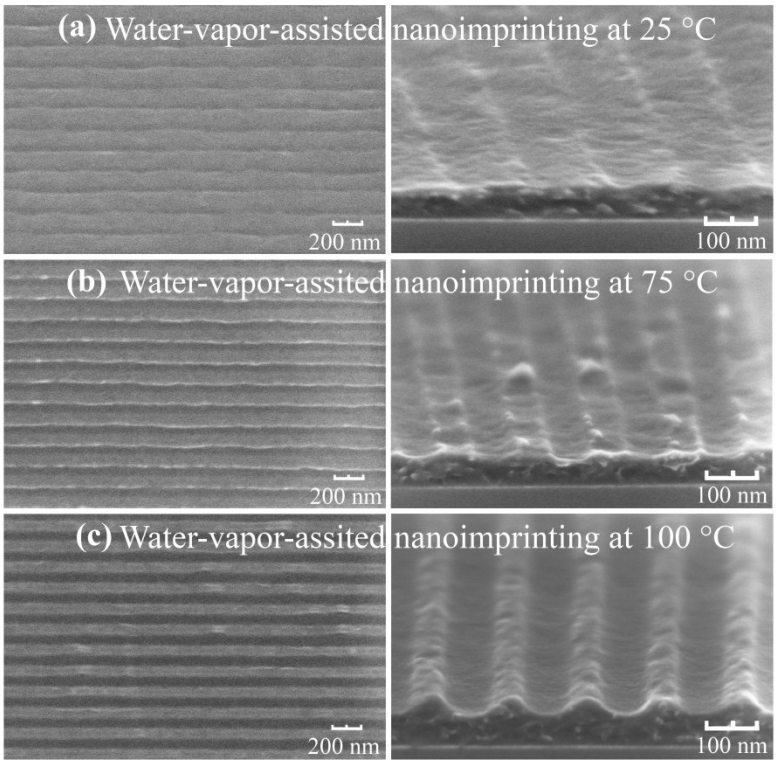


***Figure 7.4*** *SEM images of PEDOT:PSS layers patterned with water-vapor assisted nanoimprinting at a) 25 °C, b) 75 °C and c) 100 °C.*

Prior to imprinting, the room temperature, water-vapor saturated $N_2$ gas (~25 mm Hg) was introduced into the chamber for all imprinting temperatures. To allow the film to equilibrate at the desired temperature and humidity, all of the films were maintained at temperature for 10 minutes before imprinting. After imprinting, the chamber was flushed with dry $N_2$ gas for 5 minutes to remove residual water-vapor. The stamp was removed from the sample only after subsequent cooling to room temperature. The conventional thermal imprinting was also carried out using the same procedure above where a dry $N_2$ stream was used rather than the water-vapor stream. Structural characterization for dry-thermal and wet-thermal imprinting at 150 °C are presented in the following section.

### 7.2.2. Structural and Electrical characterization

The fidelity of the pattern transfer and the quality of the imprinted patterns between water-assisted thermal and dry thermal processes were compared using GISAXS and SEM, and the primary results are shown in Figure 7.5. GISAXS, a rapid and nondestructive technique, provides structural information in reciprocal space and averages over macroscopic regions while SEM is a real space local probe and provides complimentary information on the imprinting process. Figure 7.5 (left column) shows the GISAXS images from the (top) silicon imprint master, PEDOT:PSS patterns from (middle) thermal imprinting and (bottom) water-vapor-assisted imprinting. As discussed in Chapter 5, GISAXS images exhibit BRs at evenly-spaced values of $q_r$ and the in-plane spacing ($\Delta q_r$) of the BRs is simply related to the grating periodicity ($2\pi/\Delta q_r$). The BRs often exhibit a strong modulation which primarily results from the interference of x-rays scattered from both the top and bottom of the pattern and thus give precise information on the pattern's height. A quantitative morphological description of the nanoscale

patterns can be obtained from an analysis of the BRs. The sidewall slope angle can be directly measured from the phase shift of the BR modulations with $q_r$ as is evident from the "sloping wings" of the scattering pattern (see Figure 7.5).

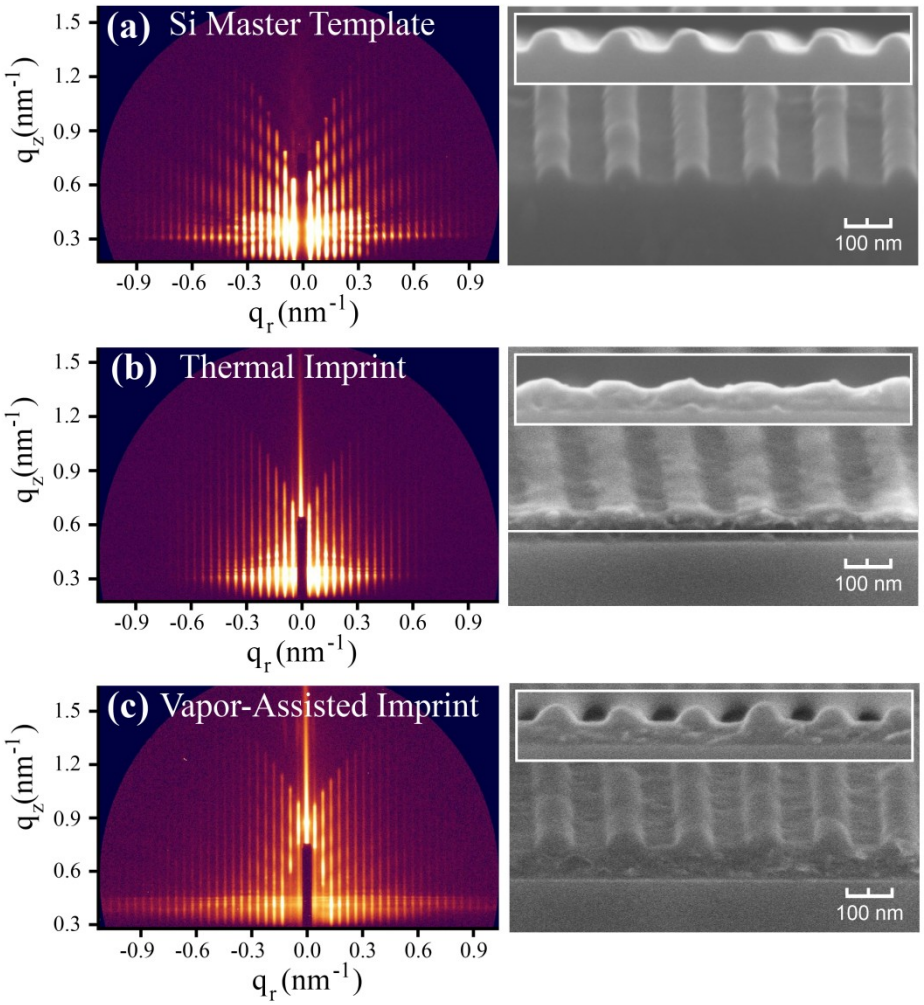


***Figure 7.5*** *GISAXS (right) and SEM (left) images of a) silicon master template, b) PEDOT:PSS gratings fabricated by thermal nanoimprinting and c) PEDOT:PSS gratings fabricated by vapor-assisted nanoimprinting. The insets show the cross-sectional view.*

For the silicon master template, $\Delta q_r = 0.0449$ nm$^{-1}$, corresponding to a 140 nm grating periodicity. A 40 nm feature height is obtained from the 0.156 nm$^{-1}$ modulation period along each BR. The sidewall angle of (46.7± 0.7)° is approximated from the shift in positions of the

maxima along the BRs.[18] These dimensions, also confirmed by the cross-sectional SEM images (Figure 7.5 a, right), are consistent with the lithographically defined periodicity and patterning height.

The GISAXS image of the dry thermally imprinted PEDOT:PSS pattern (Figure 7.5 b, right) exhibits BRs with $\Delta q_r = 0.0448$ nm$^{-1}$ the same as the master, as expected. However, the strong intensity modulations along each BR in the master have vanished for the dry imprinted sample. Representative BR profiles (Figure 7.6) show a very weak modulation whose period is larger than that of the master template, thus indicating incomplete imprinting. This implies poor pattern transfer since perfect transfer should give rise to the same overall behavior of the master and imprinted BRs. The much faster fall-off of the dry imprinted BR modulations suggests the absence of flat features at the tops and bottoms of the imprinted patterns. This is consistent with the cross-sectional SEM image (Figure 7.5 b, left), where the height of the dry thermally imprinted PEDOT:PSS patterns is approximated to be ~20 nm and the side-wall angle to be less than 30°. Surface roughness and non-uniformity are also evident in the SEM images, both in the oblique angle and cross-sectional perspectives. The reduced height and side-wall angle of the PEDOT:PSS patterns indicate an incomplete vertical pattern transfer from the silicon master template by conventional thermal imprinting (dry conditions). Both longer imprinting times (up to 1 hour) and higher imprinting temperatures (180 °C) did not improve the fidelity of pattern transfer significantly, thus indicating that thermal annealing alone is insufficient to provide excellent nanoimprint fidelity.

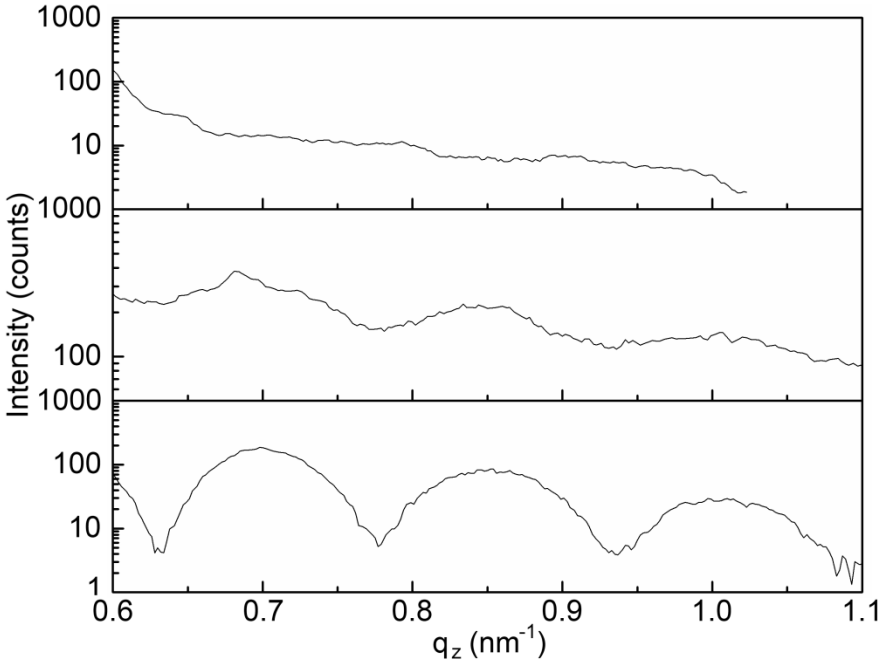


***Figure 7.6*** *Intensity along the third order Bragg rod extracted from the GISAXS images of thermally imprinted PEDOT:PSS pattern (top), water-vapor assisted imprinted PEDOT:PSS pattern (middle) and silicon master template (bottom).*

The quality of imprinted pattern can be significantly improved by introducing water-vapor during the imprinting process. A 39 nm feature height in the PEDOT:PSS pattern is obtained from the 0.160 nm$^{-1}$ modulation period along the BRs. This implies that the entire depth of the master template was imprinted into the PEDOT:PSS film in contrast to the dry thermal imprinting where the feature height was ~20 nm. The sidewall angle of (43±2)°, approximated from the shift in positions of the maxima along the BRs, is close to the sidewall angle of the master template. The GISAXS image of the PEDOT:PSS gratings patterned by water-vapor-assisted nanoimprinting (Figure 7.5 (c)) exhibits up to 20th order of BRs comparable to the number of BRs observed in the GISAXS patterns from the silicon master template. This suggests that the features remain reasonably sharp since rounded edges would diminish the intensity of the higher order peaks. The spacing of the BRs of the imprinted sample $\Delta q_r$ =0.0445 nm$^{-1}$ ,

corresponds to that of the master template. Our results indicate that the absorbed water in the PEDOT:PSS film provided by the humid environment ensures the complete filling of the master template cavities during the nanoimprinting process.

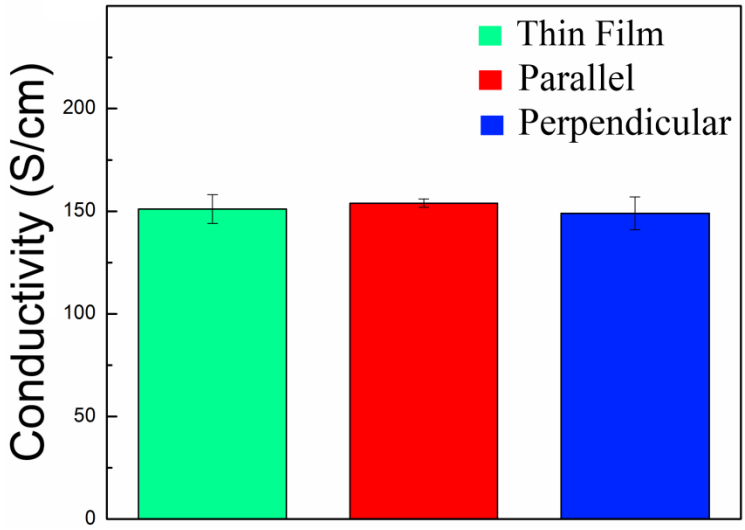


***Figure 7.7*** *Comparison of conductivities of PEDOT:PSS pattern fabricated by water-vapor-assisted imprinting along the grating direction (red), perpendicular to the grating (blue) and PEDOT:PSS thin film (green).*

In order to study the effect of water-vapor-assisted nanoimprinting on the conductivity of the PEDOT:PSS thin film, standard four-probe conductivity measurements were carried out in air using the Pro-4 system (Signatone). For the in-plane conductivity measurements, PEDOT:PSS thin films were spin-coated onto clean glass substrate and the thickness of the film was measured by a surface profilometer (Veeco Dektak 150). The measurements were repeated three time at slightly different location to obtain the average conductivity.

The conductivity of (151 ± 7) $Scm^{-1}$ was obtained for the control PEDOT:PSS thin film sample (Figure 7.7), consistent with literature values.[21] Both positive and negative effects of the thermal annealing on the conductivity of PEDOT:PSS thin film have been reported.[22, 23] While Nardes *et al* observed the conductivity of PEDOT:PSS thin film increases with annealing

temperature,[22] Dimitriev *et al* reported a substantial reduction in conductivity when heated to elevated temperature (~ 180 °C).[23] However, no significant changes in the conductivity of our PEDOT:PSS patterned films, fabricated by water-vapor-assisted imprinting, were observed. The conductivity along the grating direction is (154 ± 2) $Scm^{-1}$ while the conductivity of (149 ± 8) $Scm^{-1}$ is obtained along the direction perpendicular to the grating (Figure 7.7). The presence of a thick residual layer (~ 40 nm), beneath the imprinted depth, may contribute to the lack of in-plane anisotropy in the electrical properties of the PEDOT:PSS imprinted films. Moreover, GIWAXS measurements show that the polymer backbones in the PEDOT:PSS imprinted films does not exhibit any preferred in-plane orientation (Figure 7.8) along or perpendicular to the grating direction in contrast to the nanoimprinted semiconducting polymer, poly-(3 hexylthiophene), where its polymer backbones align preferentially along the grating direction.[18] This may in part explain the nearly isotropic conductivity observed in imprinted PEDOT:PSS films.

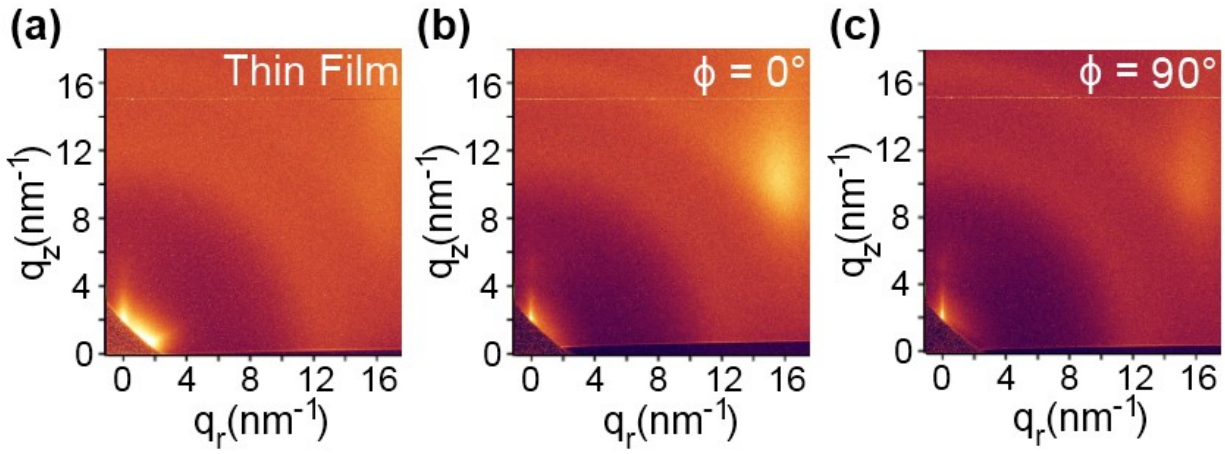


***Figure 7.8*** *2D GIWAXS patterns of (a) uniform PEDOT:PSS thin film and water-vapor assisted imprinted PEDOT:PSS pattern taken with azimuthal angle (b) $\phi = 0°$ and (c) $\phi = 90°$. The azimuthal angle ($\phi$) is defined as zero when the grating is parallel to the direction of incident x-rays. All GIWAXS patterns exhibit broad scattering ring centered around $q_r \sim 12\ nm^{-1}$ indicating that only short-range structural order exists and there is no preferential ordering of polymer backbones induced by nanoimprinting.*

The successful patterning on the PEDOT:PSS thin film with water-vapor-assisted nanoimprinting using a pattern with 70 nm features (140 nm pitch) were demonstrated. PEDOT:PSS is a composite material in which PEDOT domains are embedded in a PSS matrix. [20] The imprinting results suggest that the adsorbed water in the PSS matrix acts as a plasticizer while the PEDOT domains are softened by the elevated temperature. The excellent fidelity in the water-vapor-assisted nanoimprinting is confirmed by both GISAXS and SEM. Water-vapor assisted nanoimprinting does not affect the electrical properties of the PEDOT:PSS film and thus these nanopatterned PEDOT:PSS gratings may find useful applications in emerging organic electronics where the increased surface area may improve the electrical properties.

## 7.3 Device fabrication and characterization

The fabrication process for OPV device with nanoimprinted PEDOT:PSS films is schematically shown in Figure 7.9. The device structure was similar to the reference OPV devices described in Chapter 6 and consisted of ITO/PEDOT:PSS/P3HT:PCBM/Al. A thin film of PEDOT:PSS layer was first spin-coated (5000 rpm, 45s) onto ITO-coated glass substrates which was cleaned with $O_2$ plasma for 5 min and imprinted with the silicon master template following the same procedure described in section 7.2. A ~140 nm film of P3HT:PCBM was then spin-coated (1100 rpm, 45s) from a 1:1 2wt. % solution in dichlorobenzene to fill the nanostructured PEDOT:PSS layer. The conformal coating of the blend layer on the nanostructured PEDOT:PSS layer was obtained. Finally, a ~100 nm thick aluminum cathode was thermally evaporated through a shadow mask (1 mm diameter circles). Since imprinted area (~5 mm x 5mm) covered only part of the PEDOT:PSS coated ITO/Glass substrate (~15mm x 15

mm), multiple devices with both nanoimprinted and planar PEDOT:PSS layers were obtained for each sample. The samples were annealed at 140°C for 10 min in a vacuum oven before characterization.

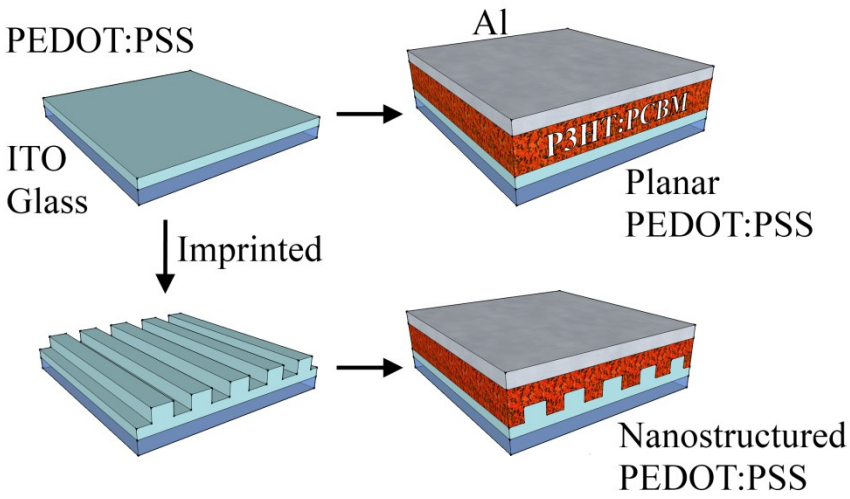


***Figure 7.9.*** *Fabrication process for BHJ solar cells with planar (top) and nanostructured (bottom) PEDOT:PSS layers.*

Figure 7.10 shows the representative J-V characteristic of the OPV devices fabricated with planar and nanostructured PEDOT:PSS layers. Here, the devices with planar PEDOT:PSS on the same sample were used as reference since they went through the same fabrication processes as patterned devices including the exposure to water-vapor. Note that the overall efficiency of the planar PEDOT:PSS devices (~1%) fabricated in this study was low compared with that of the planar PEDOT:PSS devices (~3%) presented in Chapter 6. One of the possible reason for observed difference in performance was the contamination on the surface of PEDOT:PSS layer during the water-vapor assisted imprinting process. For the device fabricated in Chapter 6, the deposition of the PEDOT:PSS layer was immediately followed by the

deposition of the blend layer. In this study, the spin-coated PEDOT:PSS layer was exposed to air for extended time during the transfer between the imprinting setup and device fabrication station as well as water-vapor and elevated temperature during the imprinting process. The hydrophobic layer coated on the silicon master template might partially desorbs when the mask is separated from the imprint and this would leave contaminating residues on the PEDOT:PSS surface.

Although the base efficiency of the reference planar PEDOT:PSS devices was low, it still served as a reference to study the effect of nanostrucuting of PEDOT:PSS layer. The variation between the patterned and reference device parameters was compared in Table 7.1. The values in the Table were obtained by averaging the extracted parameters from five different devices. The most significant improvement was observed in short circuit current ($J_{sc}$). Nanostructuring of PEDOT:PSS layer led to a ~35% increase in the short circuit current (Jsc), from 4.45 to 6.02 $mA/cm^2$ (see Table 7.1). Although variation in open circuit voltage was negligible, the fill factor (FF) increased from 39% to 42% and PCE of the device improved from 1.0% to 1.5%. However, the increase in PEDOT:PSS area by nanoimprinting was only ~ 26% which was less than the increase in $J_{sc}$ (~35%) and PCE (~50%). This difference implies an additional effect was present other than a simple increase in electrode area. In order to understand these improvement, structural characterization of the P3HT:PCBM layer deposited on both planar and nanostructured PEDOT:PSS layer were carried out.

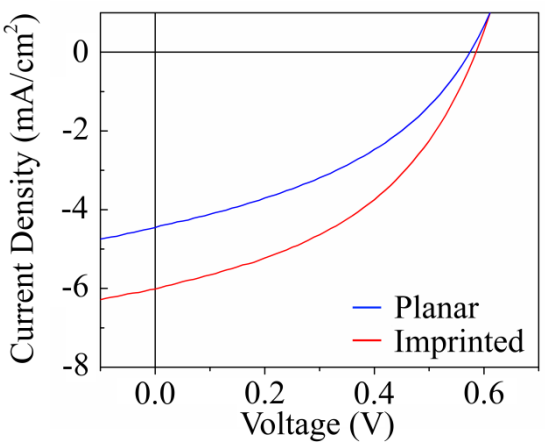


***Figure 7.10.*** *Representative J-V characteristics of BHJ solar cells fabricated with planar (blue) and imprinted (red) PEDOT:PSS layers*

TABLE 7.1. Characteristics of BHJ solar cells fabricated with planar and nanostructured PEDOT:PSS layers.

| Device | $J_{sc}$ (mA/cm$^2$) | $V_{oc}$ (V) | FF (%) | PCE (%) |
|---|---|---|---|---|
| **Planar** | 4.45 | 0.58 | 39 | 1.00 |
| **Nanostructured** | 6.02 | 0.59 | 42 | 1.50 |

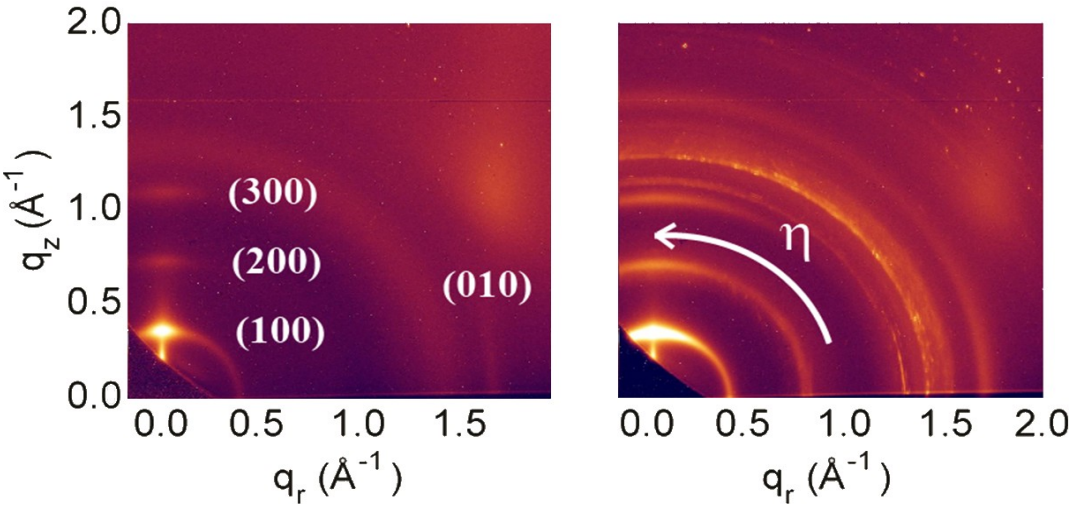


***Figure 7.11.*** *GIWAXS patterns of the P3HT:PCBM blends deposited on the planar(left) and nanostructured(right) PEDOT:PSS layers.*

GIWAXS measurements of the P3HT:PCBM blends indicated that the angular distribution of P3HT lamellae became broader when deposited on the nanostructured PEDOT:PSS layer. GIWAXS pattern from blend layer deposited on the planar PEDOT:PSS layer exhibited typical scattering peaks resulting from the lamellar stacking [(100),(200) and (300)] and π-π stacking (010) of the P3HT domains. Although the GIWAXS pattern from the blend layer deposited on the nanostructured PEDOT:PSS exhibited scattering peaks at similar *q* position, their angular distribution of the scattering intensity became broader, resulting in a series of rings (see Figure 7.11). This indicated that the edge-on oriented P3HT lamellar layers on the planar PEDOT:PSS layer were disturbed by nanostructuring of the underlying PEDOT:PSS layers. The lack of P3HT lamellar orientation along the out-of-plane direction would help improve the charge transport in that direction and therefore enhance the short circuit current. This structural difference may contribute to the observed improvement in performance of the naonimprinted PEDOT:PSS devices.

## 7.4 Conclusion

In summary, water-vapor-assisted nanoimprinting was employed to nanostructure PEDOT:PSS layer successfully. P3HT:PCBM OPV devices fabricated with the PEDOT:PSS nanogratings as the electron blocking layers showed ~35% improvement in short circuit current and ~50% improvement in power conversion efficiency. GIWAXS measurements showed that structural changes of the blend layer induced by nanostructured PEDOT:PSS layer may contribute to enhancement in device performance in addition to the increase in electrode area.

## 7.5 References


1. Rider, D. A.; Tucker, R. T.; Worfolk, B. J.; Krause, K. M.; Lalany, A.; Brett, M. J.; Buriak, J. M.; Harris, K. D., Indium tin oxide nanopillar electrodes in polymer/fullerene solar cells. *Nanotechnology* **2011,** 22, (8).
2. Yu, P. C.; Chang, C. H.; Su, M. S.; Hsu, M. H.; Wei, K. H., Embedded indium-tin-oxide nanoelectrodes for efficiency and lifetime enhancement of polymer-based solar cells. *Appl Phys Lett* **2010,** 96, (15).
3. Treat, N. D.; Campos, L. M.; Dimitriou, M. D.; Ma, B.; Chabinyc, M. L.; Hawker, C. J., Nanostructured hybrid solar cells: dependence of the open circuit voltage on the interfacial composition. *Adv Mater* **2010,** 22, (44), 4982-6.
4. Allen, J. E.; Black, C. T., Improved Power Conversion Efficiency in Bulk Heterojunction Organic Solar Cells with Radial Electron Contacts. *ACS Nano* **2011**.
5. Gunes, S.; Neugebauer, H.; Sariciftci, N. S., Conjugated polymer-based organic solar cells. *Chem Rev* **2007,** 107, (4), 1324-1338.
6. Fan, Z. Y.; Ruebusch, D. J.; Rathore, A. A.; Kapadia, R.; Ergen, O.; Leu, P. W.; Javey, A., Challenges and Prospects of Nanopillar-Based Solar Cells. *Nano Res* **2009,** 2, (11), 829-843.
7. Dimitrakopoulos, C. D.; Mascaro, D. J., Organic thin-film transistors: A review of recent advances. *Ibm J Res Dev* **2001,** 45, (1), 11-27.
8. Chu, T. Y.; Alem, S.; Verly, P. G.; Wakim, S.; Lu, J. P.; Tao, Y.; Beaupre, S.; Leclerc, M.; Belanger, F.; Desilets, D.; Rodman, S.; Waller, D.; Gaudiana, R., Highly efficient polycarbazole-based organic photovoltaic devices. *Appl Phys Lett* **2009,** 95, (6).

9. Iskandar, F.; Suryamas, A. B.; Kawabe, M.; Munir, M. M.; Okuyama, K.; Tarao, T.; Nishitani, T., Indium Tin Oxide Nanofiber Film Electrode for High Performance Dye Sensitized Solar Cells. *Jpn J Appl Phys* **2010,** 49, (1).

10. Wang, H. W.; Ting, C. F.; Hung, M. K.; Chiou, C. H.; Liu, Y. L.; Liu, Z. W.; Ratinac, K. R.; Ringer, S. P., Three-dimensional electrodes for dye-sensitized solar cells: synthesis of indium-tin-oxide nanowire arrays and ITO/TiO(2) core-shell nanowire arrays by electrophoretic deposition. *Nanotechnology* **2009,** 20, (5).

11. Takanezawa, K.; Hirota, K.; Wei, Q. S.; Tajima, K.; Hashimoto, K., Efficient charge collection with ZnO nanorod array in hybrid photovoltaic devices. *J Phys Chem C* **2007,** 111, (19), 7218-7223.

12. Takanezawa, K.; Tajima, K.; Hashimoto, K., Efficiency enhancement of polymer photovoltaic devices hybridized with ZnO nanorod arrays by the introduction of a vanadium oxide buffer layer. *Appl Phys Lett* **2008,** 93, (063308).

13. Kirchmeyer, S.; Reuter, K., Scientific importance, properties and growing applications of poly( 3,4-ethylenedioxythiophene). *J Mater Chem* **2005,** 15, (21), 2077-2088.

14. Jonas, F.; Schrader, L., Conductive Modifications of Polymers with Polypyrroles and Polythiophenes. *Synthetic Met* **1991,** 41, (3), 831-836.

15. Groenendaal, B. L.; Jonas, F.; Freitag, D.; Pielartzik, H.; Reynolds, J. R., Poly(3,4-ethylenedioxythiophene) and its derivatives: Past, present, and future. *Advanced Materials* **2000,** 12, (7), 481-494.

16. Taylor, P. C.; Lee, J. K.; Zakhidov, A. A.; Chatzichristidi, M.; Fong, H. H.; DeFranco, J. A.; Malliaras, G. C.; Ober, C. K., Orthogonal Patterning of PEDOT:PSS for Organic Electronics using Hydrofluoroether Solvents. *Advanced Materials* **2009,** 21, (22), 2314.

17. Lee, J. K.; Chatzichristidi, M.; Zakhidov, A. A.; Hwang, H. S.; Schwartz, E. L.; Sha, J.; Taylor, P. G.; Fong, H. H.; DeFranco, J. A.; Murotani, E.; Wong, W. W. H.; Malliaras, G. G.; Ober, C. K., Acid-diffusion behaviour in organic thin films and its effect on patterning. *J Mater Chem* **2009,** 19, (19), 2986-2992.

18. Reano, R. M.; Kong, Y. P.; Low, H. Y.; Tan, L.; Wang, F.; Pang, S. W.; Yee, A. F., Stability of functional polymers after plasticizer-assisted imprint lithography. *J Vac Sci Technol B* **2004,** 22, (6), 3294-3299.

19. Emah, J. B.; Curry, R. J.; Silva, S. R. P., Low cost patterning of poly (3,4-ethylenedioxythiophene) poly(styrenesulfonate) films to increase organic photovoltaic device efficiency. *Appl Phys Lett* **2008,** 93, (10).

20. Khang, D. Y.; Lee, H. H., Room-temperature imprint lithography by solvent vapor treatment. *Appl Phys Lett* **2000,** 76, (7), 870-872.

21. Kim, E.; Xia, Y. N.; Zhao, X. M.; Whitesides, G. M., Solvent-assisted microcontact molding: A convenient method for fabricating three-dimensional structures on surfaces of polymers. *Advanced Materials* **1997,** 9, (8), 651-654.

22. Elschner, A., *PEDOT : principles and applications of an intrinsically conductive polymer*. CRC Press: Boca Raton, FL, 2011; p xxi, 355 p.

23. Jung, Y. S.; Jung, W.; Tuller, H. L.; Ross, C. A., Nanowire Conductive Polymer Gas Sensor Patterned Using Self-Assembled Block Copolymer Lithography. *Nano Lett* **2008,** 8, (11), 3776-3780.

24. Voicu, N. E.; Ludwigs, S.; Crossland, E. J. W.; Andrew, P.; Steiner, U., Solvent-vapor-assisted imprint lithography. *Advanced Materials* **2007,** 19, (5), 757-+.

# CHAPTER 8

## Summary and Outlook

### 8.1 Summary

A deeper understanding of a processing/structure/property relationship in nanimprinted OPV devices is essential for the progress of the field and also for the application in other devices. This thesis reports the results of experimental studies of nanostructured semiconducting and conducting polymers that are utilized in organic photovoltaic devices.

In Chapter 4, results from structural characterization of Poly (3-alkylthiophene)s thin films were presented. The analysis of the X-ray scattering data reveals that P3AT polymers arrange in lamellar structure and pack without intedigitating side chains. Additionally, the P3AT crystalline domains mostly oriented edge-on with respect to the substrate. Furthermore, studies from *in situ* thermal and solvent annealing show that the P3HT lamellar layers expand significantly with increasing temperature and coherent length provided by dry annealing at 180˚C was obtained using pressurized toluene annealing at 135˚C.

In Chapter 5, results from in-depth structural characterization of the nanoimprinted P3HT thin film utilizing the combination of GISAXS/GIWAXS techniques were presented. The results of these studies show that nanoimprinting is a promising technique by which the active layer morphology can be greatly controlled and molecular orientation can be optimized. The imprinting process not only transfers the topographical features from the imprint master to the P3HT film with high fidelity but also reorients some of the polymers from edge-on to face-on orientation and aligns the P3HT backbones along the grating direction. Moreover, temperature-

dependent scattering measurements indicate that the imprinted induced orientation and alignment remains intact even at temperatures where the imprinted topographical features nearly vanish. Since charge transport characteristic of organic semiconductors is typically anisotropic and strongly dependent on crystalline ordering and molecular orientation, controlling these parameters is an important aspect of improving their performance in OPV applications.

In Chapter 6, the results from optimization of bulk heterojunction organic photovoltaic devices with planar PEDOT:PSS layer were presented. The performance of the polymers from three different suppliers were compared. Moreover, the thickness of the active layer was optimized to obtain the power conversion efficiency comparable to the literature values.

In Chapter 7, nanostructured PEDOT:PSS layer is explored as an alternative approach to improve the power conversion efficiency of organic photovoltaic devices. PEDOT:PSS thin films were successfully patterned with water-vapor-assisted nanoimprinting using a grating pattern with 70 nm features (140 nm pitch). The fidelity of the pattern-transfer was studied by GISAXS and SEM. The nanostructured PEDOT:PSS layer was then incorporated into OPV device providing substantial improvement in power conversion efficiency over the control device with planar PEDOT:PSS layer. GIWAXS measurements show that the underlying nanostructured PEDOT:PSS layer not only provide additional surface area for charge extraction but also affect the orientation of the subsequently deposited P3HT:PCBM blend layer. The optimization of the nanoimprinted patterns such as varying high and periodicity of the gratings, and characterization of the subsequently deposited bulk heterojunction layer will be essential in order to fully exploit the novel properties of these nanoimprinted structures in organic photovoltaic applications.

## 8.2 Outlook

Nanoimprinting is a promising techniques to fabricate the ordered hetero junction devices with the interdigitated D/A interface. Although the P3HT nanogratings were successfully imprinted in this work, the deposition of acceptor materials (PCBM) from the solution by spin-coating requires solvents that does not damage the imprinted P3HT structures. A search for orthogonal solvents that could dissolve the PCBM but do not deteriorate the P3HT layer was challenging since they were originally designed and synthesized to show similar solving behavior. In future work, damage to the imprinted P3HT structures could be avoided by employing UV/thermal cross-linkable derivatives of donor polymers as well as water-soluble acceptor molecules. Another possible way to address this would be to use double imprinting in which the imprinted nano-pattern on thin film of small molecules, such as PCBM, is used as a stamp to imprint a thin film of polymer such as P3HT. The double imprinting process will provide the ability to fabricate OHJ devices with relatively simple steps.

The nanostructured PEDOT:PSS layer could be extended beyond the P3HT:PCBM bulk heterojunction system which is investigated in this thesis. The low band gap polycarbozole derivative polymer such as PCDTBT have shown high PCE and the nanostructured PEDOT:PSS layer could further improve the performance. Moreover, PCDTBT exhibits face-on orientation in thin film morphology and the effect of nanostrucutred PEDOT:PSS layer on the orientation of the polymer can be compared and contrasted with present study on P3HT. The strategy to nanostructure PEDOT:PSS layer is also greatly applicable to other electron and hole blocking layers such as solution processed thin films of ZnO and $TiO_x$. Furthermore, nanostructuring both cathode and anode interfaces could result in reduced optical reflectance and therefore enhance absorption in the active layer. In the future, optimization and characterization of these

nanoimprinted semiconducting/conducting polymer nanostructures will be essential in order to fully exploit the novel properties of these structures for OPV applications.

# Bibliography

## Chapter 2


1. Light Absorption of Conjugated Materials. http://photonicswiki.org/images/d/d3/Polyene_series.PNG
2. http://wps.prenhall.com/wps/media/objects/3311/3391094/blb0906.html.
3. Goetzberger, A.; Hebling, C.; Schock, H. W., Photovoltaic materials, history, status and outlook. *Mat Sci Eng R* **2003,** 40, (1), 1-46.
4. Sariciftci, N. S.; Brabec, C. J.; Hummelen, J. C., Plastic solar cells. *Adv Funct Mater* **2001,** 11, (1), 15-26.
5. Service, R. F., Outlook Brightens for Plastic Solar Cells. *Science* **2011,** 332, (6027), 293-293.
6. Brabec, C. J.; Dyakonov, V.; Scherf, U., *Organic photovoltaics : materials, device physics, and manufacturing technologies*. Wiley-VCH: Weinheim, 2008; p xxi, 575 p.
7. Nelson, J., *The physics of solar cells*. Imperial College Press: London River Edge, NJ, 2003; p xix, 363 p.
8. Green, M. A.; Emery, K.; Hishikawa, Y.; Warta, W., Solar cell efficiency tables (version 36). *Prog Photovoltaics* **2010,** 18, (5), 346-352.
9. Heeger, A. J., Semiconducting polymers: the Third Generation. *Chem Soc Rev* **2010,** 39, (7), 2354-2371.
10. Marks, R. N.; Halls, J. J. M.; Bradley, D. D. C.; Friend, R. H.; Holmes, A. B., The Photovoltaic Response in Poly(P-Phenylene Vinylene) Thin-Film Devices. *J Phys-Condens Mat* **1994,** 6, (7), 1379-1394.

11. Sariciftci, N. S., Plastic solar cells. *Abstr Pap Am Chem S* **2001,** 222, U281-U281.

12. Electrical properties of silicon.

13. Tang, C. W., 2-Layer Organic Photovoltaic Cell. *Appl Phys Lett* **1986,** 48, (2), 183-185.

14. Forrest, S. R.; Peumans, P.; Yakimov, A., Small molecular weight organic thin-film photodetectors and solar cells. *J Appl Phys* **2003,** 93, (7), 3693-3723.

15. Yu, G.; Heeger, A. J., Charge Separation and Photovoltaic Conversion in Polymer Composites with Internal Donor-Acceptor Heterojunctions. *J Appl Phys* **1995,** 78, (7), 4510-4515.

16. Halls, J. J. M.; Walsh, C. A.; Greenham, N. C.; Marseglia, E. A.; Friend, R. H.; Moratti, S. C.; Holmes, A. B., Efficient Photodiodes from Interpenetrating Polymer Networks. *Nature* **1995,** 376, (6540), 498-500.

17. Li, G.; Shrotriya, V.; Huang, J. S.; Yao, Y.; Moriarty, T.; Emery, K.; Yang, Y., High-efficiency solution processable polymer photovoltaic cells by self-organization of polymer blends. *Nat Mater* **2005,** 4, (11), 864-868.

18. Brady, M. A.; Su, G. M.; Chabinyc, M. L., Recent progress in the morphology of bulk heterojunction photovoltaics. *Soft Matter* **2011,** 7, (23), 11065-11077.

19. Nunzi, J. M., Organic photovoltaic materials and devices. *Cr Phys* **2002,** 3, (4), 523-542.

20. Hoppe, H.; Sariciftci, N. S., Organic solar cells: An overview. *J Mater Res* **2004,** 19, (7), 1924- 1945.

21. Zhou, H. X.; Yang, L. Q.; You, W., Rational Design of High Performance Conjugated Polymers for Organic Solar Cells. *Macromolecules* **2012,** 45, (2), 607-632.

22. Stubinger, T.; Brutting, W., Exciton diffusion and optical interference in organic donor-acceptor photovoltaic cells. *J Appl Phys* **2001,** 90, (7), 3632-3641.

23. Gommans, H.; Schols, S.; Kadashchuk, A.; Heremans, P.; Meskers, S. C. J., Exciton Diffusion Length and Lifetime in Subphthalocyanine Films. *J Phys Chem C* **2009,** 113, (7), 2974-2979.

24. Luhman, W. A.; Holmes, R. J., Investigation of Energy Transfer in Organic Photovoltaic Cells and Impact on Exciton Diffusion Length Measurements. *Adv Funct Mater* **2011,** 21, (4), 764-771.

25. Blom, P. W. M.; Mihailetchi, V. D.; Koster, L. J. A.; Markov, D. E., Device physics of polymer : fullerene bulk heterojunction solar cells. *Advanced Materials* **2007,** 19, (12), 1551-1566.

26. Scharber, M. C.; Wuhlbacher, D.; Koppe, M.; Denk, P.; Waldauf, C.; Heeger, A. J.; Brabec, C. L., Design rules for donors in bulk-heterojunction solar cells - Towards 10 % energy-conversion efficiency. *Advanced Materials* **2006,** 18, (6), 789-+.

27. Dimitrakopoulos, C. D.; Mascaro, D. J., Organic thin-film transistors: A review of recent advances. *Ibm J Res Dev* **2001,** 45, (1), 11-27.

28. Li, G.; Shrotriya, V.; Yao, Y.; Huang, J. S.; Yang, Y., Manipulating regioregular poly(3-hexylthiophene): [6,6]-phenyl-C-61-butyric acid methyl ester blends - route towards high efficiency polymer solar cells. *J Mater Chem* **2007,** 17, (30), 3126-3140.

**Chapter 3**

1. Speakman, J. C., The Discovery of X-Ray-Diffraction by Crystals. *J Chem Educ* **1980,** 57, (7), 489-490.

2. Heeger, A. J., Semiconducting polymers: the Third Generation. *Chem Soc Rev* **2010,** 39, (7), 2354-2371.

3. Ezquerra, T. A., *Applications of synchrotron light to scattering and diffraction in materials and life sciences*. Springer: Berlin, 2009; p xvi, 318 p.

4. Grider, D. E.; Wright, A.; Ausburn, P. K., Electron-Beam Melting in Microfocus X-Ray Tubes. *J Phys D Appl Phys* **1986,** 19, (12), 2281-2292.

5. Shaheen, S. E.; Brabec, C. J.; Sariciftci, N. S.; Padinger, F.; Fromherz, T.; Hummelen, J. C., 2.5% efficient organic plastic solar cells. *Appl Phys Lett* **2001,** 78, (6), 841-843.

6. Als-Nielsen, J.; McMorrow, D., *Elements of modern X-ray physics*. Wiley: New York, 2001; p xi, 318 p.

7. Tolan, M., *X-ray scattering from soft-matter thin films : materials science and basic research*. Springer: Berlin ; New York, 1999; p viii, 197 p.

8. Busch, P.; Rauscher, M.; Smilgies, D. M.; Posselt, D.; Papadakis, C. M., Grazing-incidence small-angle X-ray scattering from thin polymer films with lamellar structures-the scattering cross section in the distorted-wave Born approximation. *J Appl Crystallogr* **2006,** 39, 433-442.

9. Brabec, C. J.; Cravino, A.; Meissner, D.; Sariciftci, N. S.; Fromherz, T.; Rispens, M. T.; Sanchez, L.; Hummelen, J. C., Origin of the open circuit voltage of plastic solar cells. *Adv Funct Mater* **2001,** 11, (5), 374-380.

10. Goetzberger, A.; Hebling, C.; Schock, H. W., Photovoltaic materials, history, status and outlook. *Mat Sci Eng R* **2003,** 40, (1), 1-46.

11. Warren, B. E., *X-ray diffraction*. Dover ed.; Dover Publications: New York, 1990; p vii, 381 p.

12. Smilgies, D. M., Scherrer grain-size analysis adapted to grazing-incidence scattering with area detectors. *J Appl Crystallogr* **2009,** 42, 1030-1034.

13. Wang, C. Q.; Jones, R. L.; Lin, E. K.; Wu, W. L.; Leu, J., Small angle x-ray scattering measurements of lithographic patterns with sidewall roughness from vertical standing waves. *Appl Phys Lett* **2007,** 90, (19).

14. Wang, C. Q.; Fu, W. E.; Li, B.; Huang, H.; Soles, C.; Lin, E. K.; Wu, W. L.; Ho, P. S.; Cresswell, M. W., Small angle X-ray scattering measurements of spatial dependent linewidth in dense nanoline gratings. *Thin Solid Films* **2009,** 517, (20), 5844-5847.

15. Wang, C. Q.; Jones, R. L.; Lin, E. K.; Wu, W. L.; Ho, D. L.; Villarrubia, J. S.; Choi, K. W.; Clarke, J. S.; Roberts, J.; Bristol, R.; Bunday, B., Line edge roughness and cross sectional characterization of sub-50 nm structures using critical dimension small angle x-ray scattering. *Aip Conf Proc* **2007,** 931, 402-406.

16. Wang, C. Q.; Jones, R. L.; Lin, E. K.; Wu, W. L.; Rice, B. J.; Choi, K. W.; Thompson, G.; Weigand, S. J.; Keane, D. T., Characterization of correlated line edge roughness of nanoscale line gratings using small angle x-ray scattering. *J Appl Phys* **2007,** 102, (2).

17. Meyer, A. Form Factor. http://www.gisaxs.de/theory2.html (April 4, 2012)

**Chapter 4**

1. Gunes, S.; Neugebauer, H.; Sariciftci, N. S., Conjugated polymer-based organic solar cells. *Chem Rev* **2007,** 107, (4), 1324-1338.

2. Sirringhaus, H., Device physics of Solution-processed organic field-effect transistors. *Adv Mater* **2005,** 17, (20), 2411-2425.

3. Sirringhaus, H.; Tessler, N.; Friend, R. H., Integrated optoelectronic devices based on conjugated polymers. *Science* **1998,** 280, (5370), 1741-1744.

4. Li, G.; Shrotriya, V.; Yao, Y.; Huang, J. S.; Yang, Y., Manipulating regioregular poly(3-hexylthiophene): [6,6]-phenyl-C-61-butyric acid methyl ester blends - route towards high efficiency polymer solar cells. *J Mater Chem* **2007,** 17, (30), 3126-3140.

5. Joshi, S.; Grigorian, S.; Pietsch, U., X-ray structural and crystallinity studies of low and high molecular weight poly(3-hexylthiophene). *phys. stat. sol. (a)*, 2008; Vol. 205, pp 488-496.

6. Woo, C.; Thompson, B.; Kim, B.; Toney, M.; Fréchet, J., The Influence of Poly(3-hexylthiophene) Regioregularity on Fullerene-Composite Solar Cell Performance. *J. Am. Chem. Soc.*, 2008; Vol. 130, pp 16324-16329.

7. Ma, W.; Yang, C.; Gong, X.; Lee, K.; Heeger, A. J., Thermally Stable, Efficient Polymer Solar Cells with Nanoscale Control of the Interpenetraging Network Morphology. *Adv. Funct. Matt.* **2005,** 15, 1617-1622.

8. Jaczewska, J.; Raptis, I.; Budkowski, A.; Goustouridis, D.; Raczkowska, J.; Sanopoulou, M.; Pamuł, E.; Bernasik, A.; Rysza, J., *Swelling of P3HT films exposed to solvent vapors an humidity: Evaluation of solubility parameters*, 2007; pp 1-6.

9. Kim, D.; Park, Y.; Jang, Y.; Kim, S.; Cho, K., Solvent Vapor-Induced Nanowire Formation in Poly(3-hexylthiophene) Thin Films. *Macromol. Rapid Commun.*, 2005; Vol. 26, pp 834-839.

10. http://webbook.nist.gov/cgi/cbook.cgi?ID=C108883&Mask=4

11. Osterbacka, R.; An, C. P.; Jiang, X. M.; Vardeny, Z. V., Two-dimensional electronic excitations in self-assembled conjugated polymer nanocrystals. *Science* **2000,** 287, (5454), 839-842.

12. Sirringhaus, H.; Brown, P. J.; Friend, R. H.; Nielsen, M. M.; Bechgaard, K.; Langeveld-Voss, B. M. W.; Spiering, A. J. H.; Janssen, R. A. J.; Meijer, E. W.; Herwig, P.; de Leeuw, D. M., Two-dimensional charge transport in self-organized, high-mobility conjugated polymers. *Nature* **1999,** 401, (6754), 685-688.

13. Stepanyan, R.; Subbotin, A.; Knaapila, M.; Ikkala, O.; ten Brinke, G., Self-organization of hairy-rod polymers. *Macromolecules* **2003,** 36, (10), 3758-3763.

14. Prosa, T. J.; Winokur, M. J.; McCullough, R. D., Evidence of a novel side chain structure in regioregular poly(3-alkylthiophenes). *Macromolecules* **1996,** 29, (10), 3654-3656.

15. Tashiro, K.; Kobayashi, M.; Kawai, T.; Yoshino, K., Crystal structural change in poly(3-alkyl thiophene)s induced by iodine doping as studied by an organized combination of X-ray diffraction, infrared/Raman spectroscopy and computer simulation techniques. *Polymer* **1997,** 38, (12), 2867-2879.

16. Xie, H. W.; Corish, J.; Morton-Blake, D. A., Thermochromic distortions in a poly(3-alkylthiophene): an atomistic simulation investigation. *Synthetic Met* **2000,** 113, (1-2), 65-72.

17. Yamamoto, T.; Komarudin, D.; Arai, M.; Lee, B. L.; Suganuma, H.; Asakawa, N.; Inoue, Y.; Kubota, K.; Sasaki, S.; Fukuda, T.; Matsuda, H., Extensive studies on pi-stacking of poly(3-alkylthiophene-2,5-diyl)s and poly(4-alkylthiazole-2,5-diyl)s by optical spectroscopy, NMR analysis, light scattering analysis, and X-ray crystallography. *J Am Chem Soc* **1998,** 120, (9), 2047-2058.

18. McCullough, R. D., The chemistry of conducting polythiophenes. *Adv Mater* **1998,** 10, (2), 93-98.

19. Kim, D. H.; Park, Y. D.; Jang, Y. S.; Yang, H. C.; Kim, Y. H.; Han, J. I.; Moon, D. G.; Park, S. J.; Chang, T. Y.; Chang, C. W.; Joo, M. K.; Ryu, C. Y.; Cho, K. W., Enhancement of field-effect mobility due to surface-mediated molecular ordering in regioregular polythiophene thin film transistors. *Adv Funct Mater* **2005,** 15, (1), 77-82.

20. Malik, S.; Nandi, A. K., Crystallization mechanism of regioregular poly(3-alkyl thiophene)s. *J Polym Sci Pol Phys* **2002,** 40, (18), 2073-2085.

21. Kline, R. J.; DeLongchamp, D. M.; Fischer, D. A.; Lin, E. K.; Richter, L. J.; Chabinyc, M. L.; Toney, M. F.; Heeney, M.; McCulloch, I., Critical role of side-chain attachment density on the order and device performance of polythiophenes. *Macromolecules* **2007,** 40, (22), 7960-7965.

22. Khasanshin, T. S.; Shchamialiou, A. P.; Poddubskij, O. G.; Thermodynamic Properties of Heavy n-Alkanes in the Liquid State: n-Dodecane, *Int. J of Thermophysics* **2003**, 24, (5), 1277-1289.

23. Ballauff, M., Stiff-Chain Polymers - Structure, Phase-Behavior, and Properties. *Angew Chem Int Edit* **1989,** 28, (3), 253-267.

24. Watanabe, J.; Harkness, B. R.; Sone, M.; Ichimura, H., Rigid-Rod Polyesters with Flexible Side-Chains .4. Thermotropic Behavior and Phase Structures in Polyesters Based on 1,4-Dialkyl Esters of Pyromellitic Acid and 4,4'-Biphenol. *Macromolecules* **1994,** 27, (2), 507-512.

25. Yang, C.; Orfino, F. P.; Holdcroft, S., A phenomenological model for predicting thermochromism of regioregular and nonregioregular poly(3-alkylthiophenes). *Macromolecules* **1996,** 29, (20), 6510-6517.

26. Gurau, M. C.; Delongchamp, D. M.; Vogel, B. M.; Lin, E. K.; Fischer, D. A.; Sambasivan, S.; Richter, L. J., Measuring molecular order in poly(3-alkylthiophene) thin films with polarizing spectroscopies. *Langmuir* **2007,** 23, (2), 834-842.

27. Ong, B. S.; Wu, Y. L.; Liu, P.; Gardner, S., High-performance semiconducting polythiophenes for organic thin-film transistors. *J Am Chem Soc* **2004,** 126, (11), 3378-3379.

28. I, M.; Heeney, M.; Bailey, C.; Genevicius, K.; I, M.; Shkunov, M.; Sparrowe, D.; Tierney, S.; Wagner, R.; Zhang, W. M.; Chabinyc, M. L.; Kline, R. J.; Mcgehee, M. D.; Toney, M. F., Liquid-crystalline semiconducting polymers with high charge-carrier mobility. *Nat Mater* **2006,** 5, (4), 328-333.

29. Barrera, G. D.; Bruno, J. A. O.; Barron, T. H. K.; Allan, N. L.; Negative thermal expansion. J. Phys. Cond. Matt. 17, R217 (2005).

30. Park, J. H.; Kim, J. S.; Lee, J. H.; Lee, W. H.; Cho, K., Effect of Annealing Solvent Solubility on the Performance of Poly(3-hexylthiophene)/Methanofullerene Solar Cells. *J Phys Chem C* **2009,** 113, (40), 17579-17584.

31. Li, G.; Yao, Y.; Yang, H.; Shrotriya, V.; Yang, G.; Yang, Y., "Solvent annealing" effect in polymer solar cells based on poly(3-hexylthiophene) and methanofullerenes. *Adv Funct Mater* **2007,** 17, (10), 1636-1644.

32. Kaganer, V. M.; Mohwald, H.; Dutta, P., Structure and phase transitions in Langmuir monolayers. *Rev Moder Phys* **1999,** 71, (3), 779-819.

33. Craievich, A. F.; Denicolo, I.; Doucet, J., Molecular motion and conformational defects in odd-numbered paraffins. Phys Rev B 1984, 30, (8), 4782-4787

## Chapter 5

1. Mele, E.; Di Benedetto, F.; Persano, L.; Cingolani, R.; Pisignano, D., Multilevel, room-temperature nanoimprint lithography for conjugated polymer-based photonics. *Nano Lett* **2005,** 5, (10), 1915-1919.

2. Li, H. W.; Huck, W. T. S., Ordered block-copolymer assembly using nanoimprint lithography. *Nano Letters* **2004,** 4, (9), 1633-1636.

3. Hu, Z. J.; Baralia, G.; Bayot, V.; Gohy, J. F.; Jonas, A. M., Nanoscale control of polymer crystallization by nanoimprint lithography. *Nano Lett* **2005,** 5, (9), 1738-1743.

4. He, X., Gao, F., Tu, G., Hasko, D. G., Hüttner, S., Greenham, N. C., Steiner, U., Friend, R. H. and Huck, W. T. S., Formation of Well-Ordered Heterojunctions in Polymer:PCBM Photovoltaic Devices. *Adv Funct Mater* **2011,** 21, (1), 139-146.

5. He, X. M.; Gao, F.; Tu, G. L.; Hasko, D.; Huttner, S.; Steiner, U.; Greenham, N. C.; Friend, R. H.; Huck, W. T. S., Formation of Nanopatterned Polymer Blends in Photovoltaic Devices. *Nano Lett* **2010,** 10, (4), 1302-1307.

6. Austin, M. D.; Ge, H. X.; Wu, W.; Li, M. T.; Yu, Z. N.; Wasserman, D.; Lyon, S. A.; Chou, S. Y., Fabrication of 5 nm linewidth and 14 nm pitch features by nanoimprint lithography. *Appl Phys Lett* **2004,** 84, (26), 5299-5301.

7. Jung, G. Y.; Johnston-Halperin, E.; Wu, W.; Yu, Z. N.; Wang, S. Y.; Tong, W. M.; Li, Z. Y.; Green, J. E.; Sheriff, B. A.; Boukai, A.; Bunimovich, Y.; Heath, J. R.; Williams, R. S., Circuit fabrication at 17 nm half-pitch by nanoimprint lithography. *Nano Lett* **2006,** 6, (3), 351-354.

8. Chou, S. Y.; Krauss, P. R.; Renstrom, P. J., Imprint lithography with 25-nanometer resolution. *Science* **1996,** 272, (5258), 85-87.

9. Zheng, Z. J.; Yim, K. H.; Saifullah, M. S. M.; Welland, M. E.; Friend, R. H.; Kim, J. S.; Huck, W. T. S., Uniaxial alignment of liquid-crystalline conjugated polymers by nanoconfinement. *Nano Lett* **2007,** 7, (4), 987-992.

10. Hu, Z. J.; Muls, B.; Gence, L.; Serban, D. A.; Hofkens, J.; Melinte, S.; Nysten, B.; Demoustier-Champagne, S.; Jonas, A. M., High-throughput fabrication of organic nanowire devices with preferential internal alignment and improved performance. *Nano Lett* **2007,** 7, (12), 3639-3644.

11. DeLongchamp, D. M.; Vogel, B. M.; Jung, Y.; Gurau, M. C.; Richter, C. A.; Kirillov, O. A.; Obrzut, J.; Fischer, D. A.; Sambasivan, S.; Richter, L. J.; Lin, E. K., Variations in semiconducting polymer microstructure and hole mobility with spin-coating speed. *Chem Mater* **2005,** 17, (23), 5610-5612.

12. Yang, H. H.; LeFevre, S. W.; Ryu, C. Y.; Bao, Z. N., Solubility-driven thin film structures of regioregular poly(3-hexyl thiophene) using volatile solvents. *Appl Phys Lett* **2007,** 90, (17), -.

13. Sirringhaus, H.; Wilson, R. J.; Friend, R. H.; Inbasekaran, M.; Wu, W.; Woo, E. P.; Grell, M.; Bradley, D. D. C., Mobility enhancement in conjugated polymer field-effect transistors through chain alignment in a liquid-crystalline phase. *Appl Phys Lett* **2000,** 77, (3), 406-408.

14. Kline, R. J.; Mcgehee, M. D.; Toney, M. F., Highly oriented crystals at the buried interface in polythiophene thin-film transistors. *Nat Mater* **2006,** 5, (3), 222-228.

15. Yang, H. C.; Shin, T. J.; Yang, L.; Cho, K.; Ryu, C. Y.; Bao, Z. N., Effect of mesoscale crystalline structure on the field-effect mobility of regioregular poly(3-hexyl thiophene) in thin-film transistors. *Adv Funct Mater* **2005,** 15, (4), 671-676.

16. Chang, J. F.; Sun, B. Q.; Breiby, D. W.; Nielsen, M. M.; Solling, T. I.; Giles, M.; McCulloch, I.; Sirringhaus, H., Enhanced mobility of poly(3-hexylthiophene) transistors by spin-coating from high-boiling-point solvents. *Chem Mater* **2004,** 16, (23), 4772-4776.

17. Sirringhaus, H.; Brown, P. J.; Friend, R. H.; Nielsen, M. M.; Bechgaard, K.; Langeveld-Voss, B. M. W.; Spiering, A. J. H.; Janssen, R. A. J.; Meijer, E. W.; Herwig, P.; de Leeuw, D. M., Two-dimensional charge transport in self-organized, high-mobility conjugated polymers. *Nature* **1999,** 401, (6754), 685-688.

18. Guo, L. J., Nanoimprint lithography: Methods and material requirements. *Adv Mater* **2007,** 19, (4), 495-513.

19. Peng, Q.; Tseng, Y. C.; Darling, S. B.; Elam, J. W., Nanoscopic Patterned Materials with Tunable Dimensions via Atomic Layer Deposition on Block Copolymers. *Adv Mater* **2010,** 22, (45), 5129-+.

20. Peng, Q.; Tseng, Y. C.; Darling, S. B.; Elam, J. W., A Route to Nanoscopic Materials via Sequential Infiltration Synthesis on Block Copolymer Templates. *Acs Nano* **2011,** 5, (6), 4600-4606.

21. Tseng, Y. C.; Peng, Q.; Ocola, L. E.; Elam, J. W.; Darling, S. B., Enhanced Block Copolymer Lithography Using Sequential Infiltration Synthesis. *J Phys Chem C* **2011,** 115, (36), 17725-17729.

22. Savas, T. A.; Schattenburg, M. L.; Carter, J. M.; Smith, H. I., Large-area achromatic interferometric lithography for 100 nm period gratings and grids. *J Vac Sci Technol B* **1996,** 14, (6), 4167-4170.

23. Hofmann, T.; Dobisz, E.; Ocko, B. M., Grazing incident small angle x-ray scattering: A metrology to probe nanopatterned surfaces. *J Vac Sci Technol B* **2009,** 27, (6), 3238-3243.

24. Born, M.; Wolf, E., *Principles of optics; electromagnetic theory of propagation, interference, and diffraction of light*. Pergamon Press: London, New York, 1959, p 803.

25. Hu, T. J.; Jones, R. L.; Wu, W. L.; Lin, E. K.; Lin, Q. H.; Keane, D.; Weigand, S.; Quintana, J., Small angle x-ray scattering metrology for sidewall angle and cross section of nanometer scale line gratings. *J Appl Phys* **2004,** 96, (4), 1983-1987.

26. Aryal, M.; Trivedi, K.; Hu, W. C., Nano-Confinement Induced Chain Alignment in Ordered P3HT Nanostructures Defined by Nanoimprint Lithography. *Acs Nano* **2009,** 3, (10), 3085-3090.

27. Jones, R. L.; Hu, T. J.; Soles, C. L.; Lin, E. K.; Reano, R. M.; Casa, D. M., Real-time shape evolution of nanoimprinted polymer structures during thermal annealing. *Nano Lett* **2006,** 6, (8), 1723-1728.

28. Lee, H. J.; Soles, C. L.; Ro, H. W.; Jones, R. L.; Lin, E. K.; Wu, W. L.; Hines, D. R., Nanoimprint pattern transfer quality from specular x-ray reflectivity. *Appl Phys Lett* **2005,** 87, (26), -.

29. Ding, Y. F.; Ro, H. W.; Germer, T. A.; Douglas, J. F.; Okerberg, B. C.; Karim, A.; Soles, C. L., Relaxation Behavior of polymer structures fabricated by nanoimprint lithography. *Acs Nano* **2007,** 1, (2), 84-92.

30. Patrick, H. J.; Germer, T. A.; Ding, Y. F.; Ro, H. W.; Richter, L. J.; Soles, C. L., Scatterometry for in situ measurement of pattern reflow in nanoimprinted polymers. *Appl Phys Lett* **2008,** 93, (23), -.

31. Smilgies, D. M., Scherrer grain-size analysis adapted to grazing-incidence scattering with area detectors. *J Appl Crystallogr* **2009,** 42, 1030-1034.

32. Ocko, B. M.; Wu, X. Z.; Sirota, E. B.; Sinha, S. K.; Gang, O.; Deutsch, M., Surface freezing in chain molecules: Normal alkanes. *Phys Rev E* **1997,** 55, (3), 3164-3182.

**Chapter 6**

1. van Duren, J. K. J.; Yang, X. N.; Loos, J.; Bulle-Lieuwma, C. W. T.; Sieval, A. B.; Hummelen, J. C.; Janssen, R. A. J., Relating the morphology of poly(p-phenylene vinylene)/methanofullerene blends to solar-cell performance. *Adv Funct Mater* **2004,** 14, (5), 425-434.

2. Moule, A. J.; Bonekamp, J. B.; Meerholz, K., The effect of active layer thickness and composition on the performance of bulk-heterojunction solar cells. *J Appl Phys* **2006,** 100, (9).

3. Shaheen, S. E.; Brabec, C. J.; Sariciftci, N. S.; Padinger, F.; Fromherz, T.; Hummelen, J. C., 2.5% efficient organic plastic solar cells. *Appl Phys Lett* **2001,** 78, (6), 841-843.

4. Rispens, M. T.; Meetsma, A.; Rittberger, R.; Brabec, C. J.; Sariciftci, N. S.; Hummelen, J. C., Influence of the solvent on the crystal structure of PCBM and the efficiency of MDMO-PPV : PCBM 'plastic' solar cells. *Chem Commun* **2003**, (17), 2116-2118.

5. Li, G.; Shrotriya, V.; Yao, Y.; Yang, Y., Investigation of annealing effects and film thickness dependence of polymer solar cells based on poly(3-hexylthiophene). *J Appl Phys* **2005,** 98, (4).

6. Lenes, M.; Koster, L. J. A.; Mihailetchi, V. D.; Blom, P. W. M., Thickness dependence of the efficiency of polymer : fullerene bulk heterojunction solar cells. *Appl Phys Lett* **2006,** 88, (24).

7. Ma, W. L.; Yang, C. Y.; Gong, X.; Lee, K.; Heeger, A. J., Thermally stable, efficient polymer solar cells with nanoscale control of the interpenetrating network morphology. *Adv Funct Mater* **2005,** 15, (10), 1617-1622.

8. Li, G.; Shrotriya, V.; Huang, J. S.; Yao, Y.; Moriarty, T.; Emery, K.; Yang, Y., High-efficiency solution processable polymer photovoltaic cells by self-organization of polymer blends. *Nat Mater* **2005,** 4, (11), 864-868.

9. Reyes-Reyes, M.; Kim, K.; Carroll, D. L., High-efficiency photovoltaic devices based on annealed poly(3-hexylthiophene) and 1-(3-methoxycarbonyl)-propyl-1-phenyl-(6,6)C-61 blends. *Appl Phys Lett* **2005,** 87, (8).

10. Hoppe, H.; Arnold, N.; Sariciftci, N. S.; Meissner, D., Modeling the optical absorption within conjugated polymer/fullerene-based bulk-heterojunction organic solar cells. *Sol Energ Mat Sol C* **2003,** 80, (1), 105-113.

11. Pettersson, L. A. A.; Roman, L. S.; Inganas, O., Modeling photocurrent action spectra of photovoltaic devices based on organic thin films. *J Appl Phys* **1999,** 86, (1), 487-496.

**Chapter 7**

1. Rider, D. A.; Tucker, R. T.; Worfolk, B. J.; Krause, K. M.; Lalany, A.; Brett, M. J.; Buriak, J. M.; Harris, K. D., Indium tin oxide nanopillar electrodes in polymer/fullerene solar cells. *Nanotechnology* **2011,** 22, (8).
2. Yu, P. C.; Chang, C. H.; Su, M. S.; Hsu, M. H.; Wei, K. H., Embedded indium-tin-oxide nanoelectrodes for efficiency and lifetime enhancement of polymer-based solar cells. *Appl Phys Lett* **2010,** 96, (15).
3. Treat, N. D.; Campos, L. M.; Dimitriou, M. D.; Ma, B.; Chabinyc, M. L.; Hawker, C. J., Nanostructured hybrid solar cells: dependence of the open circuit voltage on the interfacial composition. *Adv Mater* **2010,** 22, (44), 4982-6.
4. Allen, J. E.; Black, C. T., Improved Power Conversion Efficiency in Bulk Heterojunction Organic Solar Cells with Radial Electron Contacts. *ACS Nano* **2011**.
5. Gunes, S.; Neugebauer, H.; Sariciftci, N. S., Conjugated polymer-based organic solar cells. *Chem Rev* **2007,** 107, (4), 1324-1338.
6. Fan, Z. Y.; Ruebusch, D. J.; Rathore, A. A.; Kapadia, R.; Ergen, O.; Leu, P. W.; Javey, A., Challenges and Prospects of Nanopillar-Based Solar Cells. *Nano Res* **2009,** 2, (11), 829-843.
7. Dimitrakopoulos, C. D.; Mascaro, D. J., Organic thin-film transistors: A review of recent advances. *Ibm J Res Dev* **2001,** 45, (1), 11-27.

8. Chu, T. Y.; Alem, S.; Verly, P. G.; Wakim, S.; Lu, J. P.; Tao, Y.; Beaupre, S.; Leclerc, M.; Belanger, F.; Desilets, D.; Rodman, S.; Waller, D.; Gaudiana, R., Highly efficient polycarbazole-based organic photovoltaic devices. *Appl Phys Lett* **2009,** 95, (6).

9. Iskandar, F.; Suryamas, A. B.; Kawabe, M.; Munir, M. M.; Okuyama, K.; Tarao, T.; Nishitani, T., Indium Tin Oxide Nanofiber Film Electrode for High Performance Dye Sensitized Solar Cells. *Jpn J Appl Phys* **2010,** 49, (1).

10. Wang, H. W.; Ting, C. F.; Hung, M. K.; Chiou, C. H.; Liu, Y. L.; Liu, Z. W.; Ratinac, K. R.; Ringer, S. P., Three-dimensional electrodes for dye-sensitized solar cells: synthesis of indium-tin-oxide nanowire arrays and ITO/TiO(2) core-shell nanowire arrays by electrophoretic deposition. *Nanotechnology* **2009,** 20, (5).

11. Takanezawa, K.; Hirota, K.; Wei, Q. S.; Tajima, K.; Hashimoto, K., Efficient charge collection with ZnO nanorod array in hybrid photovoltaic devices. *J Phys Chem C* **2007,** 111, (19), 7218-7223.

12. Takanezawa, K.; Tajima, K.; Hashimoto, K., Efficiency enhancement of polymer photovoltaic devices hybridized with ZnO nanorod arrays by the introduction of a vanadium oxide buffer layer. *Appl Phys Lett* **2008,** 93, (063308).

13. Kirchmeyer, S.; Reuter, K., Scientific importance, properties and growing applications of poly( 3,4-ethylenedioxythiophene). *J Mater Chem* **2005,** 15, (21), 2077-2088.

14. Jonas, F.; Schrader, L., Conductive Modifications of Polymers with Polypyrroles and Polythiophenes. *Synthetic Met* **1991,** 41, (3), 831-836.

15. Groenendaal, B. L.; Jonas, F.; Freitag, D.; Pielartzik, H.; Reynolds, J. R., Poly(3,4-ethylenedioxythiophene) and its derivatives: Past, present, and future. *Advanced Materials* **2000,** 12, (7), 481-494.

16. Taylor, P. C.; Lee, J. K.; Zakhidov, A. A.; Chatzichristidi, M.; Fong, H. H.; DeFranco, J. A.; Malliaras, G. C.; Ober, C. K., Orthogonal Patterning of PEDOT:PSS for Organic Electronics using Hydrofluoroether Solvents. *Advanced Materials* **2009,** 21, (22), 2314.

17. Lee, J. K.; Chatzichristidi, M.; Zakhidov, A. A.; Hwang, H. S.; Schwartz, E. L.; Sha, J.; Taylor, P. G.; Fong, H. H.; DeFranco, J. A.; Murotani, E.; Wong, W. W. H.; Malliaras, G. G.; Ober, C. K., Acid-diffusion behaviour in organic thin films and its effect on patterning. *J Mater Chem* **2009,** 19, (19), 2986-2992.

18. Reano, R. M.; Kong, Y. P.; Low, H. Y.; Tan, L.; Wang, F.; Pang, S. W.; Yee, A. F., Stability of functional polymers after plasticizer-assisted imprint lithography. *J Vac Sci Technol B* **2004,** 22, (6), 3294-3299.

19. Emah, J. B.; Curry, R. J.; Silva, S. R. P., Low cost patterning of poly (3,4-ethylenedioxythiophene) poly(styrenesulfonate) films to increase organic photovoltaic device efficiency. *Appl Phys Lett* **2008,** 93, (10).

20. Khang, D. Y.; Lee, H. H., Room-temperature imprint lithography by solvent vapor treatment. *Appl Phys Lett* **2000,** 76, (7), 870-872.

21. Kim, E.; Xia, Y. N.; Zhao, X. M.; Whitesides, G. M., Solvent-assisted microcontact molding: A convenient method for fabricating three-dimensional structures on surfaces of polymers. *Advanced Materials* **1997,** 9, (8), 651-654.

22. Elschner, A., *PEDOT : principles and applications of an intrinsically conductive polymer*. CRC Press: Boca Raton, FL, 2011; p xxi, 355 p.

23. Jung, Y. S.; Jung, W.; Tuller, H. L.; Ross, C. A., Nanowire Conductive Polymer Gas Sensor Patterned Using Self-Assembled Block Copolymer Lithography. *Nano Lett* **2008,** 8, (11), 3776-3780.

24. Voicu, N. E.; Ludwigs, S.; Crossland, E. J. W.; Andrew, P.; Steiner, U., Solvent-vapor-assisted imprint lithography. *Advanced Materials* **2007,** 19, (5), 757-761.